The role of Ca^{2+} influx mechanisms in the regulation of human cardiac fibroblasts in 2D- and 3D- culture models

Dissertation

for the award of the degree

“Doctor of Philosophy” (Ph.D.)

of the Georg-August-Universität Göttingen

within the doctoral program “Molecular Medicine”

of the Georg-August University School of Science (GAUSS)

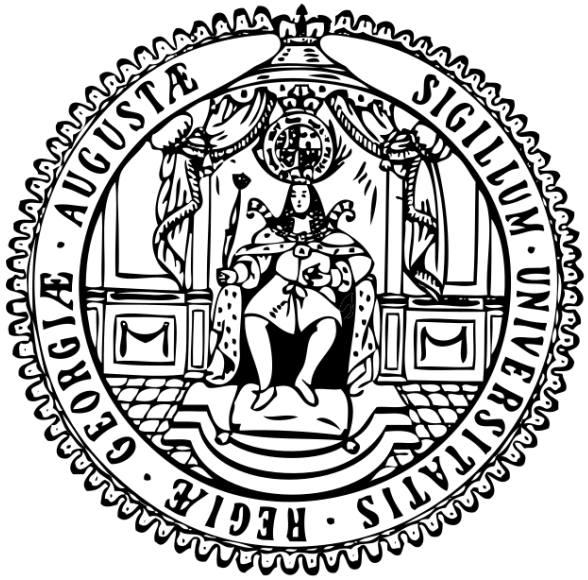

Submitted by

Abdul Rehman

Gujranwala, Pakistan

Göttingen, November 2020

Thesis Committee and Examination Board

Doctoral Thesis Committee

Supervisor

Prof. Dr. Susanne Lutz
Institute of Pharmacology and Toxicology
University Medical Center, Göttingen

Co-supervisor-1

Prof. Dr. Thomas Meyer
Department of Psychosomatic Medicine and Psychotherapy
University Medical Center, Göttingen

Co-supervisor-2

Prof. Dr. Jürgen Brockmöller
Institute of Clinical Pharmacology
University Medical Center, Göttingen

Extended Examination Board Members

Prof. Dr. Frauke Alves
Clinic of Hematology and Medical Oncology
University Medical Center, Göttingen

Prof. Dr. Ralf Dressel
Institute of Cellular and Molecular Immunology
University Medical Center, Göttingen

Dr. Antje Ebert
Department of Cardiology and Pneumology
University Medical Center, Göttingen

Date of submission of thesis: 05.11.2020

Date of the oral examination: 18.12.2020

Declaration

I hereby declare that the thesis entitled "**The role of Ca^{2+} influx mechanisms in the regulation of human cardiac fibroblasts in 2D- and 3D- culture models**" has been solely written by myself and with no other sources and aids than quoted.

Abdul Rehman **Göttingen: 05.11.2020**

Acknowledgements

During the last some years, being a Ph.D. student at the University Medical Centre, Göttingen, I received many help from various people around me. Without their kind help, I would not have been able to write this dissertation or complete my Ph.D., and I very happily express my thanks and gratitude towards all of them in this small section.

First, I would like to express my immense gratitude towards my supervisor, Prof. Dr. Susanne Lutz, for her enormous support from the very start of my Ph.D. until the last moments of this challenging journey. Susanne taught me how to put reason and argument scientifically. She has been always available to help me out with many different kinds of questions, problems, and puzzles.

Other than scientific support, I also got huge moral support from her to be able to work in a very competitive research environment. I have no hesitation to state that without her continued support, the goals of this project would have never been realised.

In this respect, I would also extend thanks to my co-supervisors, Prof. Dr. Thomas Meyer, to answer all my questions about Smad signaling, and Prof. Dr. Jürgen Brockmöller for guiding me through chemical-structural aspects of pharmacology. Their valuable input, expert opinion, skilled suggestions, and constructive criticism have added a lot to my knowledge.

I was very lucky to be able to participate in several cardiac and pharmacological communities, conferences, department meetings, and events where I presented parts of my research. I would like to thank all the audiences, referees, and visitors who provided their valuable input on my presentations, talks, and, discussions. It all proved to be very reinforcing and reviving. Being a member as a young scientist at the Deutsches Zentrum für Herz- und Kreislaufforschung (DZHK), I thank all the support and knowledge that I got from there. I would also like to thank our director, Prof. Dr. Wolfram Hubertus Zimmermann, for his valuable suggestions and encouragement.

Thanks to the scholarship provided by the Higher Education Commission of Pakistan (HEC), and Deutscher Akademischer Austauschdienst (DAAD) that I was able to work on my dream, Ph.D. I am also thankful to both the organizations to let me travel around the world and especially, the whole of Germany.

Thanks are also due to my departmental and lab colleagues including Elif Levent, Gabriela Leão Santos, Naim Kittana, Josephine Ralph, Fredrica Mayer, Robin Anaton, Alisa DeGrave, Sara Al Disi, Fatima Kanwal, and many other members, for their moral and technical support in providing a friendly and constructive environment.

I also thank Zeeshan, Imran, Zafar Iqbal, Umair Amin, Umair Latif, Umer, Shafique, Shahbaz and Saleem for their friendship, and kind support in all matters of this journey.

I was lucky enough to have a full spectrum of support from my beloved parents, for having supported me for the whole of my life. My wholesome thanks also extend to my siblings, especially my brother, Shahid Maqsood, who has been making tons of things possible for me, over the years. It may not be enough to express the thanks, gratitude, and love that I owe to them all.

Finally, I want to thank my love, my wife, Sumrah, whose great care, patience, love, and support have been countless to achieve this goal, especially during the final stage of this dissertation. I realise, many often you felt you had to share me with medicines. I am glad that now we are able to spend more time together. Lastly, heartfelt thanks to my cutie-pie, Aleen, for being always involved with me and making this journey very pleasant. With all my love, this book is dedicated to my family.

November, 2020
Göttingen

Table of contents

List of Figures

List of Tables

List of abbreviations

ACEI	Angiotensin converting enzyme inhibitor
AF	Atrial fibrillation
ANOVA	Analysis of variance
APS	Ammonium persulfate
AT	A combination of angiotensin II and transforming growth factor beta
AT_1R	Angiotensin II type 1 receptor
AT_2R	Angiotensin II type 2 receptor
ATF6	Activating transcription factor 6
AUC	Area under the curve
bFGF	Basic fibroblasts growth factor
BiP	Binding-immunoglobulin protein
BSA	Bovine serum albumin
BTP2	SOCE inhibitor (YM-58483; [N-{4-[3,5-Bis(trifluoromethyl)-1H-pyrazol-1-yl]phenyl}-4-methyl-1,2,3-thiadiazole-5-carboxamide])
CCN1	Cellular communication network factor 1
cDNA	Complementary DNA
CF	Cardiac Fibroblasts
CHOP	CCAAT/Enhancer-binding protein homologous protein
CM	Cardiac myocytes
Col1a1	Collagen type I, alpha 1
Col3a1	Collagen type III, alpha 1
CRAC	Calcium release-activated calcium channels
CSA	Cross-sectional area
CsA	Cyclosporin A
CTGF	Connective tissue growth factor
DAG	Diacylglycerol
DAPI	4′,6-Diamidino-2-phenylindole
DDIT3	DNA damage inducible transcript 3
DM	Diabetes mellitus

DMEM	Dulbecco's modified eagle medium
DMSO	Dimethylsulfoxide
DPBS	Dulbecco’s phosphate-buffered saline
ECM	Extracellular matrix
EGFR	Epidermal growth factor receptor
EMT	Epithelial-to-mesenchymal transition
EndMT	Endothelial-to-mesenchymal transition
ER	Endoplasmic reticulum
ET-1	Endothelin-1
FACS	Fluorescence-activated cell sorting
FCS	Fetal calf serum
FGM-3	Fibroblast growth medium-3
FL2-A	Fluorescence pulses area
FL2-W	Fluorescence pulses width
FSC	Forward scatter scale
GAPDH	Glyceraldehyde-3-phosphate dehydrogenase
GPCR	G-protein-coupled receptor
hECT	Human engineered connective tissue
HF	Heart failure
HFpEF	Heart failure with preserved ejection fraction
HFrEF	Heart failure with reduced ejection fraction
HRP	Horseradish peroxidase
HSPA5	Heat shock protein family A member 5
IP3	Inositol 1,4,5-trisphosphate
IP3R	Inositol 1,4,5-trisphosphate receptor
IRE1	Inositol-requiring enzyme 1
LAP	Latency-associated peptides
LTBP	Latent transforming growth factor-β-binding protein
MI	Myocardial infarction
mRNA	Messenger RNA

MyoF	Myofibroblasts
NFAT	Nuclear factor of activate T-cells
NHCF-V	Normal human ventricular cardiac fibroblasts
Orai1	Calcium release-activated calcium modulator 1
Orai2	Calcium release-activated calcium modulator 2
Orai3	Calcium release-activated calcium modulator 3
P/S	Penicillin/streptomycin
PDGFR-α	Platelet-derived growth factor receptor alpha
PDI	Protein disulfide isomerases
PERK	R-like endoplasmic reticulum kinase
PFA	Paraformaldehyde
PIP2	Phosphatidylinositol bisphosphate
PKC	Protein kinase C
PLC-β	Phospholipase C-beta
POSTN	Periostin
Pro-Col1a1	Uncleaved collagen type I, alpha 1
p-Smad2	Phosphorylated Smad family member 2
Pyr3	Pyrazole 3
RAAS	Renin-angiotensin-aldosterone system
ROCE	Receptor-operated calcium entry
ROI	Region of interest
RT-qPCR	Real-time quantitative polymerase chain reaction
SDS	Sodium dodecyl sulfate
SDS-PAGE	Sodium dodecyl sulfate polyacrylamide gel electrophoresis
SERCA	Sarco/endoplasmic reticulum calcium-ATPase
Smad2	Smad family member 2
Smad3	Smad family member 3
SOCE	Store-operated calcium entry
SSC	Side-scatter scale
Stim1	Stromal interaction molecule 1

Stim2	Stromal interaction molecule 2
TCF21	Transcription factor 21
TEMED	Tetramethylethylenediamine
Tgfbr1	TGF-β receptor type I
Tgfbr2	TGF-β receptor type II
TGF-β	Transforming growth factor beta
TGN	Thapsigargin
TRPC1	Transient receptor potential canonical channel 1
TRPC3	Transient receptor potential canonical channel 3
TRPC4	Transient receptor potential canonical channel 4
TRPC6	Transient receptor potential canonical channel 6
TRPM4	Transient receptor potential channel sub-family M member 4
UPR	Unfolded protein response
α-SMA	Actin alpha 2, smooth muscle
ΔRFU	Change in fluorescent intensity

List of symbols and units

α	Alpha
β	Beta
γ	Gamma
µM	Micromolar
µl	Microliter
sec	Second
ºC	Centigrade
nM	Nanomolar
ng	Nanogram
mm^3	Cubic Millimeter
mm^2	Millimeter square
ml	Milliliter
min	Minute
mg	Milligram
M	Molar
L	Liter
h	Hour
g	Gram
cm	Centimeter
%	Percentage

1. Summary

Cardiac fibrosis is a serious health problem commonly associated with cardiovascular diseases and remains an increasing health burden around the globe. The development of cardiac fibrosis involves the activation and differentiation of mainly resident cardiac fibroblasts (CF) by biochemical factors including angiotensin II (Ang II) and transforming growth factor β (TGF-β). As both factors were shown to interfere with the Ca^{2+} handling in CF, the role of Ca^{2+} influx mechanisms were studied in 2D and 3D cultures of CF.

In a first step, the influence of the inhibition of the store-operated calcium entry (SOCE) and the transient receptor potential channel canonical 3 (TRPC3) by BTP2 (YM-58483) and Pyr3 (Pyrazole 3), respectively, on the Ca^{2+} handling were determined in 2D cultured normal human ventricular cardiac fibroblasts (NHCF-V). Both inhibitors were shown to reduce the basal and Ang II-dependent Ca^{2+} oscillations, as well as the Ang II-induced Ca^{2+} transients. Moreover, BTP2 was demonstrated to reduce the TGF-β-dependent Ca^{2+} transient and the ER calcium content under basal condition. Long-term treatment indicated that BTP2 and Pyr3 inhibited the proliferation of NHCF-V and induced cytotoxic effects in 2D cultured cells. An important difference between both inhibitors were identified for their effects on the pro-fibrotic gene expression. BTP2 blunted the expression of the major cardiac collagen isoform Col1a1, but Pyr3 was without effect. BTP2 also down-regulated the matricellular protein connective tissue growth factor (CTGF). Importantly, BTP2 increased the expression of important effectors of the unfolded protein response (UPR).

In the next step, the NHCF-V were used to generate human engineered connective tissues (hECT). To induce cell activation a co-treatment with Ang II and TGF-β (AT) was applied. This treatment was shown to increase hECT compaction, contraction, stiffness, and strength, and to decrease extensibility. In the following, the anti-fibrotic potential of BTP2 was shown by a significant reduction of the AT-induced compaction, contraction, stiffness, and strength, and by an increase in elasticity and extensibility of the fibrotic hECT. Molecular analysis revealed that BTP2 treatment resulted in enhanced cell loss within the initial culture period and a downregulation of Col1a1. Mechanistically, BTP2 induced mild ER-stress indicated by an up-regulation of the UPR mediator DDIT3. Finally, Pyr3 also significantly reduce the AT-induced contraction and stiffness but surprisingly, none of the other biomechanical parameters.

In summary, the BTP2-dependent Ca^{2+} influx inhibition induced ER-stress which interfered with ECM protein expression and fibrotic processes in hECT, whereas, Pyr3 interfered only with the contractile behavior of NHCF-V.

2. Introduction

2.1 Cardiac fibrosis and heart diseases

Heart diseases are a major health burden around the globe irrespective of the developmental status of a society. It is estimated that at least 26 million people around the world suffer from heart failure (HF) [1, 2]. Even worse, a recent study has demonstrated that the survival rate of patients with HF has not been improved in the last 20 years [3]. The major cause of mortality in heart diseases is coronary artery disease and consequently myocardial infarction (MI) often resulting in HF [4, 5]. Independent of the initial condition, including hypertension, chronic ischemia, MI and valve abnormalities, the heart undergoes a structural remodeling which leads over time to HF. Cardiac fibrosis underlies nearly all conditions leading to HF and correlates with long-term mortalities of heart diseases [6-9]. Moreover, cardiac fibrosis may serve as a diagnostic marker and therapeutic target for HF with preserved ejection fraction (HFpEF) that represents 50% of patients with symptomatic HF [10]. It has also been shown that adverse cardiac remodeling is directly related to the development of HF with reduced ejection fraction (HFrEF), and biomarkers of collagen synthesis and degradation indicate worsening of the disease [11]. In another study on non-ischemic cardiomyopathies, it has been shown that, in the absence of pre-existing HF, the prevalence of non-ischemic myocardial fibrotic conditions poses a higher risk of HF, hospitalization, and death compared to non-fibrotic conditions. [12].

Cardiac fibrosis is a pathological condition that commences as a part of the inflammatory response and it is a final common process in HF [10, 13-15]. Cardiac fibrosis is characterized by a dysregulated balance between synthesis and turnover

of matrix proteins, especially collagens, that results in extensive morphological and functional abnormalities of the heart. The deposition of collagens initially results in ventricular stiffness and diastolic dysfunction as well as the progressive remodeling of the ECM over time leads to systolic inefficiencies and ultimate HF [9, 16]. The myocardium of the mammalian heart has negligible regenerative potential that favors adaptive changes to perpetuate its functions. After acute MI, the sudden loss of cardiomyocytes (CM) and the occurring inflammation trigger fibrotic responses in an attempt to heal the wound and to reduce the risk of wall rupture [17, 18]. However, prolonged “healing” responses following MI lead to fibrosis, resulting in diastolic dysfunction, arrhythmias, and HF [19, 20]. Moreover, chronic myocardial wall stress conditions like hypertension, aortic stenosis or other valvular heart diseases result in slowly progressing cardiac fibrosis [9]. The persistent stress on the ventricular wall gradually leads to maladaptive ECM remodeling and ventricular dilatation that eventually results in combined diastolic and systolic HF [9, 17, 18, 21].

There are two principal types of cardiac interstitial fibrosis, reparative or also called replacement fibrosis, and reactive fibrosis. In reparative fibrosis, dead CM are replaced with microscars, mainly causing the diastolic dysfunction. Whereas, in reactive interstitial fibrosis, fibrous mass accumulates in the perivascular spaces surrounding intramural arteries and replaces normal thin ECM layer around muscle bundles with thick sheaths that impairs conduction, perfusion and contraction [22-24]. Most often, CM death is the main trigger for reparative fibrosis whereas reactive fibrosis occurs in multiple cardiac diseases like arterial hypertension and

other conditions of pressure overload, ischemia, and extracardiac disease conditions including diabetes mellitus (DM) and chronic kidney disease [9, 25].

The poor understanding of the pathogenesis of cardiac fibrosis is a hindrance to an approved treatment for it. On the cellular level, it is now established that the differentiation of cardiac fibroblast to myofibroblast is the key process that leads to cardiac fibrosis [9, 14, 17, 26, 27]. This differentiation is i.e. driven by neurohormonal pathways including the renin-angiotensin-aldosterone system (RAAS), adrenergic signaling as well as by different growth factors and cytokines. All these factors work together and synergistically modulate the ECM, thus inducing cardiac fibrosis [24, 28].

2.2 Cardiac fibroblasts (CF) – function and origin

The word fibroblast is derived from the Latin '*fibra*' (fiber) and Greek '*blast*' (germ, bud, cell) describing fibroblasts as fiber-secreting cells. By morphology, CF are flat spindle-shaped cells lacking a basement membrane and having multiple processes [29]. CF are anatomically interspaced as strands or sheets between CM in the myocardium. Their primary role is the maintenance of the architecture of the heart by producing and secreting structural and regulatory components of the ECM. In addition, CF were shown to be important for mechanical force transmission, vasomotor reactivity of the coronary microvasculature, and for the insulation of independent electrical conduction systems in the atria and ventricles [4, 30-33]. In line with these basal functions, it has been shown that the embryonic loss of CF results in a substantial disruption of the myocardial structure and function [34, 35].

During development, the heart is devoid of CF until the formation of the primitive heart tube, then fibroblast progenitors enter into the four chambers of the heart. Developmentally, CF are mesenchymal in origin and derived from epicardial and endothelial cells. Epicardial-derived CF emerge by epithelial-to-mesenchymal transition (EMT) and constitute over 80% of atrial and ventricular fibroblasts. The second source of CF relays on endothelial-to-mesenchymal transition (EndMT). These EndMT-derived cells constitute less than 20% of the CF and mainly reside in the right ventricle and ventricular septum [36, 37]. A third but minor source of CF is derived from the neural crest, from where they mainly populate the right atrium [37, 38]. Recent progress in lineage tracing and cell identification revealed that independent of the origin, CF are the third most abundant cell type in the adult heart after endothelial cells and cardiomyocytes. They account for around 15% of the non-myocyte population in the mouse heart, which is approximately 10% of all myocardial cells [39]. Their contribution to the human heart by number is, however, still not known.

Improvements in our understanding of the origin and proportion of CF in the heart was mainly based on progresses made in cell identification. Although there is still no marker available which is unique to CF, the cells can be identified by marker combinations including the markers TCF21 and PDGFR-α [33].

2.3 Cardiac myofibroblasts (MyoF) – function and origin

Myofibroblasts (MyoF) represent the diseased, highly secretory phenotype of CF in the injured heart. Morphologically, MyoF are larger than fibroblasts and possess ruffled membranes [40]. To meet the higher secretory demand, MyoF have an extensive ER, which covers most of the cell [41]. A typical characteristic of MyoF is

the expression of α-smooth muscle actin (α-SMA), which enables the cells to establish their contractile function. MyoF interact with the ECM through integrins, which are organized in super-mature focal adhesions and are linked to α-SMA-containing stress fibers. This contractile setup of MyoF potentiate wound closure [42]. In addition to their contractile function, MyoF are the main source of structural ECM components, predominantly of collagens, in the diseased heart and thus they are in charge to replace dead CM by ECM after myocardial injury [27, 43, 44].

Recent lineage tracing studies have shown that resident CF are the major source of MyoF after myocardial injury [45], however, secondary sources like EndMT-derived cells as well as hematopoietic and pericyte originated cells exist [46, 47]. The transdifferentiation of CF into MyoF is a multi-step event. A loss of the structural integrity of the myocardium after injury exposes the resident CF to mechanical and biochemical stress that facilitate CF proliferation and migration to the injured area. These cells are considered to be activated fibroblasts or proto-MyoF, which then further transdifferentiate into MyoF [27, 48]. Recent single cell sequencing studies have demonstrated that cells with different phenotypes can be present in the diseased mouse heart at the same time [49-51]. This is probably also true for the diseased human heart as it was shown that two types of α-SMA-positive MyoF could be isolated from explanted terminal HF hearts, namely proliferating and non-proliferating cells.

The fate of MyoF in the fibrotic heart is not fully elucidated, especially not in the setting of pressure-overload. However, it was shown that after MI the amount of α-SMA-positive cells in the scar is markedly reduced [43], possible reasons are cell

death or as recently suggested a further differentiation step into α-SMA-negative matrifibrocytes [48, 52].

Same as for quiescent CF, no exclusive markers exist for the disease-related CF phenotypes. Nowadays, a combination of α-SMA, Col1a1, and POSTN is suggested for the identification of activated fibroblasts and MyoF [33]. A discrimination between these both phenotypes is, however, difficult as changes in gene expression are continuous, accordingly it was demonstrated by single cell RNA sequencing [49-51]. Interestingly, in the mouse heart identified markers for the late-stage matrifibrocytes are genes involved in ossification [48]. So far, it is not clear if a similar gene activation occurs in the terminal maturation of the scar in the human heart.

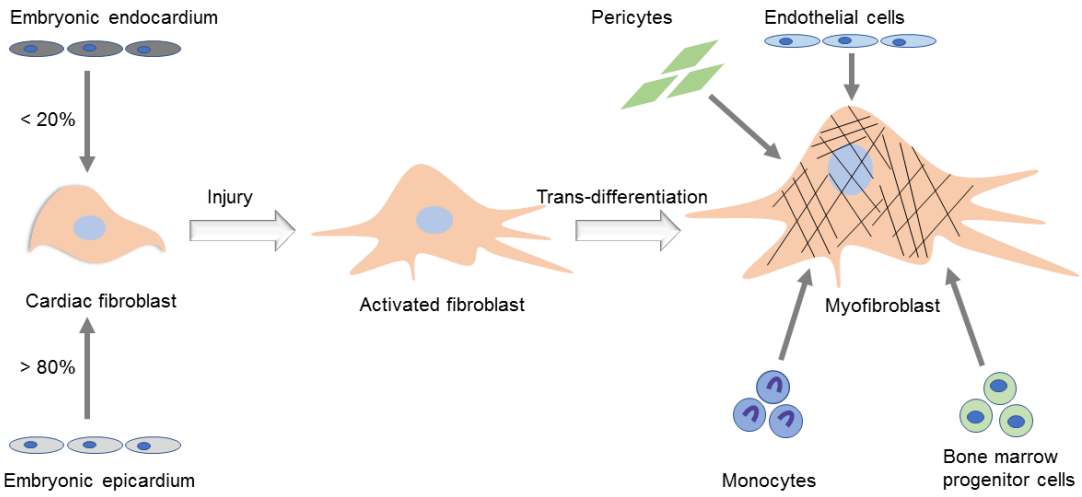

Figure 1: Developmental sources and activation of cardiac fibroblasts.

There are two documented sources of CF, epicardial and endothelial. The resident CF are the major source of activated CF and MyoF after injury. Other minor

sources of MyoF include monocytes, pericytes, endothelial and bone marrow progenitor cells. The contribution of these minor sources is still under investigation. (adopted from Tallquist MD and Molkentin JD, 2017).

2.4 Regulation of fibrosis by pro-fibrotic mediators

Cardiac fibrosis and thus cardiac fibroblast activation is induced by many bio-active factors. Amongst the most important ones are Ang II, as a mediator of the endocrine and local renin-angiotensin-aldosterone system (RAAS), and the cytokine TGF-β. The regulation and outcome of both factors have been shown to be complexly interlinked [53-55].

2.4.1 Pro-fibrotic signaling induced by Ang II

Ang II acts not only as an important physiological mediator, but plays also a role in pathological processes including cardiac fibrosis [56]. In fact, Ang II generation and signaling are the only targeted processes in the current therapy of cardiac fibrosis in heart failure. Angiotensin-converting enzyme inhibitors (ACEI) and Ang II-type1 (AT_1R) receptor antagonists are among the indispensable therapeutics in the current treatment regimen.

The anti-fibrotic action of these two drug classes is mainly based on the prevention of the activation of the AT_1R in the heart. This G-protein-coupled receptor (GPCR) is the predominantly expressed Ang II receptor in the adult mammalian and is considered to be largely responsible for the pathological effects of Ang II. Its isoform AT_2R, in contrast, seems to be mainly involved in developmental processes, although there are few data suggesting a role opposing to the AT_1R in cardiovascular diseases [57].

The AT_1R is a promiscuous receptor, which can activate several types of heterotrimeric G proteins including $G_{q/11,}$ $G_{12/13,}$ and G_i. Most data are probably available on the contribution of the AT_1R-$G_{q/11}$ pathway to fibrotic processes in CF and their derivatives. Downstream of $G_{q/11}$ either the monomeric G protein RhoA can be activated or the canonical phospholipase C-β (PLC-β) pathway, both resulting in CF activation [58-64]. Especially, indications of the contribution of the PLC-β/calcium pathway are available since several decades. PLC-β is an enzyme which cleaves phosphatidylinositol bisphosphate (PIP2) into inositol trisphosphate (IP3) and diacylglycerol (DAG) and by this diversifies the downstream signaling: i) IP3 results in a transient release of calcium by IP3 receptors at the ER membrane, ii) DAG activates together with calcium certain isoforms of the protein kinase C family (PKC), and iii) DAG was demonstrated to activate specific transient receptor potential canonical channels (TRPC channels) at the plasma membrane, which allow the influx of calcium and sodium [65-67]. All these processes have been already assigned to fibrotic processes *in vitro*, including cell proliferation and collagen production [68-70]. In some cases, the observed effects were suggested to be indirect, resulting from the transactivation of other receptors like the epidermal growth factor receptor (EGFR) [71].

The pro-fibrotic effect of Ang II *in vivo* is well known and used in an important heart disease model in which Ang II is applied to animals by implanted osmotic minipumps for several days or weeks. Hundreds of studies demonstrate that Ang II application leads to the induction of cardiac fibrosis, even when the blood pressure is not increased (first demonstrated) [72, 73]. Although this is a well-established model, there are almost no *in vivo* data available on the importance of downstream

mediators of the AT_1R-$G_{q/11}$ pathway in CF activation and cardiac fibrosis. One reason for this is based on the long-time missing cell type-specific models allowing for a targeted deletion or overexpression of genes in cardiac fibroblasts and their derivatives. With having now the possibility to modify gene expression more specifically with the help of *Tcf21*-Cre (CF) and *Postn*-Cre (MyoF) transgenic animals, it is expectable that future studies will help to better understand the contribution of the AT_1R-$G_{q/11}$ pathways to cardiac fibrosis [45, 74, 75].

2.4.2 Pro-fibrotic signaling induced by TGF-β

The TGF-β family comprises the three members TGF-β1, TGF-β2, and TGF-β3, which have all been found to play a role in the development of the heart and in heart disease [76]. During development TGF-β induces EMT as well as EndMT, both fundamental processes in cardiac fibroblast maturation as described above. In the diseased adult heart TGF-β functions as one of the strongest pro-fibrotic factors [77].

TGF-β is an emergency signal, which does not rely on *de novo* induction after a cardiac insult like MI. It was shown that TGF-β is stored in its inactive latent form in CM and in the ECM in the healthy heart, and thus it represents a stand-by trigger for repair [78, 79]. After an insult, the latent TGF-β pool is activated. This latent form consists of a TGF-β dimer, two latency-associated peptides (LAP), formerly parts of the two pro-TGF-β proteins, and a latent TGF-β-binding protein (LTBP). The LTBP is especially important to confer the ECM-associated localization of the complex. The corresponding activation mechanism of latent TGF-β may include diverse proteases, like matrix metalloproteinases, as well as integrin-dependent binding to LAP, eventually releasing active TGF-β [80].

In addition to latent TGF-β activation, the TGF-β pool is enriched by other cells in the myocardium after injury, including platelets, macrophages, and amongst others by activated CF and/or MyoF [81-84]. Therefore, CF are not only activated by TGF-β, but their diseased derivatives also contribute to the production of TGF-β, which results in autocrine signaling loop.

TGF-β elicits its effect through a heterodimeric receptor consisting of a TGF-β receptor type I (*Tgfbr1*) and type II (*Tgfbr2*) [85-87]. In CF and MyoF, it was shown that a targeted deletion of both receptors resulted *in vivo* in a strong reduction in cardiac fibrosis after pressure overload. Moreover, the same study demonstrated that a double knockout of the canonical TGF-β receptor downstream mediators Smad2 and Smad3 had a comparable effect on fibrosis. The Smad2/3 knockout in MyoF further resulted in a reduction in SMA-positive MyoF, in activated CF/MyoF proliferation, and in the repression of the expression of ECM components and modulators. Interestingly, the authors also showed that Smad2 is dispensable in this setting [88]. This rather recent study impressively demonstrates with the help of a cell-targeted approach the necessity of TGF-β signaling for cardiac fibrosis *in vivo*, and by this confirms the many other studies which have directly or indirectly demonstrated that TGF-β is a master regulator in this process.

Although the importance of TGF-β in cardiac fibrosis is a well-accepted fact, there is currently no approved therapeutic approach available interfering with this pathway in the diseased heart. The first attempt to tackle this problem is currently undertaken by evaluating the effectiveness of Pirfenidone in a clinical trial in the treatment of HFpEF [89]. Pirfenidone is an approved drug for the treatment of

idiopathic lung fibrosis and is suggested to interfere with TGF-β signaling, however, by an unclear mechanism [90].

2.4.3 Cross-regulation of TGF-β and Ang II signaling in CF/MyoF

There are several lines of evidence that TGF-β and Ang II signaling pathways are interlinked in CF and their pathological derivatives (CF/MyoF will be used in the following as the cellular phenotype of 2D cultured cells is often not carefully assessed). The most intuitive link is based on a regulation of the expression of TGF-β by Ang II in cultured CF/MyoF [53, 91]. Moreover, Ang II was shown to increase the expression of Endoglin, which is a homodimeric type III TGF-β1 receptor, and of Smad3 phosphorylation in cultured CF/MyoF [92-94]. Similar observations exist in *in vivo* studies, however, due the complexity of the *in vivo* situation a clear assignment of the observed interaction between both pathways to the CF/MyoF fraction is largely impossible [95], [96].

2.5 Calcium regulation in CF/MyoF

Calcium is a versatile second messenger involved in many cellular processes including gene expression, contraction and secretion. As already described above, in CF/MyoF the Ang II-dependent regulation of calcium is probably of high importance. Ang II was shown to induce calcium transients via the canonical AT_1R/PLC-β/IP3 pathway in cultured CF/MyoF from different species including mouse, rat, rabbit and human [65, 97]. In addition to the intracellular release of calcium from the ER, calcium entry via plasma membrane channels is discussed for CF/MyoF. Here it can be discriminated between voltage-gated, receptor-operated, and store-operated channels. The presence of voltage-gated channels in CF/MyoF is relatively unlikely. Mainly effects based on the use of voltage-gated

channel blockers on the behavior of the CF/MyoF were used as an argument for their existence, however, the corresponding currents have never been documented [98-100]. In contrast, receptor-operated channels like different members of the TRPC channel family and store-operated channels are more likely to play role in CF/MyoF.

2.5.1 Receptor-operated calcium entry in CF/MyoF by TRPC channels

TRPC channels form a family with seven distinct members, named as TRPC1 to 7. They are all non-selective cation channels with variable calcium/sodium permeability ratios (P_{Ca}/P_{Na} = 1-10) [101]. These channels were shown to play a role in the receptor-operated calcium entry (ROCE) as well as in store-operated calcium entry (SOCE). In addition, a potential role in mechanosignaling was discussed [102, 103]. In CF/MyoF, all seven TRPC could be detected on mRNA level [65, 104] and TRPC1, 3, 4, and 6 were as well detected on protein level in human CF/MyoF [105]. Amongst these only the DAG-regulated TRPC3 and TRPC6 were described so far to play a role in fibrotic processes in CF/MyoF.

The existence of a PLC-β-sensitive, non-selective cation current in freshly isolated cardiac fibroblast was firstly described in 2007 [66]. In the following it was shown that this current could be inhibited by the TRPC3 inhibitor pyrazole 3 (Pyr3) [106] and that it contributed to the calcium entry in CF/MyoF after Ang II treatment. Moreover, Pyr3 inhibited cell proliferation and α-SMA expression. In the same study, it was shown that TRPC3 expression declined in ventricular rat cells during culture, but was increased in atrial CF/MyoF from dogs with atrial fibrillation (AF) [70]. In line with the pro-fibrotic function of TRPC3, its global knockout in mice suppressed the induction of cardiac fibrosis, but not of hypertrophy in response to

pressure overload [107]. Mechanistically, the extracellular signal-regulated kinases and RhoA were identified to mediate the pro-fibrotic responses of TRPC3 in AF and pressure overload, respectively [70, 107].

The role of TRPC6 in cardiac fibrosis is controversially discussed. On one hand, TRPC6 was found to exert anti-fibrotic functions under pro-fibrotic conditions in CF/MyoF. TRPC6 expression was induced by endothelin-1 (ET-1) in rat CF/MyoF, which resulted in an increased receptor-dependent calcium influx, a sustained activation of the nuclear factor of activated T-cells (NFAT) via calcineurin, and an anti-fibrotic regulation of α-SMA and collagen [108]. On the other hand, TRPC6 overexpression induced the expression of α-SMA in the same cell type as used in the ET-1 study, and its global knockout resulted in a higher incidence of ventricular wall rupture after MI in mice. The pro-fibrotic effect of TRPC6 was interestingly also assigned to the activation of NFAT [109]. The pro-fibrotic effect of TRPC6 was later confirmed with human right ventricular CF/MyoF [110].

Very recently, the existence of the Ang II-induced ROCE via TRPC channels in CF/MyoF was challenged by a study using isolated TRPC1-7 hepta knockout CF/MyoF from mice, where no influence on the Ang II-induced calcium regulation could be found. A contribution of the store-operated calcium entry (SOCE) was suggested instead [65].

2.5.2 Store-operated calcium entry in CF/MyoF

The mechanism of SOCE is required to prevent the calcium depletion of the ER. Two protein families are mainly involved to form and properly localize these

selective calcium release-activated calcium (CRAC) channels, namely Orai proteins and the stromal interaction molecules (Stim) [111].

The Orai family comprises the three channel pore forming members Orai1, Orai2, and Orai3. All three could be detected on RNA level in healthy and diseased human myocardium as well as in cultured human CF/MyoF [104, 112]. Orai1 was also detected on protein level in cultured human CF/MyoF isolated from healthy and failing hearts. Interestingly, Orai1 expression was higher in CF/Myo isolated from failing hearts, however, total Orai1 expression in male but not female failing myocardium seemed to be decreased [112, 113]. No data are available on the protein levels of the other two Orai isoforms. The same studies, further investigated the expression of Stim proteins, which function as calcium sensors in the ER and are essential for the regulation and positioning of Orai [112]. The studies could show that Stim1 and Stim2 can be detected on RNA level in the healthy and failing myocardium, Stim1 RNA was detected in cultured human CF/MyoF, and Stim1 protein was detected in human CF/MyoF isolated from the healthy and failing heart. In the isolated cells, no differences were detectable on protein level, but on RNA level Stim1 but not Stim 2 was higher expressed in the failing myocardium [104, 112, 113]. *In vitro* and *in vivo* up-regulations of Orai1 and Stim 1 have been also presented for mouse CF/MyoF induced by Ang II [61]. Additionally, Orai1 was found to be higher expressed in mouse hearts after pressure overload [114].

The role of the SOCE in cardiac fibrosis is poorly investigated. The above mentioned study of Ross and colleagues with isolated human CF/MyoF from healthy and failing hearts demonstrated that there is not only a higher expression

of Orai1 in cells from failing hearts, but also an increased calcium influx after inhibition of the ER calcium ATPase SERCA by thapsigargin. Moreover, the co-localization of Orai1 and Stim1 was enhanced in these cells arguing for a greater channel activity. And finally, with the help of the SOCE inhibitor YM-58483 (alias BTP2) they could block the higher collagen secretion from CF/MyoF from failing hearts was shown [113]. Similar anti-fibrotic effects were found by SOCE inhibition with SKF96365 as well as by knockdown of Orai1 or Stim1 in mouse CF/MyoF treated with Ang II. Here the expression of the connective tissue growth factor (CTGF), α-SMA, and fibronectin could be blocked. Moreover, the Ang II-dependent induction of TGF-β and of Smad2/3 phosphorylation was prevented [61].

The importance of the CRAC channel *in vivo* is given by more indirect approaches. Mice with a global deletion of Orai1 developed rapid dilated cardiomyopathy without signs of fibrosis [115], and the use of the Orai1 channel inhibitor JPIII reduced the expression of the most abundant collagens Col1a1 and Col3a1 after pressure overload [114].

Finally, in addition to the disease-regulated expression of the CRAC channel components, age-related changes in channel activity might also exist. Mohis and colleagues have recently reported that aging (age above 50) results in an increase in SOCE in isolated healthy human CF/MyoF, however, without being accompanied by an increase in channel component expression. The underlying mechanism needs therefore further investigation [116].

Small molecule inhibitors of the SOCE

The SOCE machinery provides multiple targets for pharmacological interventions [117]. A number of CRAC inhibitors have been developed, however, many of them with poorly characterized mechanisms of action and often with discussable specificities. For example, lanthanum (La^{3+}) and gadolinium (Gd^{3+}) can completely block the SOCE, but with poor channel selectivity [118, 119]. Antimycotic compounds like SKF96365, miconazole and econazole have also been shown to exert non-selective SOCE inhibitory activities [120].

The pyrazole compounds BTP1-3 were initially used as immunosuppressants to inhibit IL-2 production and the calcineurin-independent NFAT translocation to the nucleus in T-cells [121, 122]. However, later on it was confirmed that BTP2 (YM-58483) can potently inhibit the thapsigargin-induced Ca^{2+} influx in T-cells with an IC_{50} of around 100 nM [123]. The mechanism of action of BTP2 is not clear, but as BTP2 exerts its effect extracellularly it might interact with Orai but not with Stim [124]. There are data which suggested that BTP2 can have effects on other cation channels at the plasma membrane, including an activation of TRPM4 and an inhibition of TRPC3 and TRPC5 [125, 126]. BTP2 has been already used *in vivo*, mainly for targeting immune cells where it showed anti-inflammatory properties [127-129].

The recently presented selective inhibitors GSK-5503A and GSK-7975A of Orai1 and Orai3 might have a better specificity, but were found to have a rather low potency with an IC_{50} of around 4 µM [130].

Finally, the above-mentioned inhibitor JPIII was described to be Orai1-specific with an IC_{50} of 240 nM. Its specificity was tested against multiple other types of other calcium-permeable channels [114].

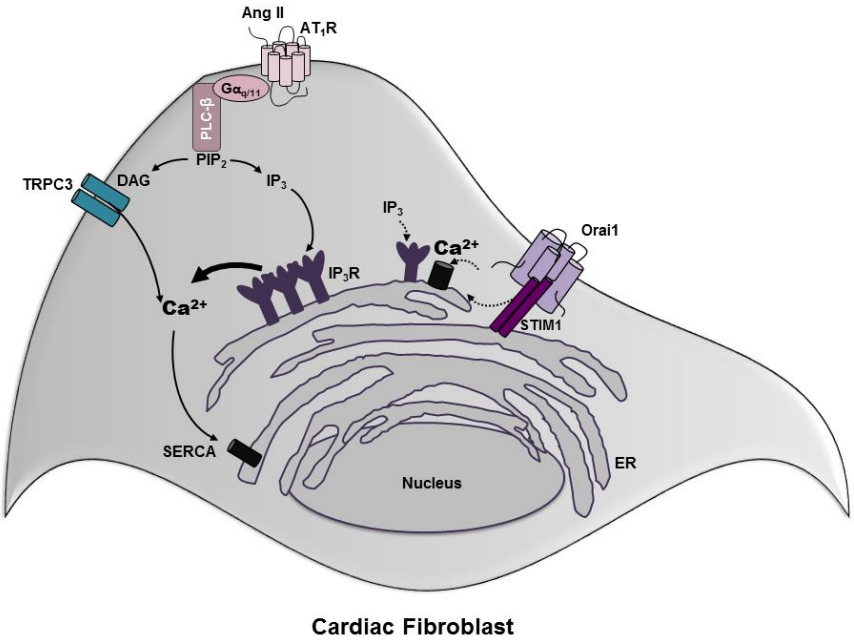

Figure 2: Calcium release and influx in cardiac fibroblast.

Agonist-dependent activation of $G\alpha_{q/11}$ /PLC-β/IP3 pathway release ER Ca^{2+} resulting in translocation of STIM1 from ER to PM to form STIM1-Orai1 complexes for Ca^{2+} influx. Generation of DAG directly activates TRPC3 channels for Ca^{2+} influx.

2.5.3 Calcium oscillation in CF/MyoF

Despite the time-restricted, receptor-induced calcium transient, non-excitable cells are able to oscillate calcium spontaneously, often augmented by receptor ligands. Central molecules in the generation of calcium oscillations are thought to be the IP3R, which are biphasically regulated by cytosolic calcium. A small increase in cytosolic calcium leads to receptor activation, whereas a high cytosolic calcium concentration results in receptor inactivation. This might lead to an oscillatory

calcium release from the ER. In addition, after G_qPCR activation a cyclic generation of IP3 was found, which could further contribute to or enhance the oscillation of cytosolic calcium [131-133].

It was suggested that the intracellular calcium stores are the major source for the oscillating calcium. However, there are also data demonstrating that the oscillation is stopped in the absence of extracellular calcium [134, 135]. This suggested that calcium influx either by ROCE or SOCE might help to sustain the oscillation [136-139].

Calcium oscillation can be observed in many cultured cells including CF/MyoF. It was shown that around one third of human CF/MyoF spontaneously oscillated calcium in 2D cultures. Application of fetal calf serum doubled the number and chelation of extracellular calcium completely suppressed the oscillation in all cells. By using La^{3+}, oscillation could be also blocked. Moreover, inhibition of PLC-β, IP3R, plasma calcium ATPases, and of the sodium calcium exchanger negatively influenced it [104]. Calcium oscillations were also detected in around 40% of cultured rat CF/MyoF, and ATP as a GPCR agonist increased the oscillation frequency without changing the amplitude. Interestingly, the calcium oscillation was found to induce a cyclic subcellular contraction of low tension actin stress fibers in rat CF/MyoF [140]. A link between calcium oscillation and a regulation of the actin cytoskeleton was also found in other cells, and importantly the interaction seems to be mutual [141, 142]. Not only the intracellular stiffness of a cell, exerted by the actin cytoskeleton, can have an impact on the oscillation of calcium, but also the stiffness of the culture substrate was shown to influence it [142].

In general, reports on calcium oscillation *in vivo* are rare and restricted to transgenic models expressing genetically encoded calcium indicators. Oscillations were so far found e.g. in smooth muscle cells and in the endothelium of the vessel wall, but nothing is known about CF/MyoF in the myocardium [143, 144].

2.6 ER stress and the unfolded protein response

The ER is the first organelle in the secretory pathway. Here, protein translation, folding and modification of most newly synthesized secreted and membrane proteins takes place. Pathological factors like nutrient and oxygen deficiencies, infections, genetic mutations, altered calcium and redox levels, disturbances in post-translational modification and folding of proteins can affect the proteostasis in the ER and by this induce ER stress [145]. To revert ER stress and regain ER homeostasis or to induce cell death, mammalian cells trigger three highly conserved signal transduction pathways, which are constituting the unfolded protein response (UPR) [146], [147].

One of the most important chaperones in the ER and part of the UPR is the binding immunoglobulin protein (BiP encoded by the *HSPA5* gene). BiP acts especially as a chaperone for misfolded or unfolded proteins and as a silencer for the unfolded protein response (UPR) under homeostatic conditions. When the load of inadequately folded proteins in the ER increases, BiP is released from the three most-upstream UPR regulators, protein kinase R-like endoplasmic reticulum kinase (PERK), activating transcription factor 6 (ATF6), and inositol-requiring enzyme 1 (IRE1), and by this BiP initiates their down-stream signaling cascades. Dependent on the degree of ER stress, the overall net response is either beneficial, leading to a reinstallation of proteostasis e.g. by induction of chaperone expression, or

detrimental, resulting in cell death [148]. Initially the three UPR pathways were suggested to partly overlap in their functions, nowadays evidence is increasing that the elicited effects by the different arms of the UPR can be rather distinct.

2.6.1 Calcium and ER stress

BiP is not only a master regulator of the UPR, it is also an important calcium binding protein. It was shown that high calcium concentrations are necessary to stabilize the binding of BiP to its folding substrates [149]. Other important calcium-dependent ER proteins involved in folding of nascent proteins are protein disulfide isomerases (PDI), which establish and rearrange disulfide bonds, and calreticulin, a calcium buffering chaperone [150, 151]. The interaction of PDI and calreticulin was shown to be as well calcium-dependent [152]. As the protein folding machinery necessary for nascent protein folding and for the correction of misfolded proteins is dependent on the calcium load of the ER, it is easy to understand that ER calcium depletion results in an emergency response like the UPR. Several studies have demonstrated that chemical ER calcium depletion, e.g. by the SERCA inhibitor thapsigarigin, can strongly induce the UPR in divers cell types including fibroblasts [153-156].

For the maintenance of the ER calcium level the SOCE is as well important as SERCA. Interference with SOCE, including deletion or downregulation of Stim, inhibition or downregulation of Orai, resulted in an induction of the UPR and ER stress in different cells [157-162]. *Vice versa*, ER stress was shown to influence SOCE. There are data suggesting that ER stress increases SOCE by a so far unclear mechanism, and oppositely it was shown that ER stress leads to a degradation of Stim2, which reduced SOCE [163, 164].

2.6.2 ER stress and cardiac fibrosis

There are several indications that ER stress plays an important role in fibrotic diseases, e.g. it was suggested to be involved in liver [165], kidney [166], pulmonary [167, 168], and cardiac fibrosis.

In the heart, the UPR was demonstrated to be induced in models of chronic beta-adrenergic activation and Ang II infusion, diabetic cardiomyopathy [169, 170], ischemia/reperfusion injury [171], pressure overload [172], and autoimmune cardiomyopathy [173], which are all associated with cardiac fibrosis. In human myocardial samples, signs of ER stress were detected in the failing heart and in the peri-infarct region [173].

Whether the induction of the UPR is beneficial of detrimental is not clear and probably depends on the intensity of ER stress, the cell type which experiences ER stress, and the UPR pathway involved. For example, in the model of chronic beta-adrenergic activation a general inhibition of the UPR by the chemical chaperone 4-phenylbutyric acid prevented cardiac fibrosis [174], whereas ATF6 induction was shown to act as beneficial mechanism in ischemia/reperfusion resulting in a reduced infarct size [175].

Most studies in the heart field investigated changes in ER stress and the UPR either in myocardial samples or in cardiomyocytes, but only few studies were focusing on the fibroblast component of the heart. As mentioned above, ATF6 is suggested to play a protective role in the heart. Its global deletion increased the fibrotic gene expression after MI in mouse hearts and importantly in the presence of TGF-β in isolated CF/MyoF [176], pointing to a direct role of the UPR in cardiac

fibrosis and potentially in CF to MyoF conversion. This is supported by a study in which a CF-specific genetic alteration of the Hippo pathway resulted in self-sustained cardiac fibrosis *in vivo*. Single cell sequencing demonstrated that an up-regulation of ER stress genes occurred specifically in the MyoF fraction resulting from the modified CF [177].

2.7 Using tissue engineering in cardiac fibrosis research

Most of our current knowledge about the behavior of CF/MyoF is either based on complex *in vivo* models or oversimplified 2D-culture systems. Especially, the latter has the disadvantage that isolated CF transdifferentiate rapidly into MyoF due to the unnatural substrate stiffness and the artificial culture conditions [178, 179]. This makes the use of engineered tissues in this research field so attractive, as the phenotypic drift can be regulated by the 3D-culture condition [180-182]. Further clear advantages are their specific and simplified compositions, scalability, reproducibility, and the possibility to analyze a variety parameters dependent on the research question [183].

Different types and shapes of engineered cardiac fibroblast models were invented so far. The simplest version was based on cell aggregation. Comparison with 2D cultured MyoF and sequential transfer of the cells from the aggregates to 2D substrates and back to aggregates demonstrated that this simple procedure is sufficient to induce distinct changes in gene expression assigned to the different phenotypes of CF and MyoF, however, functional readouts like tissue contraction and biomechanics are impossible to assess [182].

A more complex model is the disc model in which CF together with a hydrogel are used to generate flat discs in cell-culture plates. The discs can be either cultured in the well adhered to the wall, which reflects a constraint situation, or released from the wall, floating in the medium. In this model, tissue contraction is measurable in addition to direct cellular parameters, including gene expression, cell orientation and morphology [184, 185], but still the analysis of biomechanical tissue properties is impossible. More complex are models in which the tissues are fixed to flexible posts or generated in the shape of a ring.

The ring-shaped model is especially convenient for the analysis of biomechanical tissue properties as the tissues can simply be hook in an organ bath to force transducers. Ring-shaped engineered connective tissues (ECT), composed of CF/MyoF and collagen, have been successfully used by our group to investigate the role of certain proteins by gain- and loss-of-function modifications of the embedded cells, for pathway analysis as well as to study the effect of potential anti-fibrotic compounds [60, 181, 186-188]. Importantly for this thesis, the use of TGF-β as a pro-fibrotic stimulus was already verified in rat ECT [181].

2.8 Aim of the project

The heart is a multicellular organ comprising of specialized contractile cells, cardiomyocytes, and other supporting cell populations including CF. Cardiac fibrosis is a hallmark of every heart disease showing poor prognosis with available therapies and palliative measures. In the healthy myocardium, quiescent CF become activated after the injury as a part of the ‘healing’ response. However, prolonged activation of CF leads to fibrosis. Moreover, the auto/paracrine release of pro-fibrotic factors and stiffened myocardium further worsen the fibrosis. This

project aimed to study the influence of Ca^{2+}-influx mechanisms on Ca^{2+} handling and their interference with fibrotic responses in NHCF-V. To accomplish this aim, the influence of SOCE and TRPC3 inhibition was determined on Ca^{2+} oscillation and transient and their impact on fibrosis-associated proteins. Then, the anti-fibrotic potential of Ca^{2+}-influx inhibition was studied in a fibrotic 3D model of human engineered connective tissue (hECT) by rheology. Finally, Ca^{2+}-regulated downstream mediators for ECM protein synthesis and secretion were investigated with a focus on the ER-stress driven unfolded protein response (UPR).

3. Materials and Methods

3.1 Materials

3.1.1 Chemicals and reagents

Table 1: Chemicals and reagents

[N-{4-[3,5-Bis(trifluoromethyl)-1H-pyrazol-1-yl]phenyl}-4-methyl-1,2,3-thiadiazole-5-carboxamide] (BTP2)	Sigma Aldrich
4',6-Diamidino-2-phenylindole (DAPI)	Sigma Aldrich
Acetic acid (100%)	Carl Roth
Acrylamide rotiphorese gel 30 solution (30 % acrylamide/bisacrylamide, mixing ratio 37.5:1)	Carl Roth
Agarose	AppliChem
Ammonium persulfate (APS)	AppliChem
Angiotensin II, human (Ang II)	Sigma Aldrich
Aqua B. Braun	B.Braun
Bromophenol blue	AppliChem
Collagen type I (Bovine)	Collagen Solutions
Cyclosporin A (CsA)	Tocris
Dimethylsulfoxide (DMSO)	Sigma Aldrich
DNA loading buffer (6x)	Thermo-Scientific
Dulbecco’s phosphate-buffered saline DPBS (containing Ca^{2+}, Mg^{2+})	Life Technologies
DPBS (not containing Ca^{2+}/Mg^{2+})	Life Technologies
Dulbecco's modified Eagle Medium (DMEM)	Life Technologies

Ethanol, absolute	Carl Roth
Ethyl-1-(4-(2,3,3-trichloroacrylamide)phenyl)-5-(trifluoromethyl)-1H-pyrazole-4-carboxylate (Pyr3)	Sigma Aldrich
EvaGreen dye for qPCR	Solis Biodyne
Fetal calf serum (FCS)	Life Technologies
Fibroblast growth medium-3 (FGM-3)	PromoCell
GeneRuler 1 Kb DNA ladder	Thermo-Scientific
GeneRuler 1 Kb plus DNA ladder	Thermo-Scientific
Glycerol	AppliChem
Glycine	AppliChem
Hoechst 33342	Invitrogen
Igepal CA-630	Sigma Aldrich
Isopropanol	Carl Roth
Methanol	Carl Roth
Paraformaldehyde (PFA)	Sigma Aldrich
Penicillin/streptomycin (P/S)	Life Technologies
Ponceau S	Sigma Aldrich
Propidium Iodide	Sigma Aldrich
Roti-block (10x)	Carl Roth
Roti-immunoblock (10x)	Carl Roth
Roti-mark standard, protein molecular weight marker	Carl Roth
Roti-Nanoquant (Bradford reagent)	Carl Roth

Sodium chloride (NaCl)	AppliChem
Sodium dodecyl sulfate (SDS)	AppliChem
Sodium hydroxide (NaOH)	Carl Roth
ß-Mercaptoethanol	AppliChem
Tetramethylethylenediamine (TEMED)	Merck
TGF-β human (Recombinant)	Protech
Thapsigargin (TGN)	Calbiochem
Tris ultrapure (Tris base)	AppliChem
Triton X-100	Carl Roth
Trypan blue	Fluka
TrypLE Express (1X)	Life Technologies
Tween 20	Carl Roth
Water (nucleases-free, not DEPC-treated)	Thermo-Scientific

3.1.2 Consumables

Table 2: Consumables

Name of Article	Specifications	Manufacturer
Cell scrapers	16, 25 cm	Sarstedt
Cell strainers	0.45, 0.70 µm	Sarstedt
Combitips Advanced PCR clean	0.2 ml	Eppendorf
Cryo tube	1.8 ml	Thermo-Scientific

Falcon polystyrene round bottom	5 ml	Corning
Filtration sets	250, 500, 1000 ml, 0.22 µm	Corning
Flexitip pipette tips	0.5-200 µl	Peqlab
Micro-Amp optical adhesive films	PCR compatible	Applied Biosystens
Micro-Amp optical reaction plates	384-well	Applied Biosystens
Microscope glass cover slips	21, 22 mm	Thermo-Scientific
Microscopic slides	Super Frost Plus	Thermo-Scientific
Multi-well cell culture plates	6, 12, 24-well	Greiner Bio One
Multi-well cell culture plates Nunclon delta surface	6, 12, 24-well	Thermo-Scientific
Multiwell, flexible two poles, tissue casting plates (Ref No. 0727-001-001)	48-well	TPK-Kunststofftechnick
Nitrocellulose membrane, Whatman, Protran	Pore size 0.2 µm	GE Healthcare
PCR reaction tubes	0.2 ml	Applied Biosystens
Pipette tips	1, 100, 200, 1000 µl	Sarstedt
Pipette tips with filters (Tip One)	10, 100, 200, 1000 µl	Starlabs
Reaction and centrifuge tubes	15, 50 ml	Greiner Bio One
Reaction tubes	0.5, 1.5, 2 ml	Eppendorf

Serological pipettes	1, 2, 5, 10, 25, 50 ml	Sarstedt
Sterilization filters	0.20 µm	Sarstedt
Syringes	1, 10, 25 ml	BD
Tissue culture dishes	10, 15 cm	Greiner Bio One
Tissue culture Flasks	25, 75, 175 cm	Sarstedt

3.1.3 Culture Media

Table 3: Composition of media used for cell and tissue culturing

Name	Composition
10x DMEM (Serum free) (100 ml)	18.35 g DMEM Sterile water to make up to 100 ml (filtered with 0.20 µm filter)
2x DMEM (with serum) (50 ml)	10 ml 10x DMEM 10 ml FCS (20% in final conc.) 1 ml P/S 29 ml Sterile water to make up to 50 ml
Fibroblast growth medium 3 (FGM3)	500 ml Basal medium 50 ml Fetal calf serum (FCS) (10%) 500 µl FGF (0.001 µg/ml) Insulin human 500 µl (5 µg) P/S 5 ml (100x)

Fibroblast growth medium 3 (FGM3) with no serum	500 ml Basal medium 500 µl FGF (0.001 µg/ml) 500 µl Insulin (human) (5 µg) 5 ml P/S (100x)

3.1.4 Buffers and Solutions

Table 4: Composition of used buffers and solutions

Buffer	Application	Composition
10% SDS-polyacrylamide gel (50 ml)	Immunoblotting	19.8 ml Distilled water 16.7 ml acrylamide rotiphorese gel 30 solution 12.5 ml 1.5 M Tris (pH 8.8) 0.5 ml 10% SDS 0.5 ml 10% APS 0.02 ml TEMED
10x TBS buffer (1000 ml)	Immunoblotting	12.12 g Tris 87.65 g NaCl Distilled water to make up to 1000 ml pH 7.4 (adjusted with HCl)
12% SDS-polyacrylamide gel (50 ml)	Immunoblotting	16.5 ml Distilled water 20 ml Acrylamide rotiphorese gel 30 solution

		12.5 ml 1.5 M Tris (pH 8.8) 0.5 ml 10% SDS 0.5 ml 10% APS 0.02 ml TEMED
15% SDS-polyacrylamide gel (50 ml)	Immunoblotting	11.5 ml Distilled water 25 ml Acrylamide rotiphorese gel 30 solution 12.5 ml 1.5 M Tris (pH 8.8) 0.5 ml 10% SDS 0.5 ml 10% APS 0.02 ml TEMED
1x TBS-T buffer (1000 ml)	Immunoblotting	100 ml 10x TBS 1 ml Tween 20 Distilled water to make up to 1000 ml
4x SDS-PAGE sample loading buffer (20 ml)	Immunoblotting	4.0 ml 1M Tris-HCl (pH 6.8) 1.6 g SDS 8.0 ml 100% glycerol 0.8 ml 14.7 M β-mercaptoethanol 2.0 ml 0.5 M EDTA 16.0 mg Bromophenol blue Distilled water to make up to 20 ml

5x SDS-PAGE electrophoresis buffer (1000 ml)	Immunoblotting	15.1 g Tris 94 g Glycine 5 g SDS Distilled water to make up to 1000 ml pH 8.3 (adjusted with KOH)
6% SDS-polyacrylamide gel (50 ml)	Immunoblotting	26.5 ml Distilled water 10 ml Acrylamide rotiphorese gel 30 solution 12.5 ml 1.5 M Tris (pH 8.8) 0.5 ml 10% SDS 0.5 ml 10% APS 0.04 ml TEMED
APS 10% (10 ml)	Immunoblotting	1 g APS Distilled water to make up to 10 ml
CytoBuster Protein extraction reagent	Immunoblotting	Cat No. 71009-3 (MerckMillipore)
GST-fish buffer (500 ml)	Immunoblotting	25 ml 1 M Tris (pH 7.4) 75 ml 1 M NaCl 2 ml 1 M $MgCl_2$ 50 ml Glycerol 5 ml Igepal CA-630 Distilled water to make up to

		500 ml
Ponceau S stain 0.2% (100 ml)	Immunoblotting	5 ml Acetic acid (Glacial) 0.2 g Ponceau S Distilled water to make up to 100 ml
Roti-free stripping buffer (250 ml)	Immunoblotting	Carl Roth's spec. Cat No. 0083.2
SDS 10% (100 ml)	Immunoblotting	10 g SDS Distilled water to make up to 100 ml
SDS-polyacrylamide stacking gel (10 ml)	Immunoblotting	6.8 ml Distilled water 1.7 ml Acrylamide rotiphorese gel 30 solution 1.25 ml 1.5 M Tris (pH 6.8) 0.1 ml 10% SDS 0.1 ml 10% APS 0.01 ml TEMED
Transfer buffer (1000 ml)	Immunoblotting	3.02 g Tris 14.4 g Glycine 200 ml Methanol Distilled water to make up to 1000 ml
0.2% Triton (50 ml)	Immunofluorescence	100 µl 10x Triton up to 50 ml DPBS

1x Roti-immunoblock (100 ml)	Immunofluorescence	10 ml 10x Roti-immunoblock Distilled water to make up to 100 ml
4% Paraformaldehyde (PFA) (250 ml)	Immunofluorescence	10 g Paraformaldehyde 50 µl 10 N NaOH 25 ml 10x DPBS Distilled water to make up to 250 ml pH 7.0 (adjusted with HCl)
50x TAE buffer (1000 ml)	DNA agarose gel electrophoresis	242.28 g Tris 57.1 ml Acetic acid (Glacial) 200 ml 0.25 M EDTA (pH 8.0 adjusted with NaOH) Distilled water to make up to 1000 ml
DNA agarose gel 2% (50 ml)	DNA agarose gel electrophoresis	1 g agarose powder 50 ml 1x TAE buffer 3 µl Midori green advance DNA stain
0.2 N NaOH (100 ml)	Collagen type I neutralization	800 mg NaOH Sterile water to make up to 100 ml
Accutase Mix	Live human Engineered	97 ml StemPro Accutase cell dissociation reagent

	Connective Tissues (hECT) digestion	1ml 2.5% Trypsin (final conc. 0.025%), 2ml DNaseI stock solution (final conc. 20 µg/ml)
Blocking buffer	FACS analysis	200 ml DPBS (not containing Ca^{2+}/Mg^{2+}) 27 ml FCS (5%) 5 ml BSA (1%) 2.6 ml Triton-X (0.5%)
Collagenase type I	Live hECT digestion	500 mg Collagenase type I 200 ml DPBS (containing Ca^{2+}/Mg^{2+}) 20 ml fetal bovine serum (FCS 20%)

3.1.5 Inhibitors

Table 5: Inhibitor used with final concentrations in 2D and 3D cultures

Name	Stock solution	Solvent used	Working Concentration	Control Condition
BTP2	25 mM	DMSO	100 nM, 1µM, 10 µM	DMSO
Cyclosporin A (CsA)	40 mM	DMSO	20 nM	DMSO
Pyrazol 3 (Pyr3)	10.95 mM	DMSO	100 nM, 1µM, 3 µM	DMSO

Thapsigargin (TGN)	1 mM	DMSO	3 µM	DMSO

3.1.6 Kits

Table 6: Kits

Name	Application	Manufacturer
5x HOT FIREPOL EvaGreen qPCR Mix Plus	RT-qPCR	Solis Biodyne
Annexin-V-FLUOS staining kit	Apoptotic/-necrotic cells staining	Roche
Fluo-5N AM cell permeant Ca^{2+} dye	Live cell Ca^{2+} imaging (Endoplasmic Reticulum)	AAT Bioquest
Lumi-light Western blotting substrate	Chemiluminescence protein blot visualization	Roche
Revert Aid First Strand cDNA Synthesis Kit	RNA reverse transcription to cDNA	Thermo-Scientific
RNeasy kit	Total RNA isolation	Qiagen
Screen Quest Fluo-8 No Wash Ca^{2+} dye	Live cell Ca^{2+} imaging (Cytoplasmic)	AAT Bioquest
Super signal west femto maximum sensitivity substrate	Chemiluminescence protein blot visualization	Thermo-Scientific

3.1.7 Primers

Table 7: Primers used for qPCR and RT-qPCR

Gene Name	Forward Primer (5´→3´)	Reverse Primer (5´→3´)	Annealing temperature
COL1A1	GTTCAGCTTTGTGGACCTCC	TGTACGCAGGTGATTGGTGG	60°C
CTGF	GGTTACCAATGACAACGCCTC	GTACGGATGCACTTTTTGCCC	60.4°C
DDIT3	AAGGCACTGAGCGTATCATGT	TGAAGATACACTTCCTTCTTGAACAC	60°C
GAPDH	TCATTTCCTGGTATGACAACGA	GTCTTACTCCTTGGAGGCC	57°C
HSPA5	TGTTACAATCAAGGTCTATGAAGGTG	CAAAGGTGACTTCAATCTGTGG	60°C
ORAI1	GCTCATGATCAGCACCTGCAT	GGGACTCCTTGACCGAGTTG	61°C
ORAI3	ACGTCTGCCTTGCTCTCGG	GTGGGTACTCGTGGTCACTCT	62°C
STIM1	ACTTGGAGGGGTTACACCGA	ATCTCATCGCGCAGCTTCTT	60°C
STIM2	TGGATGATGACAAAGATGGTGGAA	TCTGTGCAGATGGCTGTGTTTA	60°C

3.1.8 Primary antibodies for immunoblotting

Table 8: Primary antibodies used for immunoblotting

Antibody	Working Dilution	Produced in	Clone/Type	Cat No.	Manufacturer
BiP	1:1000	Rabbit	Monoclonal/C50B12	3177	Cell Signaling
Collagen1a1 propeptide (Pro-Col1a1)	1:1000	Rabbit	Polyclonal	600-401-D19	Rockland
CTGF	1:200	Goat	Polyclonal/H-55	sc-25440	Santa Cruz
PERK	1:1000	Rabbit	Monoclonal/D11A8	5683	Cell Signaling
Phospho-Smad2 (p-Smad2)	1:1000	Rabbit	Monoclonal/(Ser 465/467)	3108	Cell Signaling
Smad2/3	1:1000	Rabbit	Monoclonal/D7G7 XP	8685	Cell Signaling
α-Tubulin	1:2000	Mouse	Monoclonal/B-5-1-2	T5168	Sigma Aldrich

3.1.9 Secondary antibodies

Table 9: Secondary antibodies for immunoblotting conjugated to horseradish peroxide (HRP)

Antibody	Working Dilution	Produced in	Cat No.	Manufactured by
Goat	1:10000	Donkey	Sc-2354	Santa Cruz
Mouse	1:10000	Rabbit	A9044	Sigma Aldrich
Rabbit	1:40000	Goat	A9169	Sigma Aldrich

3.1.10 Devices

Table 10: Devices used

Name of device	Model Name	Company
Autoclave	VX-150	Systec
Automated cell analyzer	Cellavista	SynenTec
Automated cell counter	CASY (TTC)	Roche
Centrifuges	Centrifuge 5804	Eppendorf
	Centrifuge benchtop 5417R	Eppendorf
	Megafuge 40 R	Thermo-Scientific
Chamber for gel electrophoresis	Mini-PROTEAN Tetra	Bio-Rad
Chemiluminiscence-based	Chemidoc MP	Bio-Rad

imaging system		
Fluorescent microscope (inverted) with climate chamber	IX81	Olympus
Gel imaging system	Gel Doc XR Imaging System	Bio-Rad
High speed camera system	MicroNIKKOR	MIKROTRON
Immunoblotting chamber	Mini Trans Blot Cell	Bio-Rad
Incubator for culture maintenance	Labotect Incubator C 200	Labotect
Incubator for culture maintenance	Steri-cult 200 Incubator	Forma Scientific
Incubator with shaker	MAXQ 4450	Thermo-Scientific
Laminar flow hood	HERAGAURD	Thermo-Scientific
Low vacuum suction pump	BioVac	Welch
Manual cell counting chamber	Fuchs-Rosenthal bright-line	Marienfeld-Superior
Microscope camera	CAM-XM10-T-Camera	Olympus
Microscope filter for DAPI	BP 403/12	Olympus
Microscope filter for FITC	BP492/18	Olympus
Microscope filter for GFP	BP 470/20	Olympus
Microscope filter for Texas	BP 572/23	Olympus

Red		
Microscope objective magnification 20x	LUCPLFLN20xPH|0.45	Olympus
Microscope objective magnification 40x	LUCPLFLN40xPH|0.60	Olympus
Multi-mode microplate reader	Flex Station 3	Molecular Devices
pH meter	WTW	Inolab
Pipettes	Pipetman	Gilson
QIAcube (RNA isolation robot)	SN 4958	Qiagen
Real-time PCR System	TaqMan 7900HT Fast Real-Time PCR System	Applied Biosystems
Rheometer	RSA-G2	TA instruments
Scale	Portable	Sartorius
Shaker	Vibramax 100	Heidolph
Shaker (Rotatory)	Reax 3	Heidolph
Shaker (Horizontal)	GFL 3016	GLF
Spectrophotometer	Nanodrop 1000	Peqlab
Stereo microscope	Lumar V 12	Zeiss
Stereo microscope	M80	Leica
Stereo microscope	Primovert	Zeiss

Thermocycler	Mastercycler gradient	Eppendorf
Tissueslyser (Bead mill)	TissueLyser II	Qiagen
Vortexer	VF 2 Vortexer	Janke u. Kunkel IKA Labortechnik

3.1.11 Software

Table 11: Softwares used

Name	Application	Developer
Axiovision 4.8.2	High magnification image acquisition with Lumar V 12	Zeiss
BD FACS Diva V 6.1.3	Flow cytometric analysis for cell-cycle	BD
Flowing Software version 2.5.1	Histogram analysis of cell-cycle	Turku Centre for Biotechnology, Finland
GraphPad Prism 7.0	Statistical analysis of data and graph preparation	GraphPad
Image J 1.6_24, time series analyzer V 3.0 plug-in	Image analysis for fluorescent traces, cross-sectional area (CSA) and volumes measurements	National Institute of Health USA
Image Lab 5.1	Semi-quantification of immunoblots and DNA agarose gels	Bio-Rad
Micro-display	High speed imaging	Silicon software

system V 5.4.1.2		GmbH
SDS 2.4	TaqMan 7900HT Fast Real-Time PCR System operation and its data analysis	Applied Biosystems
Trios V 4.2.1.36612	Destructive tensile strength measurement	T.A. Instruments
Xcellence Pro	Olympus microscopy system operations for cell imaging	Olympus

3.2 Methods

3.2.1 Cell culturing, passaging, and freezing of normal human ventricular cardiac fibroblast (NHCF-V)

Normal human ventricular cardiac fibroblasts (NHCF-V) were purchased from Lonza (Cat. No. CC-2904). The cells were donated by a male Caucasian donor at the age of 52 years and were tested negative by the manufacturer for common transmissible pathogens. The death cause was not cardiac dependent. The frozen stock received from the manufacturer was considered as passage 0 (P0) and cultured in fibroblast basal growth medium-3 (FGM-3, PromoCell). The fibroblast basal medium was supplied with a supplement kit consisting of human basic fibroblasts growth factor (bFGF), human insulin, and fetal calf serum (FCS). FGM-3 was supplemented immediately before use with 0.001 µg/ml bFGF, 5 µg/ml insulin, 10% FCS and 1% penicillin-streptomycin (Gibco) as anti-infective agents.

The cells from P0 were seeded in a density of 5000 cells/cm^2 in tissue culture flasks and incubated at 37°C temperature, 5% CO2, and 99% humidity. The medium was replenished with fresh medium every other day. The NHCF-V

reaching 80-90% confluency were passaged. Therefore, the confluent flasks were made debris free by washing with pre-warmed DPBS (not containing Ca^{2+} and Mg^{2+}). Then, the cells were detached from the surfaces with 1 ml/25 cm^2 of 1x synthetic trypsin (TryPLE Express, Gibco) and incubated for 3 min at 37ºC temperature, 5% CO_2, and 99% humidity. As soon as the cells acquired a round shape and started floating, the enzyme activity was immediately blocked with an equal volume of FGM-3 containing 10% FCS. The cell suspension was collected in a reaction tube and centrifuged at 300xg for 5 min at 4ºC. The dead cells/debris were removed by discarding the supernatant. The cell number and viability were determined by electrical current exclusion using a Casy TTS system (Roche). Finally, the collected cells were splitted as 1:2 ratios for expansion. To prepare frozen stocks, the cells at P2 were trypsinized and re-suspended in FGM-3 supplemented with 20% FCS and 10% DMSO. Then, one million NHCF-V in a volume of 1 ml suspension were pipetted in 1.8 ml cryotubes (NUNC) and stored in a freezing container (Mr.Frosty) at -80ºC overnight. The cells were then transferred to a -150ºC freezer for later use. To thaw the frozen stock, pre-warmed FGM-3 was used (1 ml/9.5 cm^2 of the culture surface in a collection tube). The cryovials with NHCF-V cells were quickly thawed at 37ºC, cells were re-suspended in the cryovials and then added to pre-warmed FGM-3 in the collection tube. Finally, this cell suspension was dispensed to culture flasks and maintained at 37ºC temperature and 5% CO_2. Cells in passage 4 (P4) were used in all experiments.

3.2.2 Live Ca^{2+} imaging

3.2.2.1 Preparation of cells for live-cell Ca^{2+} imaging

To elucidate changes in Ca^{2+} levels in the cytoplasm and endoplasmic reticulum (ER), the NHCF-V were plated in 12-well tissue-culture plates. As starting seeding density, 100,000 cells per well were used. When the confluency reached to 80-90%, the cells were starved overnight in serum-free FGM-3. Then, the treatment was carried out with SOCE inhibitor BTP2 or the TRPC3 inhibitor pyrazole 3 (Pyr3) for 1 h in serum-free conditions.

3.2.2.2 Loading of fluorescent Ca^{2+} dyes and live-cell imaging for Ca^{2+} transient and oscillation measurements

The pretreated cells were incubated for 30 min with the high Ca^{2+} sensitivity, low efficacy dye Fluo-8 for cytoplasmic Ca^{2+} changes. Fluo-8 has fast binding kinetics with a low K_d value of 389 nM, upon binding with Ca^{2+} it shows over a 200-fold increase in brightness of fluorescence. For ER Ca^{2+} changes, the cells were loaded with the high Ca^{2+} efficacy, low sensitivity dye Fluo-5N. The dissociation constant of Fluo-5N is very high with K_d value 90 µM that makes it suitable to detect changes in Ca^{2+} at a very high concentration like ER Ca^{2+} stores. Live-cell Ca^{2+} imaging was performed using an inverted fluorescence microscope (Olympus) in a climate chamber that was pre-warmed for at least 45 min before the start of measurement. The microscope settings for live Ca^{2+} imaging are given in Table 12.

Table 12: Inverted fluorescent microscope (Olympus) settings for live-cell Ca^{2+} imaging

Specification	Setting
Temperature	37ºC

CO_2	5%
Objective(LUCPLFLN20xPH|0.45)	20x
Lamp (MT-ARC/HG 150 W Mercury/Xe) intensity	80%
Exposure time	120 ms (unless otherwise stated)
Filter	GFP (BP 470/20)

The experiment manager in the Xcellence pro was adjusted according to the settings given in Table 13.

Table 13: Settings of Xcellence pro experimental manager for live-cell Ca^{2+} imaging

Specification	Setting
Imaging	Every 5 sec
Repetition	60 times (unless otherwise stated)

First, the fluorescence recordings were made under basal conditions, and then, Ang II or TGF-β in a final concentration of 100 nM and 5 ng/ml, respectively, were applied between the 20^{th} and 25^{th} sec of measurement. The changes in fluorescent intensities representing Ca^{2+} levels were analyzed with the help of time series analyzer V 3.0 plugin of Image J. To this end, cells in each frame were encircled and then the average fluorescent intensity of the region of interest (ROI) was taken. In the same way, fluorescent intensities of cell-free areas were determined as background and subtracted from the average fluorescence of each cell. The background-subtracted changes in fluorescence intensities were plotted in ΔRFU

units versus time. The NHCF-V showing repetitive, spontaneous, cytoplasmic Ca^{2+} changes were marked and counted manually as Ca^{2+}-oscillating cells under different conditions. The numbers of oscillating cells were presented as percentages of the total cells in the frame.

3.2.3 Proliferation and apoptosis analysis

The anti-proliferative potential of BTP2 and Pyr3 was studied by treating NHCF-V with different concentrations of inhibitors over a period of three days. For proliferation assay, NHCF-V were seeded at a low density of 15,000 cells per well onto 24-well plates and cultured with FGM-3 supplemented with 10% FCS. The next day was marked as day 0 where two plates with NHCF-V were fixed with 4% PFA in DPBS for 20 min as base-line control. The reaming cells were treated in triplicates with different concentrations of inhibitors along with control conditions. The medium was changed after every 24 h in all conditions and cells were fixed at days 1, 2, and 3 in the same way as described above. After fixation, the cells were washed once with 1x DPBS and then stained with DAPI ratio 1:1000 in DPBS and stored in dark at 4ºC under shaking. The cell counting was performed with an automated cell counting system, Cellavista (Synentec), and the absolute numbers of cells were determined.

To determine the apoptotic cell fraction, fully confluent NHCF-V were starved in serum-free FGM-3 for 12-14 h and then incubated with BTP2 or Pyr3 for 24 h. The apoptotic cell fraction was determined by live-cell fluorescent staining. To this end, the cells were incubated with annexin V-FITC, propidium iodide (PI), and Hoechst 33342 at 37ºC for 30 min in dark. Annexin V-FITC binds to the outer leaflet of apoptotic cells and PI is permeable to the incompetent plasma membrane and

intercalates with the DNA of necrotic cells. Next, the live-cell fluorescence imaging was performed and five images were taken for each fluorophore from different regions of a well. Annexin V and/or PI-positive cells were counted to determine the apoptotic/-necrotic cells and were given as a fraction of DAPI-positive cells.

3.2.4 Preparation of human engineered connective tissues (hECT)

3.2.4.1 Preparation of the master mix for hECT generation

The hECT were prepared by embedding NHCF-V in the collagen type I matrix. A master mix was prepared of acid-soluble bovine collagen type I neutralized with 0.2 N NaOH, supplemented with 2x DMEM, and finally mixed with NHCF-V suspension. The components of the master mix given in Table 14 were scaled-up to the number of tissues prepared in each batch of casting.

Table 14: Master-mix components for hECT generation

Master mix component	Volume (µl)
Collagen type I (Stock Conc. 6.91 mg/ml) 0.3 mg per hECT	43.4
2x DMEM	43.4
0.2 N NaOH	2
NHCF-V (0.750×10^6)	91.2
Total Volume	180

All the consumables and components of the master mix were pre-chilled and kept on ice during casting. The components were mixed in an orderly manner. First, collagen was pipetted in a reaction tube and then an equal volume of 2x DMEM

with phenol red as an internal indicator was added to that. This mixture turns yellow, indicating acidic pH which was neutralized with 0.2 N NaOH in a drop-wise manner until red color appeared. Finally, NHCF-V suspension was added to the final mixture, the components were swirled gently and immediately proceeded for tissue casting while keeping on ice.

3.2.4.2 hECT casting in flexible-pole tissue casting multi-well plates

The master mix prepared in section 3.2.4.1 was used for hECT casting. Pre-wet, filtered tips were used for loading the master mix in a circular motion into the oval-shaped wells of flexible pole tissues casting plates (TM5MED, TPK-Kunststofftechnik GmbH). After loading the master mix, tissue plates were incubated for 1 h at 37ºC, 5% CO_2, and 99% humidity for self-assembling of collagen matrix with NHCF-V. The hECT got assembled in a ring shape (Fig. 3) and then conditioned medium was added containing suitable concentrations of used inhibitors for 2 h. After that, pro-fibrotic mediators, 100 nM Ang II, 5 ng/ml TGF-β, or a combination of both (AT), were added. The culture medium was changed every other day with the same order of inhibitor and pro-fibrotic factors. Rheometric experiments of hECT were performed at day 3 and day 5 after casting.

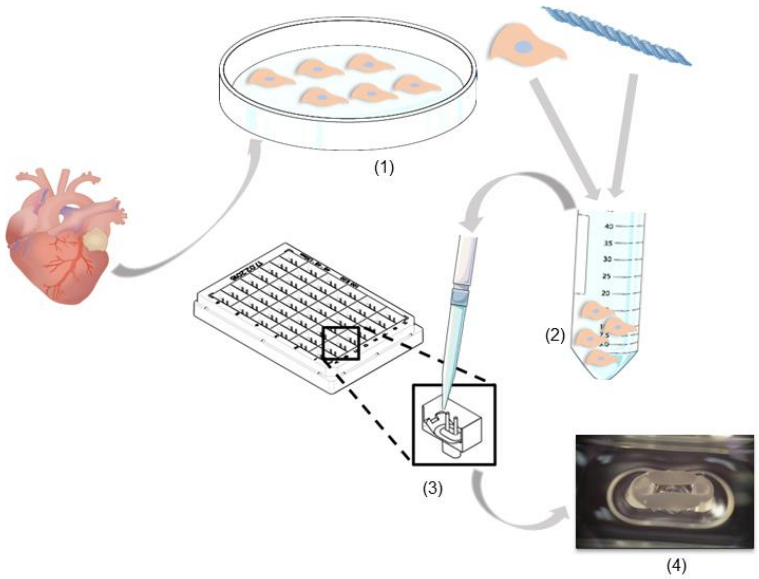

Figure 3: A schematic representation of human engineered connective tissue (hECT) generation.

Human primary cardiac fibroblasts were grown in 2D-culture conditions (1) and then suspended in collagen type I (2). This mixture is then poured into hECT casting molds with two flexible poles to hold the tissues (3). Shown is the original hECT on the poles (4).

3.2.5 Contraction measurement of the hECT

The contraction measurements were started immediately after the addition of conditioned medium to the hECT plates and marked as day 0. The imaging set-up consisted of a high-speed camera (MicroNIKKOR, MIKROTRON) and a UV-exciting adaptor for tissues holding UV-dye poles. The tissue plates were placed on a holder and then UV-dye poles were excited with an adopter under the high-speed camera (Fig. 4). After adjusting the focus, the tissue poles were imaged using Micro-display V 5.4.1.2 (Silicon software GmbH) for contraction analysis. The images were taken after every 24 h in the same manner. The distance between the poles was measured with Image J (V 1.6_24) as a measure of contraction. The

percentage difference in the distance from day 0 was determined for each day and presented as percentage contraction of the hECT. The experimental set-up used for imaging UV-pole is shown in Figure 4.

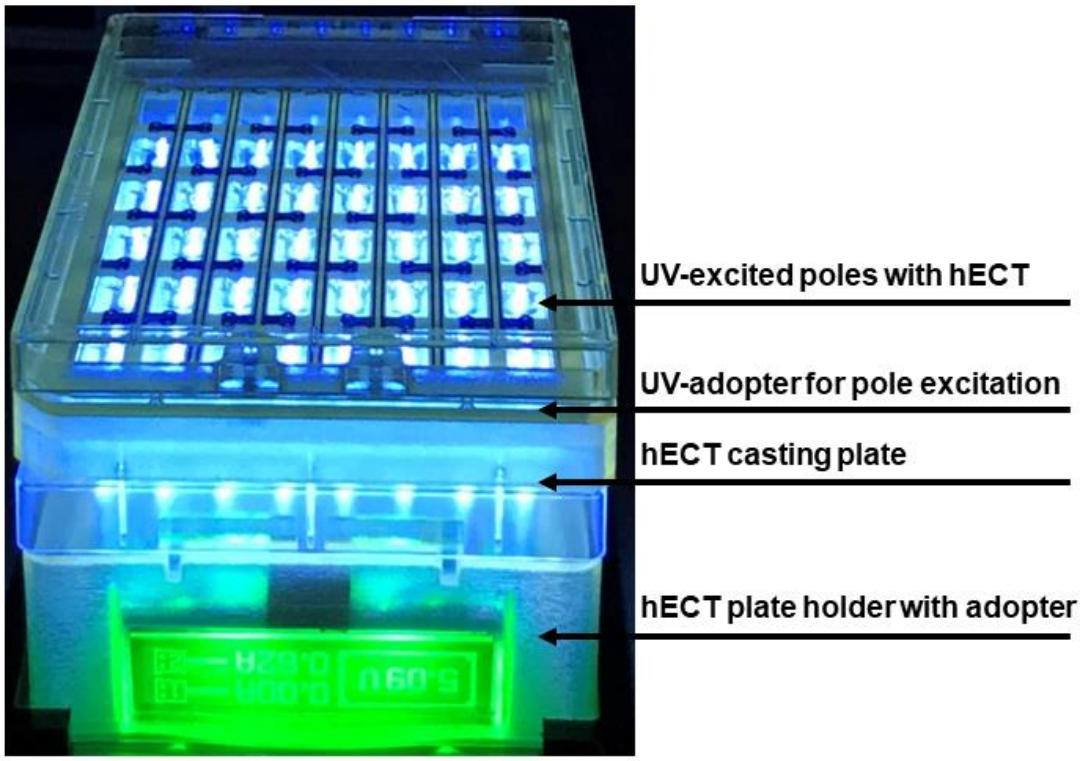

Figure 4: UV-poles imaging system for contraction measurement.

3.2.6 Cross-sectional area and volume measurement of the hECT

The cross-sectional area (CSA) was used as a parameter of hECT compaction and stress-values calculation (*Stress=Force/Area*) for stiffness studies by rheology. The macroscopic images of the hECT were taken from the top and side views with Lumar V 12. These macro images were then analyzed with Image J 1.6_24 for diameter measurement at several positions of both views. Then, the averaged diameters were used to calculate the cross-sectional area (CSA) in mm^2, according to the equation given below.

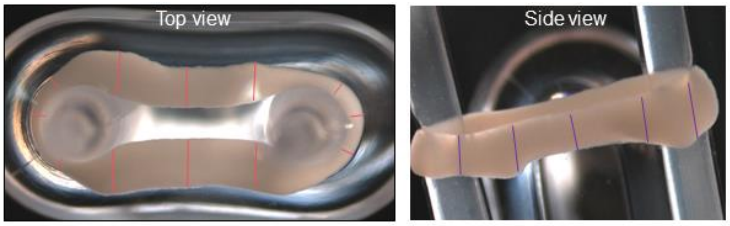

CSA= π ($D_{\text{average tope view}}$/2 x $D_{\text{average side view}}$ /2)

Figure 5: Image of hECT with top and side view markings for diameter.

Next, the volumes of hECT were calculated and used as another parameter of compaction and contraction. The macroscopic images of the hECT were taken as described above and analyzed with Image J 1.6_24 for total length calculation of the tissue. Then the CSA measured above was multiplied with the total length of the hECT to get volumes. The volume calculations were made according to the formula given below.

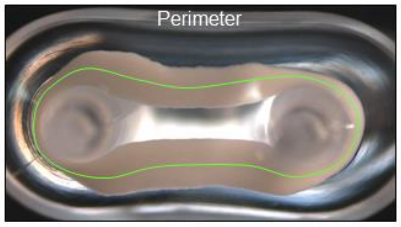

Volume= CSA x Perimeter

Figure 6: Image of hECT with marking of perimeter.

3.2.7 Destructive tensile strength measurement

The viscoelastic properties of hECT were determined by destructive tensile strength measurements in a rheometric analysis. The instrument used for these studies, was the RSA-G2 rheometer (T.A. instruments), as shown in Figure 7.

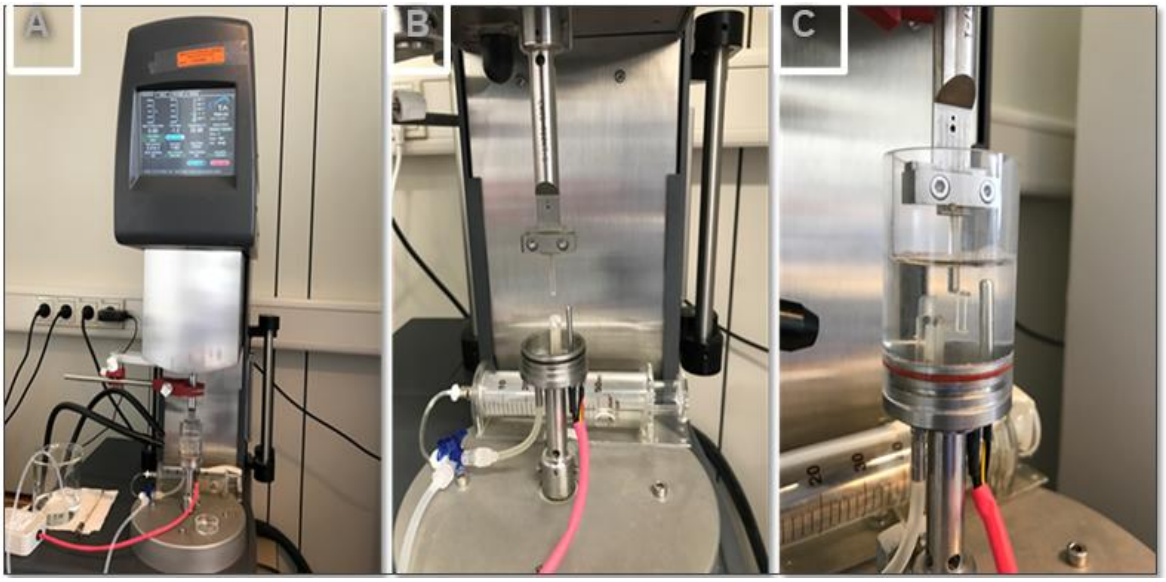

Figure 7: Experimental set-up for destructive tensile strength measurements showing RSA-G2 rheometer.

Shown are different parts of the rheometer and accessories used for rheometric analysis. ***A)*** *RSA-G2 rheometer (T.A. Instruments)* ***B)*** *Two arms of the rheometer attached to hECT holding hooks. The tissues were loaded on the hooks of both arms. The upper arm stretches the tissue and the lower arm hold it.* ***C)*** *The tissues on the hooks were equilibrated with DPBS at 37ºC and the uniaxial force of the upper arm is continued to apply till the tissue ruptured.*

To start a destructive tensile strength measurement, the tissue holding hooks attached to the arms of the rheometer were moved closed to each other and tared as *zero*. Then, the hECT were transferred onto the hooks making sure that the arms of the tissues were not twisted or kinked. After that, the upper arm was skewed to widen the gap between hooks. This gap is adjusted so that no stretch is felt on hECT arms and is termed as a *set gap*. All the measurements in an experiment were performed with the same *set gap*. Then, the housing of organ bath is closed, filled with DPBS, and equilibrated at 37°C. The level of DPBS in organ bath was kept so, that the tissues remained immersed until ruptured. Next,

the rheometer setting was adjusted in tension mode with a constant uniform rate of 0.03 mm/sec of change in length and the maximum gap width limit was kept at 100 mm. As the temperature of the organ bath reached 37°C, the experiment was started where uniaxial force continued to stretch the hECT until it ruptured. At this point, the experiment was stopped and the ruptured hECT was removed from the organ bath to start a new measurement in the same manner. The rheometric data of passive force were exported as an excel sheet and analyzed for stress calculation as described above and the strain values were calculated by the following formula.

$$Strain = L_{total} - L_0 / L_0$$

Where L_{total} is the total length of gap between the hooks when tissue got ruptured and L_0 is the initial gap between the hooks when tissue was started to stretch. A representative stress-strain curve with important regions of tissue fibrils arrangements is shown in Figure 8.

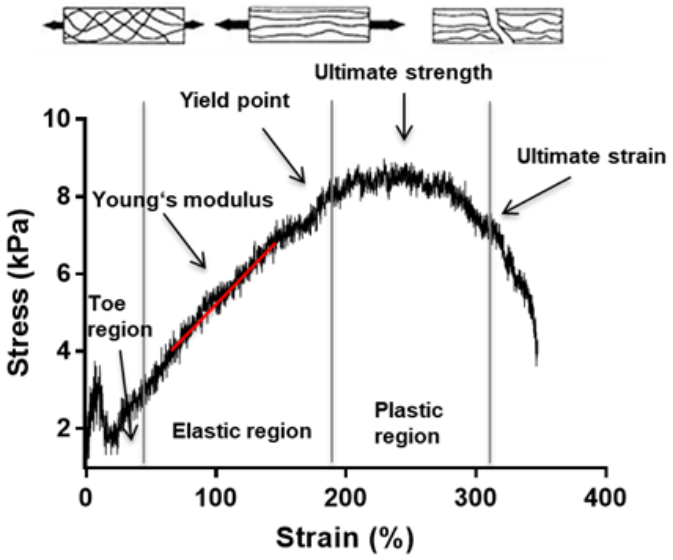

Figure 8: A representative stress-strain curve with regions of hECT fibril re-arrangements

3.2.8 Regions of tissue fibril re-arrangements in a stress-strain curve

3.2.8.1 Toe region

This is the first region of molecular re-arrangements in a stress-strain curve. In the toe region, hECT fibrils align themselves along the direction of applied force. The relationship between stress and strain is non-linear in this region and the straightening of fibrils gives a shallow slope to the curve in this region, as shown in Figure 8.

3.2.8.2 Elastic region

Next to the toe region is the elastic region. In this region, the aligned tissue fibrils stretched along the direction of applied force and the relationship between stress and strain remains nearly linear and thus following Hook's law. The slop of this linear line represents Young's modulus which is a measure of tissue stiffness. This region describes the material's resistance to elastic deformation by applied force and the deformation changes are still reversible in this region.

3.2.8.3 Yield point stress and strain

In a stress-strain curve, yield point stress is the maximum stress value that a material can withstand before a permanent deformation happens and the strain corresponding to this region is the yield point strain. The maximum stress in this region is also referred as the proportional limit of the tissue and any further increase in stress from this point leads the tissues to the plastic region. The values of yield point stress and strain were determined manually to assess the biomechanical properties of hECT in terms of elasticity. The energy absorbed for elastic deformation is known as *resilience* which was determined by calculating area under the stress-strain curve until the yield point in a stress-strain curve.

3.2.8.4 Plastic region

When the stress is continued to apply beyond the yield point, tissues entered into a permanent deformation region, the plastic region. In this region, fibrils undergo microfractures and cannot be reversed to the original shape, even if the applied stress is removed. In the plastic region, two important parameters of hECT stiffness were determined manually. These include the ultimate strength which is the maximum stress withstanding ability, and the ultimate strain which referred to the failure point strain of hECT in the stress-strain curve. Finally, the hECT *toughness,* which is the energy absorbed by a tissue until it gets ruptured, was determined by the total area under the curve of a stress-strain curve.

3.2.9 Re-isolation of viable NHCF-V from hECT

The viable NHCF-V were re-isolated from hECT by enzymatic digestion of the tissue with collagenase type I and Accutase mix solutions. To this end, a single hECT was incubated with 500 µl of collagenase type I solution (composition given

in Material section 3.1.4) in a 24-well plate at 37°C, 5% CO_2 for 2 h. After collagenase digestion, the supernatant was collected and kept on ice in a collection tube. The residual tissue was washed with DPBS and the washing solution was transferred to the above collection tube. Next, 500 µl of Accutase mix solution (composition given in Material section 3.1.4) were added to the washed hECT and incubated at 37°C, 5% CO_2 for 30 min. After Accutase digestion, the hECT was gently pipetted 3-4 times for complete isolation of NHCF-V from the matrix and transferred to the same collection tube. A final washing of the well was done with DPBS containing 5% FCS and pooled together with the above collections. Next, the final pooled cell suspension was centrifuged at 300xg for 5 min at 4ºC, supernatant debris was removed and the cell pellet was re-suspended in DPBS with 5% FCS. Finally, the viable cell numbers were determined by the electrical current exclusion method using the Casy TTS system.

3.2.10 Biochemical analysis of proteins by immunoblotting

3.2.10.1 Protein isolation from NHCF-V

The NHCF-V were cultured in 6- or 12-well cell-culture plates. When the cell reached 70-80% confluency, serum-free FGM-3 was added for 12-14 h to starve the cells. Subsequently, the cells were incubated with the inhibitors for 2 h, and then 100 nM Ang II, 5 ng/ml TGF-β or both (AT) were added for 24 h. After that, the conditioned medium was collected and the cells were washed once with DPBS. Cell lysis was performed with CytoBuster protein extraction buffer (MerckMillipore) containing freshly prepared protease and phosphatase inhibitors. To achieve complete cell lysis and collection, cell scrapers were used. The cell lysates were

collected and centrifuged at 13000xg for 5 min at 4°C to obtain debris-free protein supernatants.

3.2.10.2 Protein isolation from hECT

The hECT were either used directly at the end of the treatment period or snap-frozen in liquid N_2 and stored at -80°C for further use. The hECT were pooled in a group of three in 2 ml collection tubes containing a pre-cleaned steel bead. For cleaning, the beads were incubated in 2 M NaOH for 30 min and then rinsed with Milli-Q water several times. Then, 225 µl of CytoBuster protein isolation buffer (Merk Millipore) containing protease and phosphatase inhibitors were added to each tube. The tubes were placed in ice-cold sample holders of the bead mill (Tissue Lyser II, Qiagen) and run at a frequency of 30 Hz for 90 sec. At the end of the cycle, the samples were placed on ice and checked for lysis. In the case of incomplete lysis, the lysis cycles were repeated with cycles of cooling on ice until complete homogenization of the hECT was achieved. After that, the steel beads were removed carefully and the tissues homogenate were centrifuged at 12000xg for 30 min at 4ºC. Finally, the supernatant was collected and a portion was used for sample preparation, as described below.

3.2.10.3 Protein quantification and sample preparation

The protein concentration was determined by a classical colorimetric assay adopted from the Bradford assay using 1x Roti-Nanoquant (Carl Roth) in a Flexstation 3 system (Molecular Devices). Absolute protein quantification was determined by serial dilutions of bovine serum albumin (BSA) as standard. The protein samples were diluted to 1:20 ratio in ddH_2O, 50 µl of the diluted samples were pipetted in triplicates in 96-well microtiter plates. Then, 200 µl of 1x Roti-

Nanoquant reagent was added onto the protein samples. This reaction mixture was allowed to incubate for 5 min in the dark at room temperature and then absorbance of the colored protein-dye complex was determined at 595 nm with Flexstation 3. The absorbance of ddH_2O was used as a background to calculate the actual absorbance of protein standards. Then, the protein concentrations of samples were calculated from the slope of the absorbance curve. Next, the sample volumes were adjusted with CytoBuster protein extraction buffer for equal protein concentration in all samples. The protein samples from cells, hECT, or medium were mixed in an 1:4 ratio with 4x sample loading buffer containing freshly added 4% β-mercaptoethanol as a reducing agent. After that, the samples were heated in a heating block at 95°C for 5 min and then cooled on ice. Finally, the samples were briefly centrifuged and directly used for immunoblotting or stored at -20°C for later use.

3.2.10.4 Protein segregation by sodium dodecyl sulfate-polyacrylamide gel electrophoresis (SDS-PAGE) and nitrocellulose membrane absorption

a) SDS-polyacrylamide gel preparation

As a first step for protein segregation, SDS-polyacrylamide gels were prepared according to the composition given in Material section 3.1.4. The required volumes of the components for SDS-polyacrylamide resolving gels were pipetted without catalyst. Then the glass plates with spacer (Mini-PROTEAN short plates, Bio-RAD) were assembled and mounted on casting stands. Next, the catalyst TEMED in combination with APS were added to already pipetted gel mixture, briefly vortex, and immediately poured between the glass plate and spacer in a bubble-free manner leaving 1.5 cm space on top for stacking gel. Then, isopropanol was added

on top of the resolving gel mixture and allowed to polymerize for 30 min. Next, isopropanol was discarded and a mixture for staking gel was added on top of the resolving gel. Finally, an appropriate comb was inserted in the stacking gel for protein loading pockets and allowed to polymerize overnight at 4ºC in wet conditions.

b) Protein segregation, transfer, and visualization

The denatured protein samples prepared in section 3.2.10.3 were loaded in pockets of 6 to 12% SDS-polyacrylamide gels. The electrophoresis was performed at 80 V until the bromophenol blue in the samples reached the resolving gel. Then, the voltage was increased to 120 V for 6% gels and 160 volts for 12% gels. The electrophoresis was carried out until the dye front reached the end of the gels. In the next step, gels were removed and the proteins were transferred onto a nitrocellulose membrane sandwiched between gel and filter paper. The transfer was carried out at 100 V for 1 h in ice-cold transfer buffer and the temperature was maintained with ice packing of the transfer chamber. At the end of the transfer, membranes were removed from the sandwich and the transfer was verified by the brief incubation in 0.2% Ponceau S solution. The Ponceau S-stained membranes were documented by imaging. Where necessary, the membranes were cut according to the molecular weight of the proteins of interest to allow the detection of several proteins on one membrane. For the complete removal of the Ponceau S dye, several washings were performed with 1x TBS-T. Then the membranes were blocked with 1x Roti-Block (Carl Roth) for 1 h at room temperature to saturate unspecific binding sites. After that, the membranes were incubated with appropriate primary antibodies dilution in 1x TBS-T (as mentioned in section 3.1.8)

at 4°C overnight while shaking. The next day, the membranes were washed three times with 1x TBST, 10 min each, and then incubated with the respective HRP-conjugated secondary antibodies in appropriate dilutions (as mentioned in section 3.1.9) for 1 h while shaking. After that, the membranes were washed with 1x TBS-T three times, 10 min each, and finally the protein-antibody complexes were visualized with an enhanced chemiluminescence substrate Super Signal West Femto (Thermo-Scientific) using Chemidoc Chemiluminescent imaging system (Bio-Rad).

3.2.11 Molecular biological methods

3.2.11.1 Total RNA isolation from NHCF-V and hECT

For total RNA isolation from NHCF-V 2D cultures and hECT, the RNeasy Mini Kit (Qiagen) was used. The cells or hECT were washed with DPBS and then lysis was performed with RLT buffer with freshly added 1% β-mercaptoethanol. For complete lysis, the samples were carefully mixed by repetitive pipetting steps and then centrifuged for 3 min at maximum speed to collect the supernatant. Next, the RNA isolation from the supernatant was carried out as instructed by the manufacturer at room temperature. Finally, RNA was eluted from the column membrane with 20-30 µl of RNase-free water and stored on ice. The concentration and purity of RNA were determined by the spectrophotometric method using the Nanodrop ND-1000 system (Peqlab). RNA samples having 260/280 values ≈ 2.0 were directly used for cDNA synthesis or stored at -80°C for further use.

3.2.11.2 cDNA synthesis

Total RNA isolated in section 3.2.11.1 was used for reverse transcription to the complementary DNA (cDNA) with the help of the RevertAid First Strand cDNA

Synthesis kit (Thermo-Scientific), according to manufacturer instructions. All the pipetting and handling were carried out on the ice. The composition of the cDNA master mix and the reverse transcription protocol are listed in Table 15.

Table 15: cDNA synthesis reaction mixture and protocol

Reaction Component	Volume/amount used
RNA template	500-1000 ng
Oligod$T_{(18)}$ primer	1 µl
Incubation at 65°C for 5 min	
5x Reaction buffer	4 µl
RiboLock RNase inhibitor (20 U/µl)	1 µl
10 mM dNTP mix	2 µl
RevertAid M-MuLV RT (200 U/µl)	1 µl
Incubation at 42°C for 60 min and termination of reaction at 70°C for 5 min	

3.2.11.3 Quantitative real-time polymerase chain reaction (RT-qPCR)

Changes at the mRNA level of genes were quantified by a real-time polymerase chain reaction (RT-qPCR). The PCR reactions were carried with a 5x HOT FIREPol-EvaGreen qPCR Mix Plus kit, as instructed by the manufacturer. The cDNA was diluted in an 1:10 ratio with nuclease-free water, and 10 µM stock concentration of the primer was used. The reaction mixture used for a PCR reaction is given in Table 16 which was scaled up to triplicates for each reaction.

Table 16: Components of the reaction mixture for RT-qPCR

Reaction component	Volume (µl)
Forward primer (10 µM stock)	0.5
Reverse primer (10 µM stock)	0.5
cDNA	0.5
5x HOT FIREPol EvaGreen qPCR Mix Plus	2
Water (nuclease-free, not DEPC-treated)	6.5
Total	10

The reactions were carried out in MicroAmp optical reaction 384-well plates (Applied Biosystens). To this end, 0.5 µl of diluted cDNA was pipetted first, then, 9.5 µl of the reaction mixture were added to the well. All the steps for PCR reactions were carried out on the ice. Then, the plates were sealed with MicroAmp optical adhesive film (Applied Biosystens) and the reaction mixture was collected at the bottom after centrifugation at 500xg, 4ºC for 3 min. Finally, the reactions were carried out in a TaqMan 7900HT Fast Real-Time PCR-System. The PCR program is given in Table 17.

Table 17: PCR program used for RT-qPCR

Stage	Cycle	Temperature	Time	Repetition	Ramp rate
I	Initial denaturation	95°C	15 min	1 time	1.6°C
II	Denaturation	95°C	15 sec	40 times	

	Annealing	60°C	20 sec		
	Elongation	72°C	40 sec		
III	Dissociation curve	95°C	15 sec	1 time	
		60°C	15 sec		
		95°C	15 sec		

3.2.12 FACS analysis

The status of the cell cycle in a particular cohort of cells can be assessed by fluorescence-activated cell sorting (FACS) of DNA contents. The hECT were dissociated as described in section 3.2.9 and the NHCF-V were fixed with ice-cold 70% ethanol for at least 30 min on ice. The fixed cells can either be used directly or stored at 4°C for further use. After fixation, the cells were washed with DPBS and then incubated for 30 min in 300 µl of 10 µg/ml Hoechst 33342 stain in a blocking buffer (PBS containing 5% FBS, 1% BSA, 0.5% Triton X-100). The staining procedure was performed in the dark on ice. Then, the cells were centrifuged at 300xg for 5 min. The supernatant was discarded and the cell pellet was re-suspended in 500 µl of DPBS. The resuspended, stained cells were strained through a 0.70 µm strainer into round bottom 5 ml glass tubes for FACS (BD Falcon). Then, the flow cytometry was performed to determine the percentages of cells in different phases of the cell-cycle using a laser beam of 404 nm. The cell debris exclusion was carried out by forward scatter (FSC) and side scatters (SSC) scaling. The voltage of fluorescent pulses was adjusted to have clearer segregation of each phase. Then, the dots plot analysis of fluorescent pulses area

(FL2-A) vs. fluorescent pulses width (FL2-W) was performed for each phase. Finally, the histogram plots of FL2-A with gating on each phase were used to determine the cells in G_o/G1, S and G2/M phase of cell cycle using Flow software version 2.5.1.

3.2.13 Statistical analysis

The data sets obtained were compiled in Graph Pad prism and are given as means±SEM. To compare the difference between two groups, an unpaired t-test was applied. For the comparison between more than two groups, an analysis of variance (one-way or two-way ANOVA) test was performed with Dunnett's post hoc or Tukey's multiple comparison tests. The values were considered statistically significant for p-values less than 0.05.

4. Results

4.1 Influence of SOCE inhibition on Ca^{2+} handling and fibrotic markers expression in 2D cultures of NHCF-V

4.1.1 The phenomenon of Ca^{2+} oscillation and transient in NHCF-V

4.1.1.1 Basal characterization of Ca^{2+} oscillations and Ang II-induced Ca^{2+} transients in NHCF-V

In 2010 Chen and colleagues demonstrated that cultured NHCF-V display spontaneous intracellular Ca^{2+} fluctuation in the absence of any trigger [104]. As one aim of this thesis was to characterize mechanisms underlying Ca^{2+} oscillations, their occurrence under the used culture conditions was verified first. The NHCF-V were loaded with the Ca^{2+}-sensitive dye Fluo-8 and time-lapse live Ca^{2+} imaging was performed. The NHCF-V showed irregular fluctuation in the cytosolic Fluo-8 fluorescence in the absence of any stimulus (Fig. 9A, 9B). Of further interest was the regulation of Ca^{2+} transients in these cells elicited by pro-fibrotic factors. Therefore, 100 nM of Ang II were applied between the 20^{th} and 25^{th} second of the recording. Soon after the application of Ang II, the cytosolic Ca^{2+} sharply increased before returning back to baseline level (Fig. 9C, 9D).

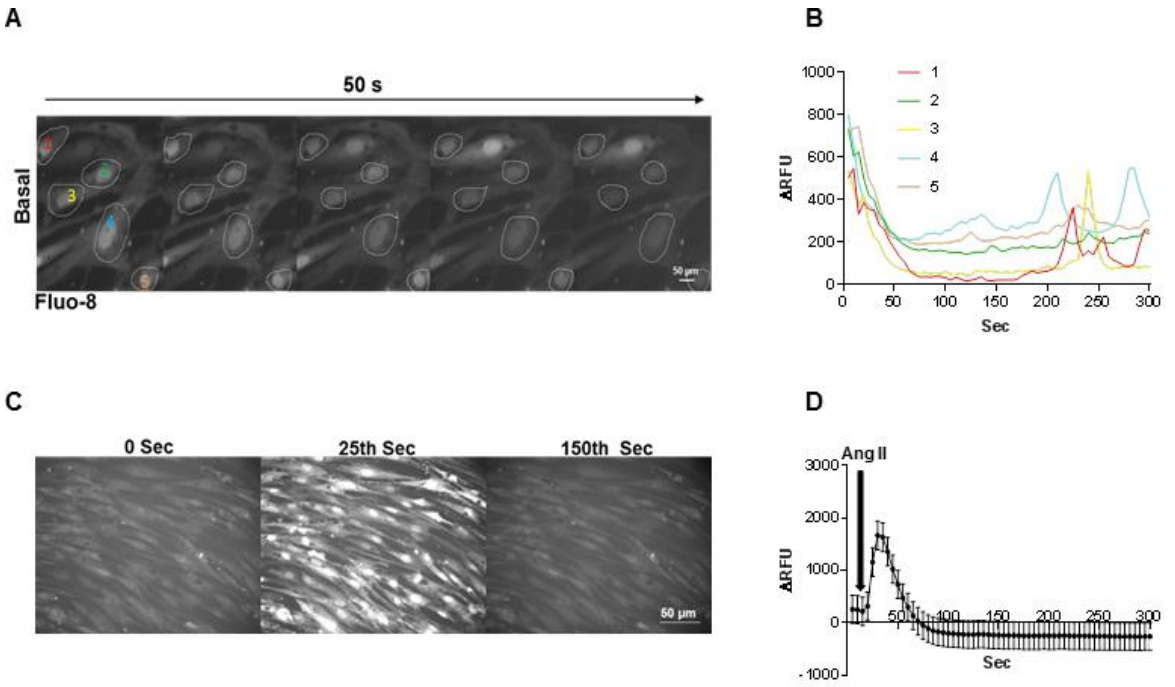

Figure 9: Basal characterization of Ca^{2+} handling in NHCF-V.

A, B) *Representative fluorescence images of Fluo-8-loaded NHCF-V over a time period of 50 s and resultant fluorescence traces of encircled cells are given.* ***C)*** *Representative fluorescence images of Fluo-8-loaded NHCF-V from the beginning, 25^{th} and 150^{th} second following 100 nM Ang II application are shown.* ***D)*** *Ca^{2+} transient measurements in relative fluorescent units (ΔRFU) following 100 nM Ang II application, as indicated. The presented values are means±SEM of four independent experiments with 230 cells in total.*

4.1.1.2 Store-operated Ca^{2+} entry (SOCE) inhibition reduces basal and Ang II-induced Ca^{2+} oscillations and Ang II-induced Ca^{2+} transients in NHCF-V

Next, the effects of store-operated Ca^{2+} entry (SOCE) inhibitor BTP2 on the basal and Ang II-induced Ca^{2+} oscillation were investigated. The NHCF-V were pre-treated with BTP2 for 1 h and then live Ca^{2+} imaging was performed for 5 min. The Ca^{2+}-oscillating cells showing cyclic cytoplasmic Ca^{2+} changes were counted manually. In the absence of inhibitor, approximately 75% cells showed spontaneous Ca^{2+} oscillations, which was reduced to 45% with 1 µM and 10 µM BTP2 (Fig. 10A). Then, the effect of Ang II on Ca^{2+} oscillation was investigated in

the absence or presence of the SOCE inhibitor BTP2. Ang II treatment resulted in a non-significant 15% increase in the percentage of Ca^{2+}-oscillating cells compared to non-treated control. However, after pre-treatment with 10 µM BTP2, exposure to 100 nM Ang II resulted in a 37% decrease in Ca^{2+} oscillations compared to untreated stimulated cells (Fig. 10B). This shows that the SOCE inhibitor BTP2 reduces the percentage of Ca^{2+}-oscillating cells under basal conditions and in the presence of Ang II.

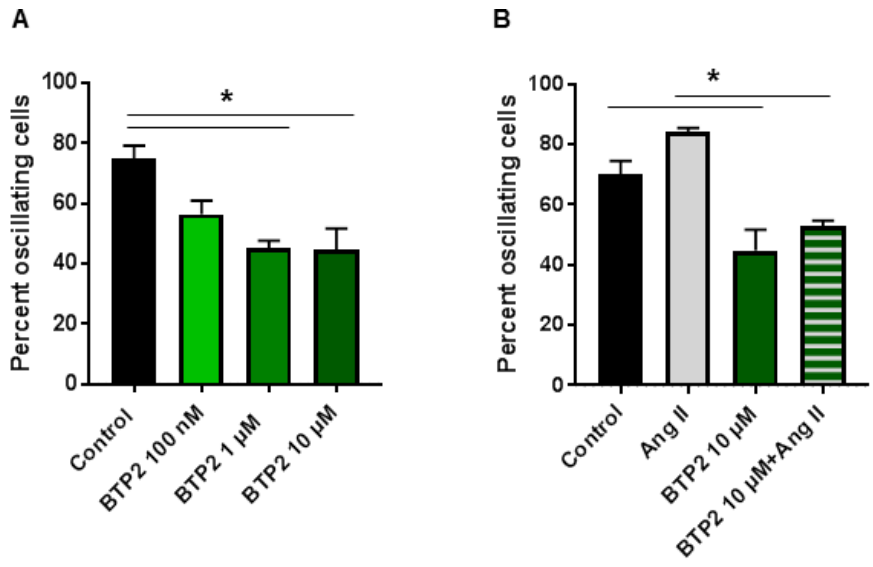

Figure 10: Ca^{2+} oscillation involves SOCE mechanisms in NHCF-V.

*NHCF-V were pre-incubated with the indicated concentrations of BTP2 for 1 h and then loaded with the cytosolic Ca^{2+}-sensitive dye Fluo-8. The percentages of Ca^{2+}-oscillating cells were assessed by live-cell imaging in the absence (A) and presence (B) of 100 nM Ang II. The presented values are means+SEM of 3-6 independent experiments with at least 90-250 cells per group analyzed, *p<0.05 as assessed by one-way ANOVA with Tukey's multiple comparisons.*

To test if the calcium influx via ORAI channels impacts the Ca^{2+} transient in NHCF-V, the cells were pre-treated with BTP2 or left untreated and then used for Ca^{2+} imaging. To induce a Ca^{2+} transient, 100 nM of Ang II were added (Fig. 11). As

shown in Figure 11, the pre-treatment of the NHCF-V with 10 µM of BTP2 resulted in a significant reduction of the Ca^{2+} transient soon after the application of 100 nM Ang II and lower concentrations showed a difference only at the 25th sec of measurement. Furthermore, a significant decline in the resting Ca^{2+} signal was noted after the transient in the presence of the highest inhibitor concentration.

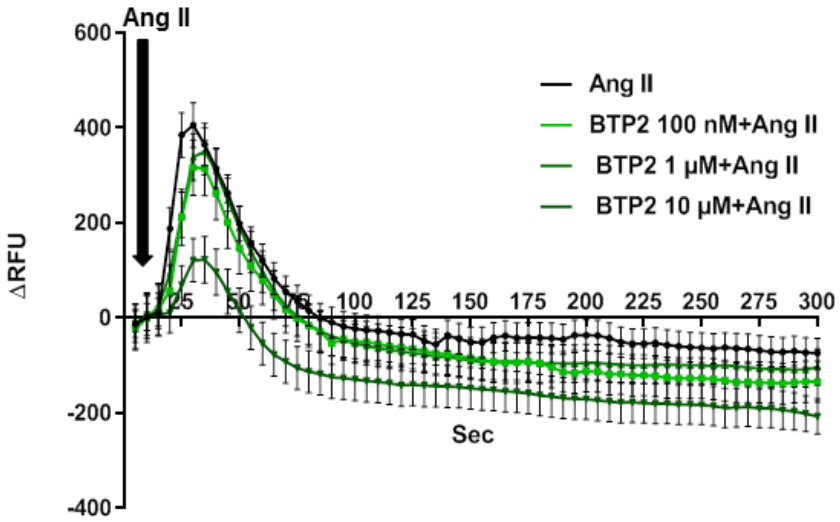

Figure 11: The Ang II-induced Ca^{2+} transient involves SOCE mechanisms in NHCF-V.

The NHCF-V were pre-incubated with 100 nM, 1 µM or 10 µM BTP2 for 1 h and then loaded with Fluo-8. The Ca^{2+} transients were elicited by the application of 100 nM Ang II. Changes in intracellular Ca^{2+} were recorded by live-cell imaging. The presented values are background-subtracted changes in the fluorescence traces given as means±SEM of 3-6 independent experiments (with at least 90-250 cells in total per condition). The p-values are <0.05 from 20th sec for 10 µM vs. Control as assessed by two-way ANOVA with Tukey's multiple comparisons.

4.1.1.3 Effect of SOCE inhibition on TGF-β induced Ca^{2+} transient in NHCF-V

Next, the potential of TGF-β to elicit a Ca^{2+} transient was studied in the absence or presence of SOCE inhibition. The NHCF-V were pre-treated with BTP2 or left untreated as a control. Five ng/ml of TGF-β were added during the course of

measurement in the same manner as described for Ang II before. In the absence of BTP2, TGF-β induced a Ca^{2+} transient with similar amplitude as Ang II, however, there was a more rapid onset of the Ca^{2+} transient in response to Ang II compared to TGF-β. Moreover, TGF-β treatment appeared to result in an extended duration of the Ca^{2+} transient and a slower decay. The highest concentration of 10 µM BTP2 showed a nearly 50% reduction in amplitude of the Ca^{2+} transient, whereas lower concentrations were without effect. The resting Ca^{2+} signal at the tail of the Ca^{2+} transient showed a concentration-dependent decline with a significant reduction when the cells were pre-treated with 10 µM BTP2 (Fig. 12).

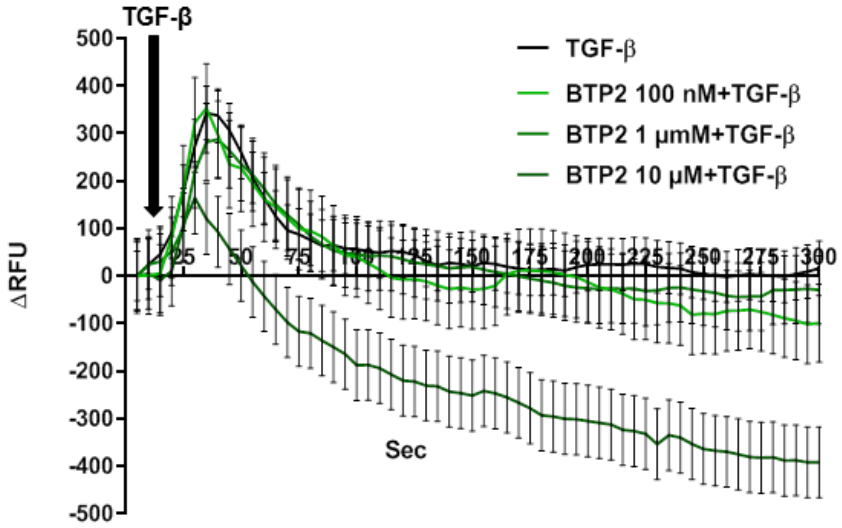

Figure 12: TGF-β-induced Ca^{2+} transient is reduced by SOCE inhibition in NHCF-V.

The NHCF-V were pre-treated with 100 nM, 1 µM, or 10 µM BTP2 for 1 h and then loaded with Fluo-8. A final concentration of 5 ng/ml of TGF-β was applied during measurement as indicated to evoke Ca^{2+} transient. Changes in intracellular Ca^{2+} were recorded by live-cell imaging. The presented values are background-subtracted changes in the fluorescence traces given as means±SEM of three independent experiments with at least 170-350 cells in total per condition, p-values

are <0.05 from 35th sec for 10 µM BTP2 vs. Control as assessed by two-way ANOVA with Tukey's multiple comparisons.

4.1.1.4 SOCE inhibitor BTP2 depleted ER Ca^{2+} in NHCF-V

Finally, the influence of SOCE inhibition on basal cytosolic and ER Ca^{2+} loads was determined by live Ca^{2+} imaging. To this end, the NHCF-V were pre-treated with BTP2 and then loaded with the above-mentioned dyes Fluo-8 for cytosolic Ca^{2+} and Fluo-5N for ER Ca^{2+} levels. The fluorescent intensities representing Ca^{2+} levels showed a significant increase in basal cytosolic Ca^{2+} load with BTP2 (Fig. 13A) and an opposite effect was noted in ER Ca^{2+} load (Fig. 13B).

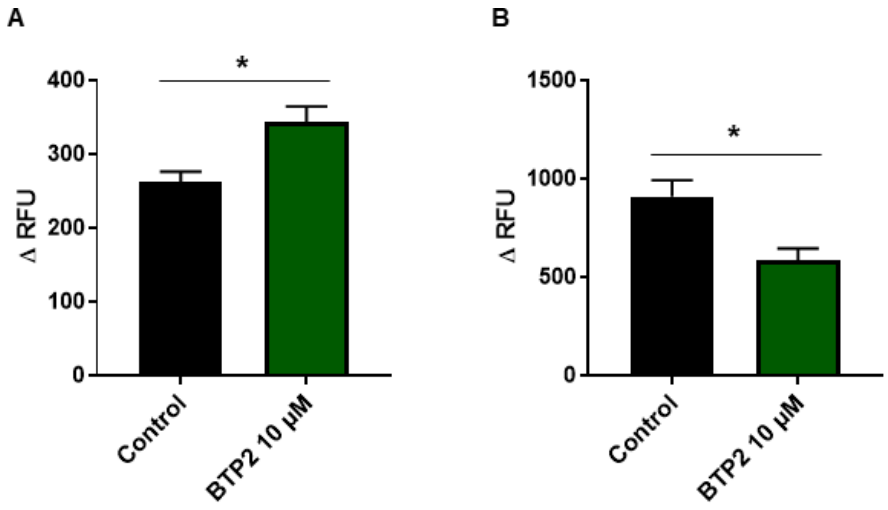

Figure 13: SOCE inhibition oppositely regulates cytosolic and ER Ca^{2+} in NHCF-V.

*NHCF-V were pre-incubated with 10 µM BTP2 for 1 h or left untreated as control and then loaded with either cytosolic Ca^{2+} dye Fluo-8 or ER Ca^{2+} dye Fluo-5N. The background-subtracted changes in fluorescent intensities representing basal cytosolic Ca^{2+} (A) or ER Ca^{2+} (B) were determined by live-cell imaging. The presented values are means+SEM of two independent experiments with at least 250-300 cells per group analyzed, *p<0.05 as assessed by one-way ANOVA with Tukey's multiple comparisons.*

4.1.2 Transcriptional influence of BTP2 on components of the SOCE machinery

To investigate how the SOCE-channel inhibitor BTP2 regulates the SOCE machinery on the transcriptional level in 2D cultures of NHCF-V, the cells were serum-starved and then treated with different concentrations of the inhibitor for 24 h in the absence or presence of fibrotic mediators, including Ang II, TGF-β and a combination of both (AT). The regulation of STIM and ORAI at the transcriptional level was determined by RT-qPCR. The Ca^{2+}-sensitive ER component STIM1 did not show any change in the presence of the fibrotic mediators, but a decline by trend in response to 10 µM BTP2 in the absence of an additional treatment and in the presence of Ang II (Fig. 14A). In contrast, STIM2 showed a significant increase in the presence of 10 µM BTP2 and TGF-β and by trend when BTP2 and Ang II were applied. The fibrotic mediators themselves were without effect (Fig. 14B). The Ca^{2+}-selective pore channel-forming unit ORAI1 showed an increase by trend with 10 µM BTP2 and Ang II, otherwise no effect of fibrotic mediators or BTP2 was observed (Fig. 14C). And finally, ORAI3 was increased by TGF-β and decreased in the presence of 10 µM BTP2. The observed inhibition was strongest in the TGF-β-treatment group (Fig. 14D). The third ORAI isoform, ORAI2, was not detectable by the PCR conditions used.

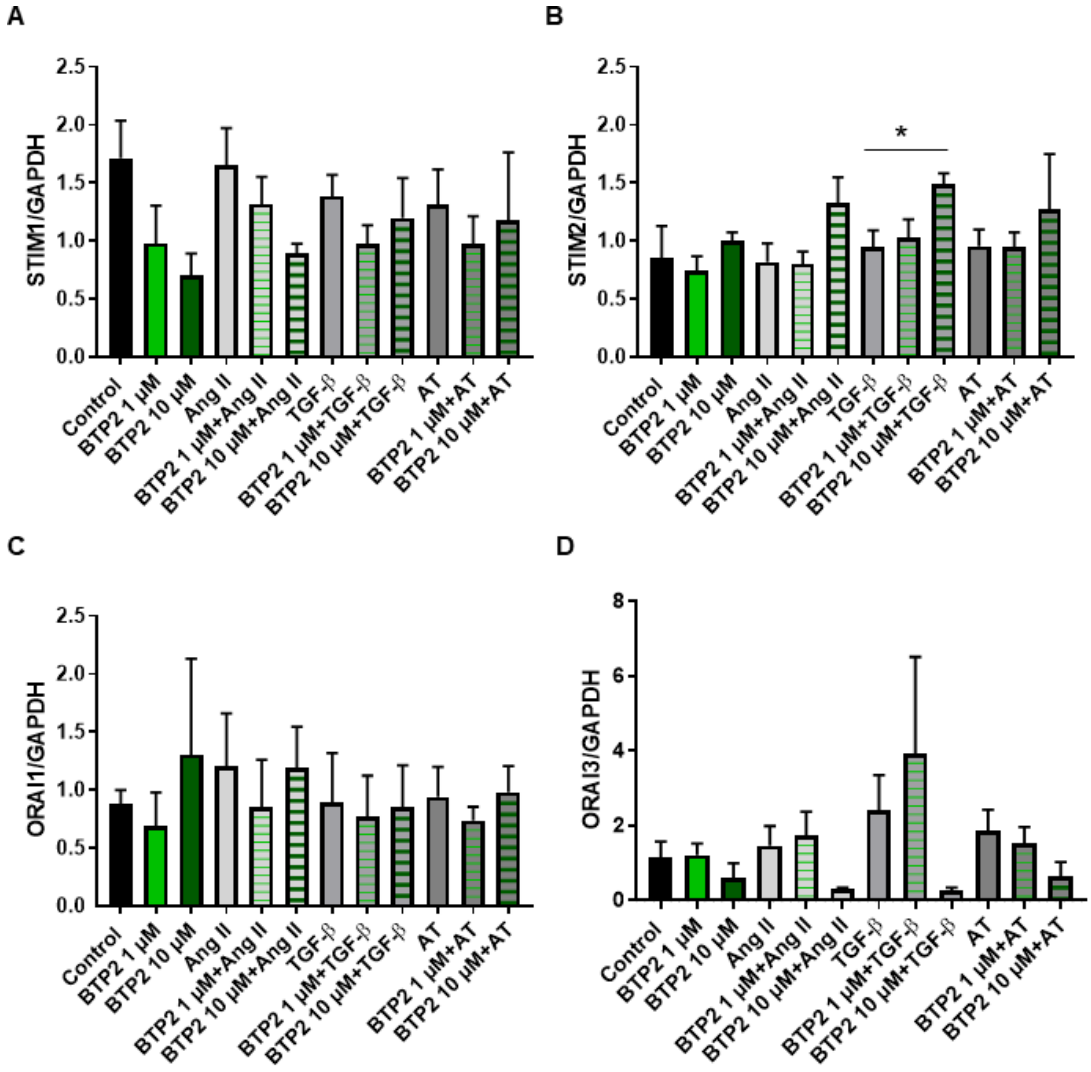

Figure 14: Components of SOCE machinery are by trend regulated by BTP2.

*The NHCF-V were serum-starved for 12 h and then treated with SOCE inhibitor BTP2 (1 µM or 10 µM) in serum-free FGM-3 medium for 2 h, after that 100 nM Ang II, 5 ng/ml TGF-β or a combination of both (AT) were applied for 24 h. Then, RNA was isolated and the changes in the transcription of SOCE genes, including STIM1 (A), STIM2 (B), ORAI1 (C), ORAI3 (D), were assessed by RT-qPCR. The values are normalized with GAPDH as a housekeeping gene. Given are means+SEM of three independent experiments performed with three technical replicate each, *p-value is <0.05 as assessed by one-way ANOVA with Tukey's multiple comparisons.*

4.1.3 Anti-proliferative and apoptotic potential of SOCE inhibitor BTP2

A characteristic of cardiac myofibroblasts is their ability to proliferate [198]. Therefore, the effect of BTP2 was studied on the serum-dependent mitogenic behavior of NHCF-V. The cell number was assessed over a period of 3 days in the presence of two different concentrations of BTP2. Compared to untreated cells, BTP2 treatment had no effect when 1 µM was used, however, when 10 µM BTP2 was added even after 2 days a substantial lower number of cells were detected compared to control (Fig. 15A). To evaluate the effect of BTP2 on cell viability, the influence on cell death, by either apoptosis or necrosis, was studied by a combined annexin V/propidium iodide (PI) staining. To this end, the cells were seeded and let grow to almost full confluency to avoid pro-proliferative effects of Ang II. In line with the proliferation analysis, the application of 10 µM BTP2 resulted in a significant increase in cell death. Ang II alone increased the number of dead cells by trend and the combination of Ang II and BTP2 showed no further increase (Fig. 15B).

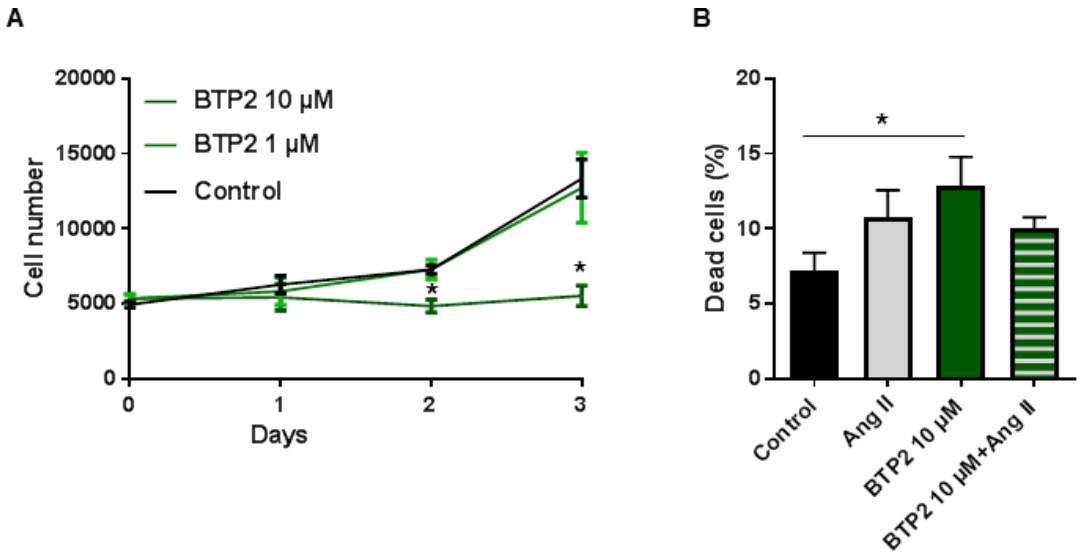

Figure 15: Long-term inhibition of SOCE channels inhibits cell proliferation and increases apoptosis.

A) *The NHCF-V were seeded into 24-well plates. The next day the cells were either directly fixed (day 0) or treated with the indicated concentrations of BTP2 for 1, 2 or 3 days in the presence of serum. The nuclei were stained with DAPI and counted by automatic cell counting. Given are the absolute cell numbers. The values are means±SEM of three independent experiments measured in replicates of 4, *p<0.05 vs. Control, as assessed by two-way ANOVA with Tukey's multiple comparisons.* ***B)*** *Confluent NHCF-V were treated with 10 µM BTP2 in the absence or presence of 100 nM Ang II, after 24 h, the living cells were stained with annexin V-FITC, PI and Hoechst 33342. Fluorescence imaging was performed and the percentage of dead cells was determined. Given are the mean percentages+SEM of annexin V and/or propidium iodide-positive cells of three independent experiments, *p<0.05 as assessed by one-way ANOVA with Tukey's multiple comparisons.*

4.1.4 Influence of SOCE inhibition on the expression and secretion of fibrosis-associated markers in 2D cultures

To identify potential fibrotic factors influenced by Ca^{2+}, changes in the transcription of fibrosis-associated genes and their translated proteins were assessed by RT-qPCR and immunoblotting, respectively. Therefore, serum-starved 2D cultures of

NHCF-V were treated for 24 h with BTP2 in the absence or presence of 100 nM Ang II, 5 ng/ml TGF-β, or a combination of both (AT). The expression changes of

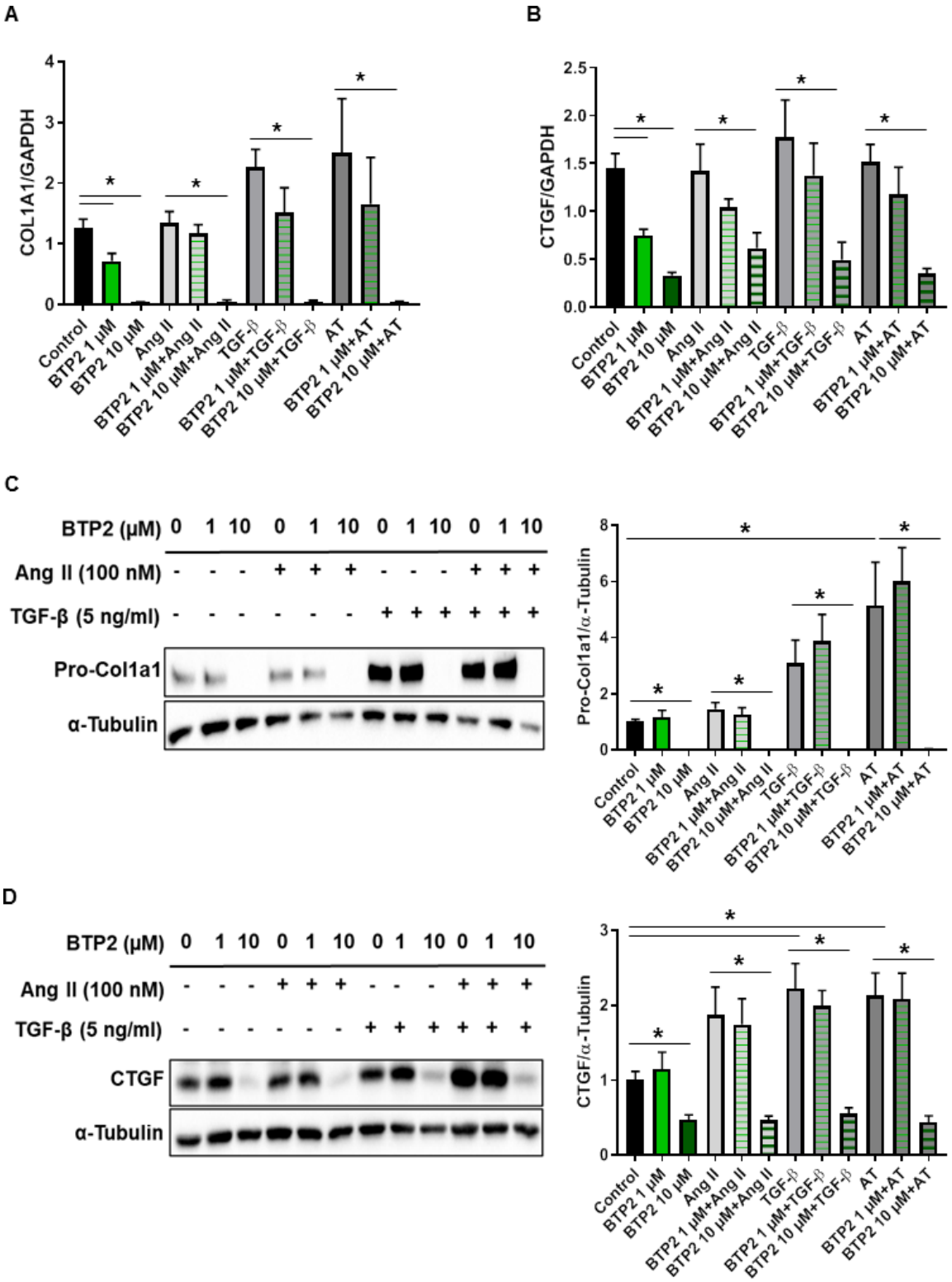

Figure 16: SOCE inhibition suppresses the biochemical induced up-regulation of collagen1a1 and CTGF expression in 2D NHCF-V.

The NHCF-V were treated with 1 µM or 10 µM BTP2 for 2 h and then 100 nM Ang II, 5 ng/ml TGF-β or a combination of both (AT) was added for 24 h. RNA and protein levels were quantified by RT-qPCR and immunoblotting, respectively. ***A-B)*** *Quantitative data of the transcriptional change of COL1A1* ***(A)*** *and CTGF* ***(B)*** *normalized by GAPDH are given as means+SEM of three independent experiments with three technical replicates each, *p<0.05 as assessed by one-way ANOVA with Tukey's multiple comparisons*. ***C-D)*** *Representative immunoblots of the uncleaved pre-form of Col1a1 (Pro-Col1a1)* ***(C)*** *and of CTGF* ***(D)*** *are shown together with α-tubulin as loading control (left). Quantification of the expression in indicated conditions are given in the graph on the right. Shown are the means+SEM normalized by α-tubulin and given relative to control of 3-4 independent experiments, *p<0.05 as assessed by one-way ANOVA with Tukey's multiple comparisons*.

the two important fibrosis markers collagen1a1 (gene: COL1A1, unprocessed protein: Pro-Col1a1) and connective tissue growth factor (CTGF) were investigated. As shown in Figure 16A and 16B, the treatment with TGF-β, Ang II or AT was without significant effect on the transcription of COL1A1 and CTGF. Ten µM BTP2 downregulated the expression of both genes in all conditions significantly, whereas 1 µM BTP2 showed significant effect only in the absence of fibrotic mediators, and intermediate regulation was seen in most conditions in the presence of mediators. Next, the protein levels of the nascent, uncleaved Pro-Col1a1 and of CTGF were assessed in cell lysates by immunoblotting. TGF-β increased the expression of CTGF, and AT of Pro-Col1a1 and CTGF. Pre-treatment with 10 µM BTP2 completely abrogated the Pro-Col1a1 expression and

significantly reduced the CTGF expression in all conditions. One µM BTP2 did not exert any effect (Fig. 16C, 16D).

To assess the effect of BTP2 on the secretion of Pro-Col1a1 and CTGF, the conditioned media from the above-described treatments of NHCF-V were used for immunoblotting. The relative changes between the secreted and intracellular portions of both proteins were assessed. The detected ratios of Pro-Col1a1 and CTGF were significantly higher when the cells were treated with 10 µM BTP2 compared to Control (Fig. 17A, 17B), except for the by trend increase in TGF-β conditions on Pro-Col1a1. One µM BTP2 did not show any effect. This data suggested that 10 µM BTP2 has not only an effect on the expression of both fibrotic markers but also on the ratio of the secreted to the non-secreted protein amount (Fig. 17).

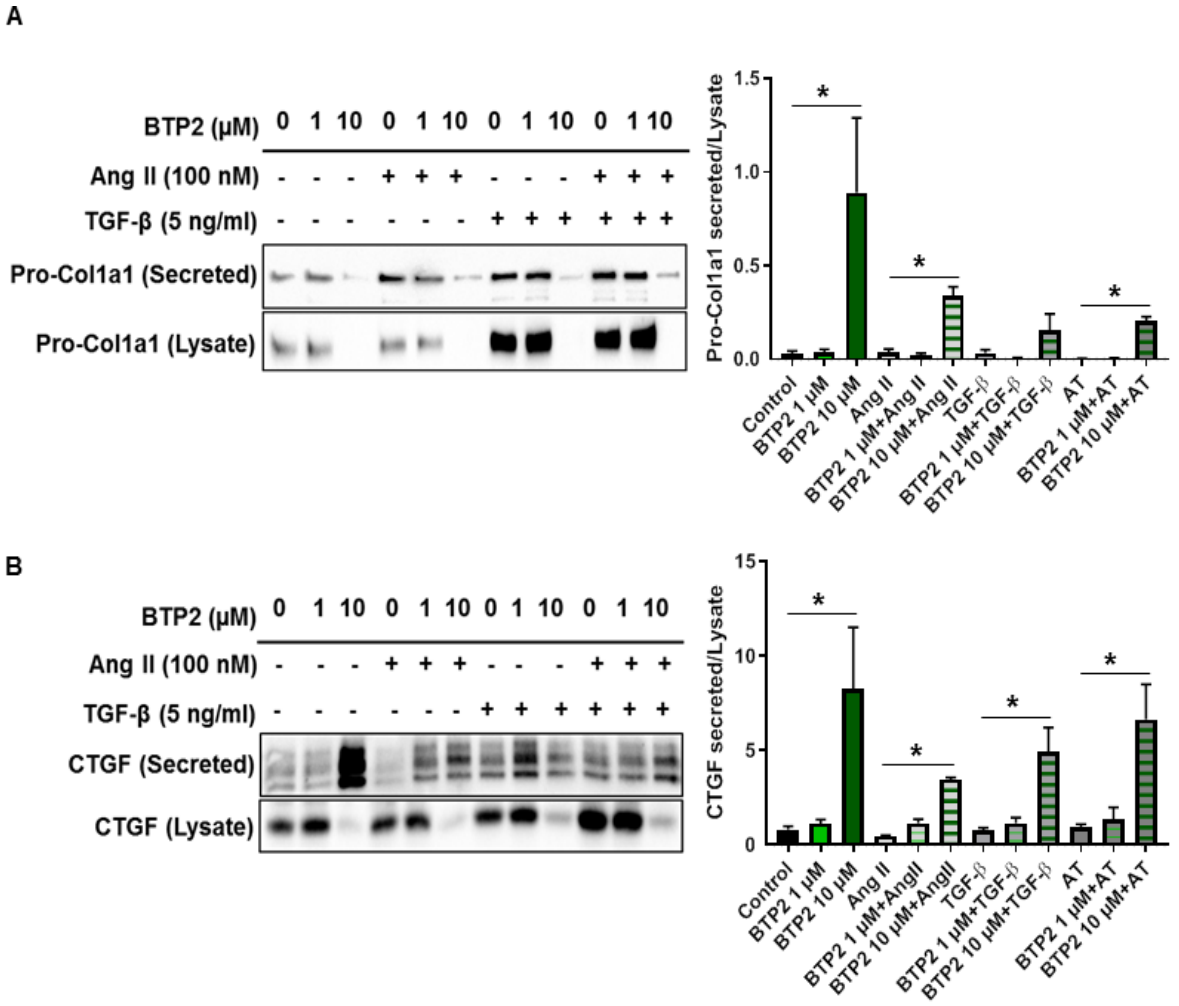

Figure 17: Inhibition of SOCE enhances the secretion of fibrosis-associated proteins in 2D cultures of NHCF-V.

*The NHCF-V were treated with 1 µM or 10 µM BTP2 for 2 h and then 100 nM Ang II, 5 ng/ml TGF-β or a combination of both (AT) was added for 24 h. The conditioned media were collected and used for immunoblotting. Representative immunoblots of the secreted uncleaved preform of Col1a1 (Pro-Col1a1) (A) and of CTGF (B) are shown together with their corresponding detection in lysates. The changes in the secreted levels of Col1a1 (Pro-Col1a1) and of CTGF are given in the bar graphs relative to the intracellular protein levels. The values are means+SEM of three independent experiments, *p<0.05 as assessed by one-way ANOVA with Tukey's multiple comparisons.*

4.1.5 Identification of downstream Ca^{2+} targets regulating the expression of fibrotic markers in 2D NHCF-V

4.1.5.1 Effect of BTP2 on the phosphorylation of the TGF-β effector mediator Smad2

As shown above, BTP2 treatment significantly reduced the expression of fibrosis-associated markers Pro-Col1a1 and CTGF. To investigate if this effect is dependent on the canonical TGF-β signaling, serum starved NHCF-V were treated with different concentrations of BTP2 in the absence or transient presence of Ang II, TGF-β or AT. Then, the phosphorylation of Smad2 was assessed relative to total Smad2/3 by means of immunoblotting. As shown in Figure 18, transient exposure to TGF-β and AT significantly increased the amount of phosphorylated Smad2. This effect was, however, not regulated by any concentration of BTP2. These data clearly demonstrated that the canonical TGF-β-signaling pathway is not involved in the observed BTP2 effects (Fig. 18).

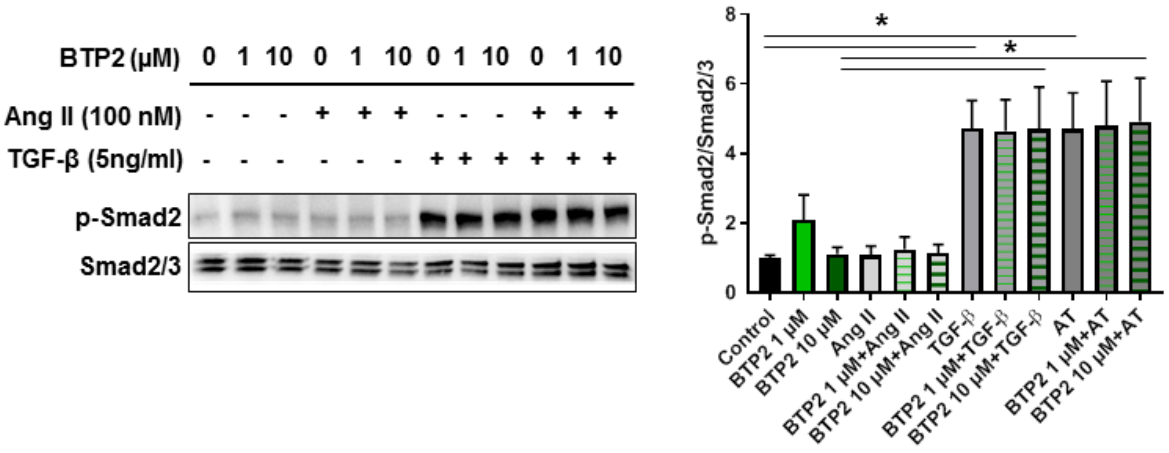

Figure 18: BTP2 has no influence on Smad2 phosphorylation in 2D cultured NHCF-V.

The NHCF-V were treated with 1 µM or 10 µM BTP2 for 2 h and then exposed to 100 nM Ang II, 5 ng/ml TGF-β or a combination of both (AT) for 30 min before

*lysed for protein isolation. Left: A representative immunoblot of the phosphorylated Smad2 isoform (p-Smad2) together with total Smad2/3 is shown. Right: Quantification of the expression in indicated conditions are given in the bar graph. Shown are the means+SEM normalized by Smad2/3 and given relative to control of three independent experiments, *p<0.05 as assessed by one-way ANOVA with Tukey's multiple comparisons.*

4.1.5.2 Influence of calcineurin inhibition on Pro-Col1a1 expression

Next, the potential involvement of the Ca^{2+}-regulated phosphatase calcineurin in the induction of Pro-Col1a1 by the pro-fibrotic mediators was investigated. To this end, serum starved NHCF-V were treated with 20 nM Cyclosporin A (CsA) in the absence or presence of pro-fibrotic mediators and then, expression of Pro-Col1a1 was investigated by immunoblot. Both, TGF-β and AT treatment resulted in an increase in Pro-Col1a1 expression. This increase was, however, not affected by the CsA treatment. This finding revealed that calcineurin had no effect on the TGF-β-induced up-regulation of Pro-Col1a1 in the used NHCF-V, and thus it could be ruled out that calcineurin is involved in the BTP2-dependent reduction in Pro-Col1a1 expression (Fig. 19).

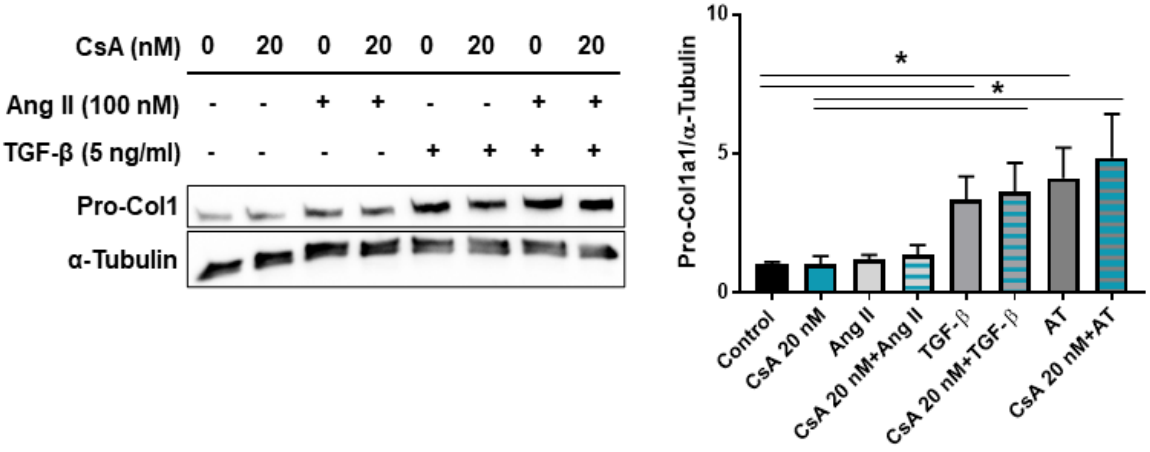

Figure 19: TGF-β up-regulated Pro-Col1a1 expression independent of calcineurin in 2D NHCF-V.

*The NHCF-V were treated with 20 nM CsA for 1 h and then 100 nM Ang II, 5 ng/ml TGF-β or a combination of both (AT) was added for 24 h. The uncleaved pre-form of Col1a1 (Pro-Col1a1) was quantified by immunoblotting. Left: Representative immunoblots of Pro-Col1a1 are shown together with α-tubulin as loading control. Right: Quantification of the expression in the indicated conditions is given in the graph. Shown are the means+SEM normalized by α-tubulin and given relative to control of five independent experiments, *p<0.05 as assessed by one-way ANOVA with Tukey's multiple comparisons.*

4.1.5.3 Influence of thapsigargin on ER-stress and fibrotic markers expression in 2D NHCF-V

As shown above, BTP2 did not show any interference with Smad2 phosphorylation and the calcineurin inhibition had no effect on Pro-Col1a1 expression under fibrotic conditions. Next, the influence of ER Ca^{2+} depletion was studied, therefore, NHCF-V were treated with the SERCA pump inhibitor thapsigargin (TGN) in the absence or presence of pro-fibrotic mediators to assess its effect on the ER-stress marker binding immunoglobulin protein (BiP) and on the fibrotic markers Pro-Col1a1 and CTGF. Immunoblot analysis showed that TGN treatment up-regulated BiP expression as expected, because the ER Ca^{2+} depletion results in the induction of ER stress [156]. Interestingly, Pro-Col1a1 as well as CTGF expression was completely abrogated by TGN independent of an additional treatment with the pro-fibrotic factors. Thus, TGN mimicked the effect of BTP2 in the regulation of both proteins (Fig. 20).

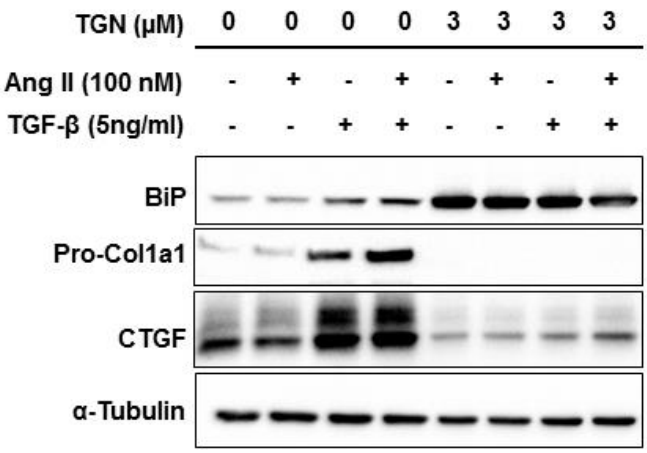

Figure 20: Thapsigargin up-regulated BiP and downregulated fibrotic markers in 2D NHCF-V.

The NHCF-V were treated with 3 μM TGN for 1 h and then 100 nM Ang II, 5 ng/ml TGF-β or a combination of both (AT) was added for 24 h. BiP, Pro-Col1a1 and CTGF expression was assessed by immunoblotting. Representative immunoblots of the BiP, Pro-Col1a1 and CTGF are shown together with α-tubulin as loading control.

4.1.5.4 Effect of BTP2 on ER-stress markers in 2-D NHCF-V

As shown above, SERCA inhibitor TGN up-regulated BiP but downregulated Pro-Col1a1 and CTGF expression under fibrotic conditions, which prompted us to examine the effect of BTP2 on ER-stress markers. Therefore, NHCF-V were treated with BTP2 in the absence or presence of Ang II, TGF-β and AT and then transcripts of ER-stress regulating genes like HSPA5 and DDIT3 and the protein markers BiP (product of HSPA5) and PERK were investigated. Ten μM BTP2 significantly up-regulated HSPA5 and DDIT3 transcripts in all conditions. The pro-fibrotic mediators alone and 1 μM BTP2 did not show any effect (Fig. 21A, 21B). In line, BiP was significantly up-regulated with 10 μM BTP2 under basal and in the presence of TGF-β, and by trend when Ang II and AT were added with BTP2. One

μM BTP2 was without significant effect (Fig. 21C). The expression of PERK showed no significant changes (Fig. 21D).

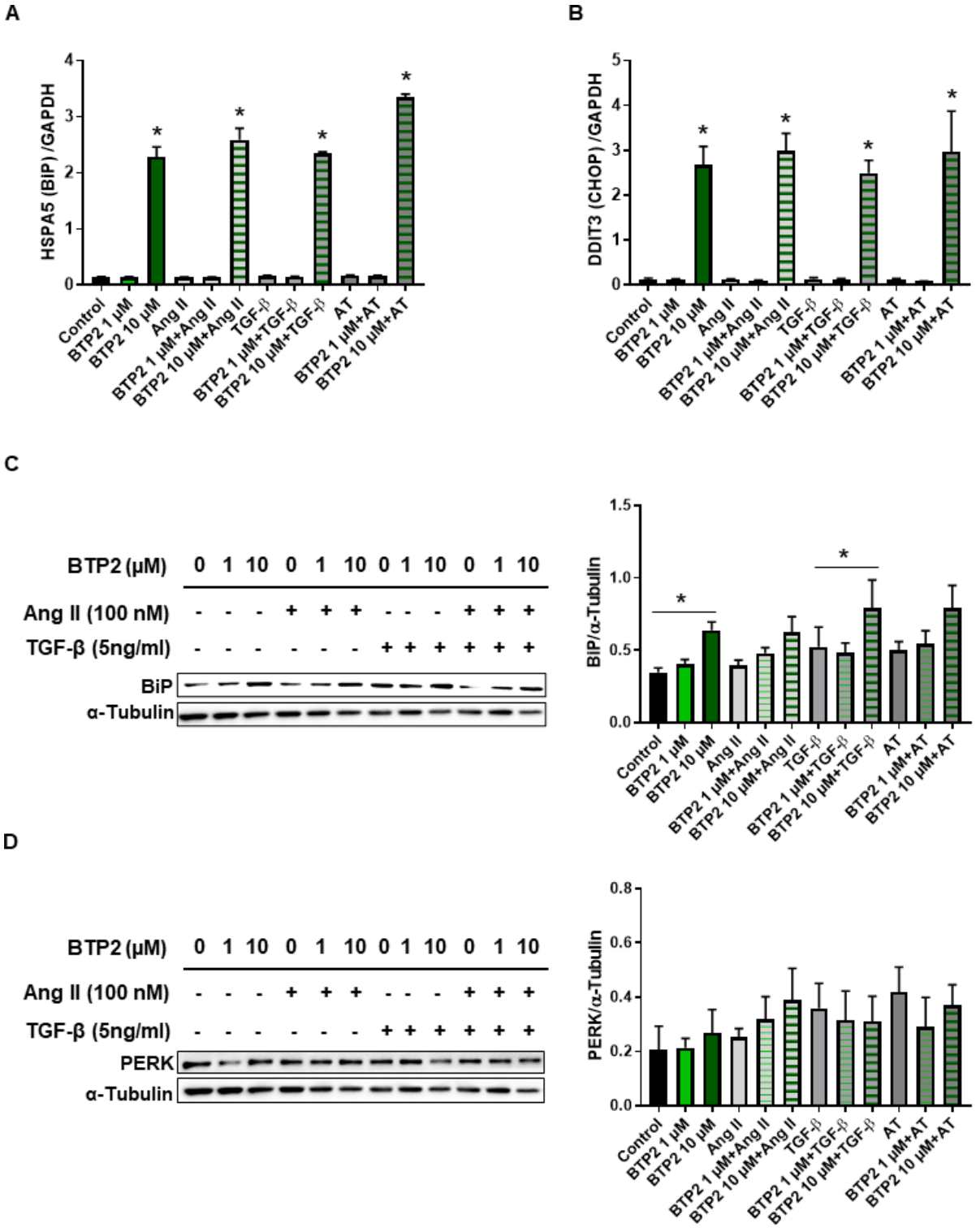

Figure 21: SOCE inhibitor BTP2 up-regulates ER-stress markers in 2D NHCF-V.

The NHCF-V were treated with 1 µM or 10 µM BTP2 for 2 h and then 100 nM Ang II, 5 ng/ml TGF-β or a combination of both (AT) was added for 24 h. RNA and protein levels were quantified by RT-qPCR and immunoblotting, respectively. ***A-B)*** *Quantitative data of the transcriptional change of HSPA5* ***(A)*** *and DDIT3* ***(B)*** *normalized by GAPDH are given as means+SEM of three independent experiments with three technical replicates each, *p<0.05 vs. the respective condition without BTP2 (Control, Ang II, TGF-β, AT), as assessed by one-way ANOVA with Tukey's multiple comparisons.* ***C-D)*** *Left: Representative immunoblots of the BiP* ***(C)*** *and of PERK* ***(D)*** *are shown together with α-tubulin as loading control. Right: Quantification of the expression in indicated conditions are given. Shown are the means+SEM normalized by α-tubulin in 4-5 independent experiments, *p<0.05 as assessed by one-way ANOVA with Dunnett's post hoc analysis individually performed for each treatment group.*

4.2 Influence of the TRPC3 inhibition on the Ca^{2+} handling, cell viability and Pro-Col1a1 expression in 2D cultures of NHCF-V

4.2.1 Transient receptor potential channel3 (TRPC3) inhibition reduces basal and Ang II-induced Ca^{2+} oscillations and Ang II-induced Ca^{2+} transients in NHCF-V

In addition to the SOCE inhibitor BTP2, the effect of the transient receptor potential channel 3 (TRPC3) inhibitor pyrazole 3 (Pyr3) on the Ca^{2+} oscillation and transient in NHCF-V was investigated in this thesis. Therefore, NHCF-V were pre-treated with Pyr3 for 1 h and then live Ca^{2+} imaging was performed for 5 min to determine the number of Ca^{2+} oscillating cells as described before. It was found that the basal Ca^{2+} oscillations were concentration dependently reduced, resulting in a reduction by 23% and 40% with 1 µM and 3 µM Pyr3, respectively (Fig. 22A). Then, Ang II was applied in the absence or presence of Pyr3 and oscillation was determined. Ang II significantly increased the number of oscillating cells by 21% compared to control and Pyr3 reduced the number of oscillating cells by 40% in the absence of

Ang II and by 25% in the presence of Ang II (Fig. 22B). This reveals that TRPC3 inhibition reduced the basal and Ang II-induced Ca^{2+} oscillations in NHCF-V.

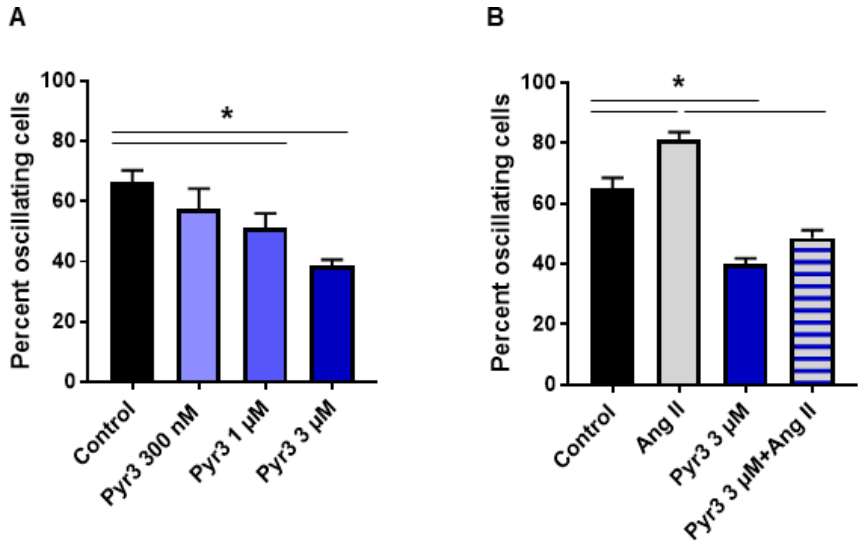

Figure 22: Ca^{2+} oscillation involves TRPC3 mechanisms in NHCF-V.

*NHCF-V were pre-incubated with the indicated concentrations of Pyr3 for 1 h and then loaded with the cytosolic Ca^{2+} dye Fluo-8. The percentages of Ca^{2+} oscillation cells were assessed by live-cell imaging in the absence (A) and presence (B) of 100 nM Ang II. The presented values are means+SEM of 4-5 independent experiments with at least 300-470 cells per group analyzed, *p<0.05 as assessed by one-way ANOVA with Tukey's multiple comparisons.*

Then, the contribution of TRPC3 channels to the Ang II-induced Ca^{2+} transient in NHCF-V was investigated by pre-treatment with Pyr3. Pyr3 application resulted in a concentration-dependent decline in the amplitude of the Ca^{2+} transient. One µM and 3 µM Pyr3 significantly reduced the Ca^{2+} transient from the start of induction, whereas 300 nM Pyr3 showed only an effect at the late decay phase of the transient. All three Pyr3 concentrations reduced the resting calcium after the transient, with 3 µM showing a significant difference (Fig. 23).

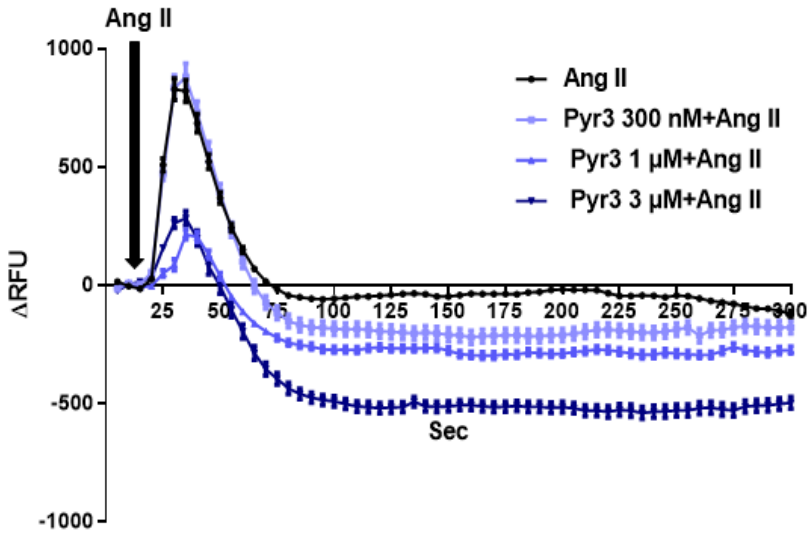

Figure 23: The Ang II-induced Ca^{2+} transient involves TRPC3 in NHCF-V.

The NHCF-V were pre-incubated with 300 nM, 1 µM or 3 µM Pyr3 for 1 h and then loaded with Fluo-8. The Ca^{2+} transients were elicited by the application of 100 nM Ang II. Changes in intracellular Ca^{2+} were recorded by live-cell imaging. The presented values are background-subtracted changes in the fluorescence traces given as means±SEM of 4-5 independent experiments (with at least 300-470 cells in total per condition). The p-values are <0.05 from 70th sec for 300 nM, from 25th sec for 1 µM and 3 µM Pyr3 vs. Control as assessed by two-way ANOVA with Tukey's multiple comparisons.

4.2.2 Influence of TRPC3 inhibition on the proliferation and apoptosis in 2D NHCF-V

Ca^{2+} influx inhibition through SOCE channels has shown significant effects on viability and proliferation in NHCF-V. Therefore, the influence of TRPC3 inhibition on proliferation of NHCF-V was investigated in the presence of 1 µM and 3 µM Pyr3 for 3 consecutive days. Compared to control, Pyr3 showed a concentration-dependent decline in cell number at day 2 and 3. In case of 1 µM Pyr3, a low rate of cell proliferation was still detectable. In contrast, 3 µM of Pyr3 led already after 2 days to a considerable cell loss compared to the number of initially seeded cells

proclaiming cytotoxicity (Fig. 24A). Next, the effect of Pyr3 on the viability and cell death by necrosis/apoptosis was studied in the same way as described before for BTP2. Three µM of Pyr3 resulted in a significant increase in cell death which is in agreement with the proliferation data. Ang II alone increased the number of dead cells by trend and the combination of Ang II with Pyr3 did not show further increase (Fig. 24B).

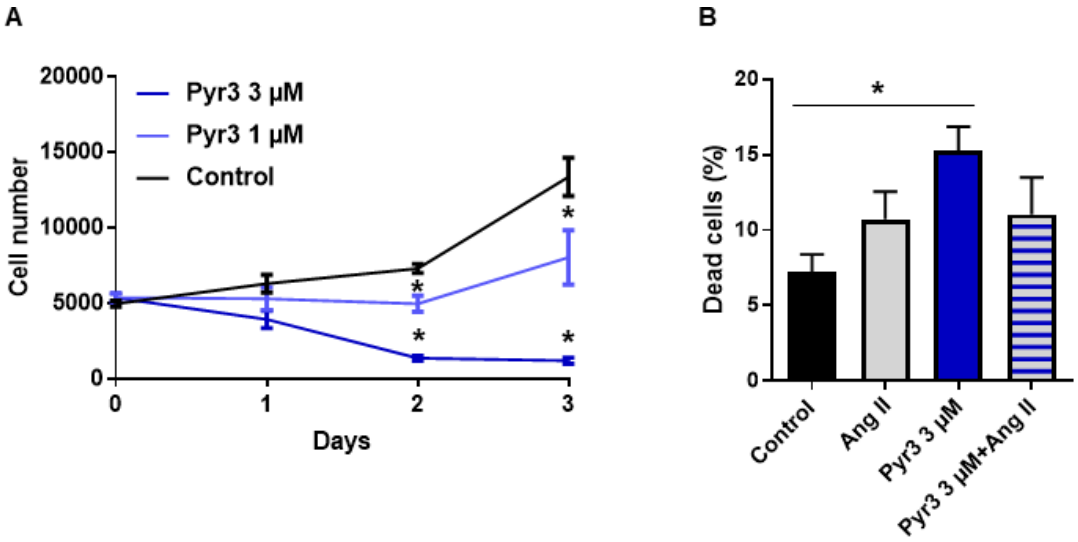

Figure 24: Long-term inhibition of TRPC3 channels inhibits cell proliferation and increases apoptosis.

A) *The NHCF-V were seeded into 24-well plates. The next day the cells were either directly fixed (day 0) or treated with the indicated concentrations of Pyr3 for 1, 2 or 3 days in the presence of serum. The nuclei were stained with DAPI and counted by automatic cell counting. Given are the absolute cell numbers. The values are means±SEM of three independent experiments measured in replicates of 4, *p<0.05 vs. Control as assessed by two-way ANOVA with Tukey's multiple comparisons.* ***B)*** *Confluent NHCF-V were treated with 3 µM Pyr3 in the absence or presence of 100 nM Ang II, after 24 h, the living cells were stained with annexin V-FITC, PI and Hoechst 33342. Fluorescence imaging was performed and the percentage of dead cells was determined. Given are the mean percentages+SEM of annexin V and/or propidium iodide positive cells of three independent*

*experiments, *p<0.05 as assessed by one-way ANOVA with Tukey's multiple comparisons.*

4.2.3 Influence of TRPC3 inhibition on the expression of Pro-Col1a1 in 2D cultures of NHCF-V

To identify potential molecular mechanisms which could be influenced by Ca^{2+} influx through TRPC3 channels, immunoblot analysis was performed. Therefore, 2D cultures of NHCF-V were treated for 24 h with Pyr3 (0.3 µM and 3 µM) in the absence or presence of AT and the expression of Pro-collagen1a1 was investigated showing that none of the used Pyr3 concentrations had any effect (Fig. 25).

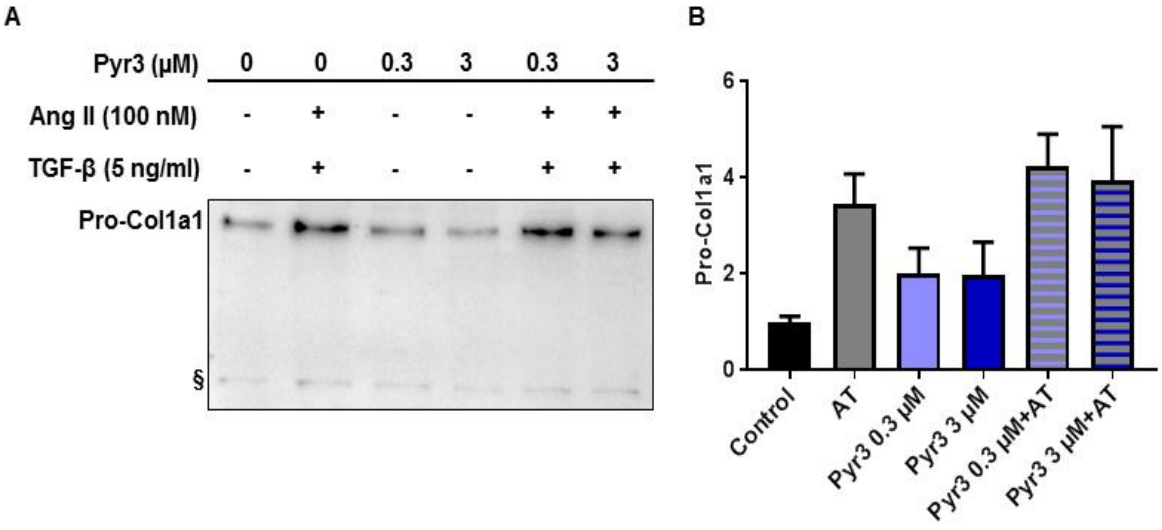

Figure 25: TRPC3 inhibition has no effect on the AT-dependent increase in Pro-collagen1a1 in 2D NHCF-V.

*The NHCF-V were treated with 0.3 µM or 3 µM Pyr3 for 2 h and then AT was added for 24 h. Representative immunoblot of the uncleaved pre-form of Col1a1 (Pro-Col1a1) is shown in **(A)** Quantification of the expression in indicated conditions are given in **(B)** were normalized to the unspecific band (marked with §) and are relative to control. Shown are means+SEM of 3-4 independent experiments.*

4.3 Influence of the inhibition of the SOCE on the fibrotic remodeling of hECT

4.3.1 TGF-β increases the contraction of hECT

As the data obtained from 2D cultures suggested that BTP2 might act as an anti-fibrotic drug by inhibiting cell proliferation and the expression of fibrosis-associated genes in NHCF-V, the next aim was to investigate its effect on 3D engineered human connective tissues (hECT) under basal and fibrotic conditions. To this end, fibrotic agents were first tested in the absence of BTP2. Therefore, NHCF-V were cultured in a collagen matrix for up to 5 days and were treated with 100 nM Ang II, 5 ng/ml TGF-β or the combination of both (AT). The molds used for tissue generation contained two flexible poles, which allowed to determine hECT contraction. The maximum contraction of the tissues was reached after around 3 days independent of the treatment. Under basal condition, tissue contraction was 24% at day 5. Surprisingly, Ang II was without additional effect on tissue contraction compared to control. In contrast, AT treatment induced an increase in contraction starting from day 1 on and resulting in a 54% higher contraction at day 5 when compared to control. TGF-β alone demonstrated a slightly lower effect as AT, however, the difference was only at day 3 significant (Fig. 26).

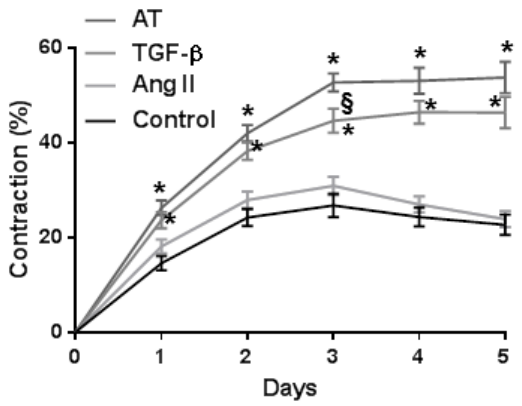

Figure 26: Influence of pro-fibrotic mediators on hECT contraction.

*hECT were generated from NHCF-V and collagen type I and treated with 100 nM Ang II, 5 ng/ml TGF-β or a combination of both (AT) for 5 days. The deflection of the flexible tissue-holding poles was analyzed on a daily basis to determine tissue contraction. The changes in percent compared to day 0 are given as means±SEM of 3-4 independent experiments with 12-48 hECT per group, *p<0.05 vs. Control, §p<0.05 vs. AT, as assessed by two-way ANOVA with Tukey's multiple comparisons.*

4.3.2 The compaction of hECT is enhanced by TGF-β

After investigating the effect of the pro-fibrotic factors on hECT contraction, their impact on the cross-sectional areas (CSA) and volumes of the tissues were studied next as a measure of tissue compaction after 3 and 5 days of culture. The CSA and volumes of the hECT were calculated from macroscopic images (as described in section 3.2.6). Under control conditions, the CSA and volumes moderately increased between day 3 and day 5. Compared to control, TGF-β and AT reduced the CSA and volumes at day 3 and day 5, and Ang II at day 5 only. Moreover, TGF-β and AT treatment resulted in a decline in hECT volumes between day 3 and day 5 (Fig. 27).

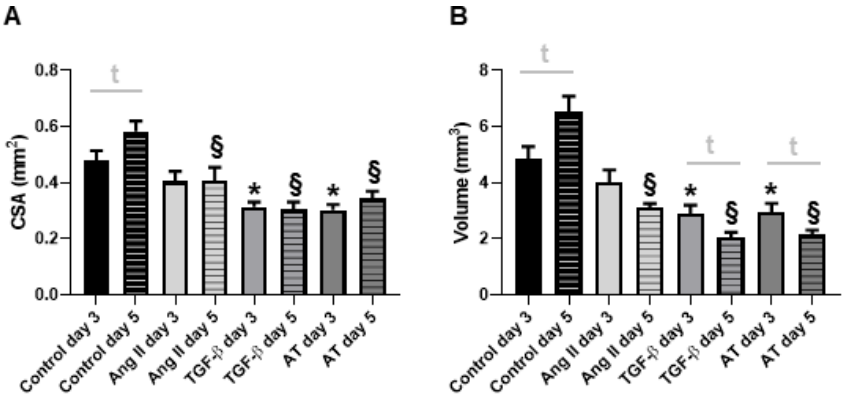

Figure 27: Influence of pro-fibrotic mediators on hECT compaction.

hECT were generated from NHCF-V and collagen type I and treated with 100 nM Ang II, 5 ng/ml TGF-β or a combination of both (AT) for 3 or 5 days. Macroscopic images of the hECT were taken to determine the cross-sectional areas (CSA) ***(A)*** *and volumes* ***(B)*** *of the tissues. The values are given as means+SEM with 11-25 hECT per group, *p<0.05 vs. Control day 3, §p<0.05 vs. Control day 5 as assessed by one-way ANOVA with Dunnett's post hoc analysis, ^{t}p<0.05 as assessed by an unpaired t-test.*

4.3.3 Pro-fibrotic mediators complexly regulate the biomechanical properties of hECT

To test the influence of the pro-fibrotic mediators on the biomechanical properties of the hECT, destructive tensile strength measurements were performed after 3 or 5 days of treatment with 100 nM Ang II, 5 ng/ml TGF-β or AT (as described in section 3.2.7). The slope of the elastic phase from the obtained stress-strain curves, representing the Young's modulus and thus the tissue stiffness, was calculated. The stiffness of the hECT increased under control conditions between day 3 and day 5, compared to control with TGF-β at day 3 and with AT at day 3 and day 5. The increase observed with TGF-β at day 5 was not significant due to the large data variance (Fig. 28).

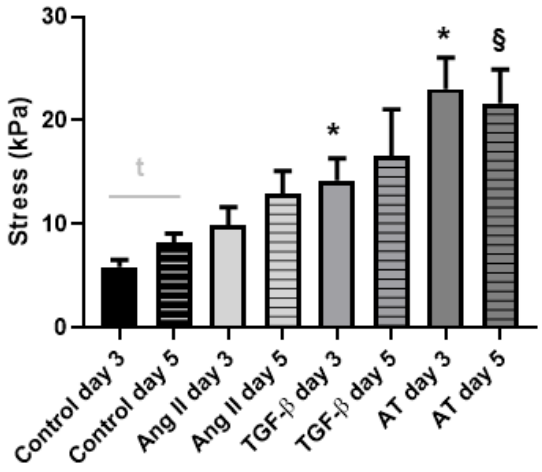

Figure 28: Influence of pro-fibrotic mediators on the stiffness of hECT.

*hECT were generated from NHCF-V and collagen type I and treated with 100 nM Ang II, 5 ng/ml TGF-β or a combination of both (AT) for 3 or 5 days. Rheometry was performed and the obtained stress-strain curves were used to determine the Young's moduli (slope of the elastic phase) reflecting tissue stiffness. The values are depicted as means+SEM with 8-20 hECT per group, *p<0.05 vs. Control day 3, §p<0.05 vs. Control day 5 as assessed by one-way ANOVA with Dunnett's post hoc analysis, ^{t}p<0.05 as assessed by an unpaired t-test.*

In addition to the Young's modulus, other parameters of the elastic region were determined. This included the yield point strain and the yield point stress, also known as the proportional limit, as well as the energy which was absorbed in this phase representing the tissue's resilience.

Yield point strain was determined from the point just before the start of the permanent deformation of tissues. The yield point strain was significantly decreased in control-, Ang II- and AT-treated tissues and by trend in TGF-β-treated tissues between day 3 and day 5. No significant differences could be observed by the treatments when compared to control at the respective days (Fig. 29A). The

yield point stress was increased under all pro-fibrotic mediator conditions at day 3, but not at day 5. By direct comparison of day 3 and day 5 data, a decline in the yield point stress was found when the hECT were treated with TGF-β or AT (Fig. 29B). The resilience depicted as AUC was significantly reduced with AT treatment at day 5 when compared to control tissues at day 5 and to AT tissues at day 3. This decline in resilience between day 3 and day 5 was also found in all other conditions, however, it was not significant when TGF-β was used alone (Fig. 29C).

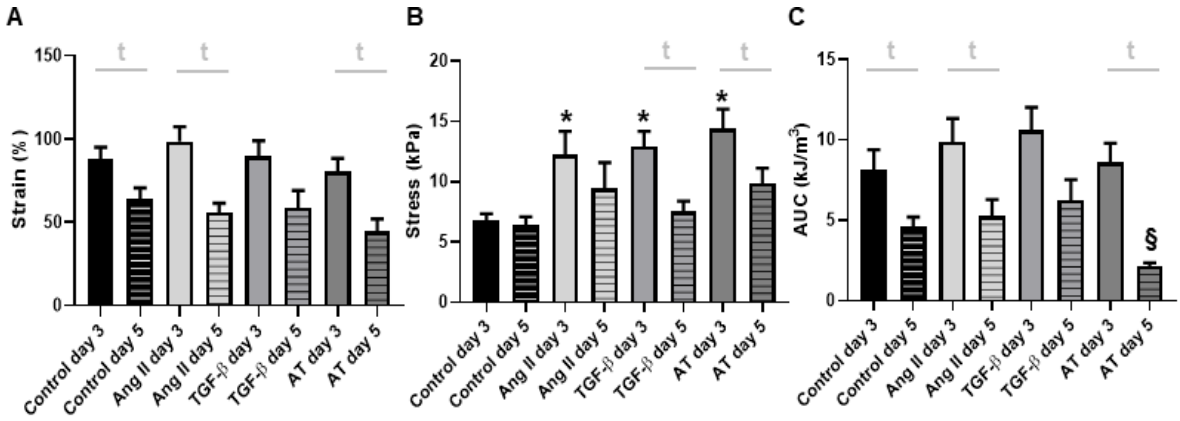

Figure 29: Influence of pro-fibrotic mediators on the yield point and the resilience of hECT.

*The yield point was determined in the stress-strain curves and the strain **(A)** and stress **(B)** values are given. The resilience was calculated as area under the curve of the elastic phase **(C)**. Given are the values as means+SEM with 7-23 hECT per group, *p<0.05 vs. Control day 3, §p<0.05 vs. Control day 5 as assessed by one-way ANOVA with Dunnett's post hoc analysis, ^{t}p<0.05 as assessed by an unpaired t-test.*

The elastic phase of a stress-strain curve is followed by the plastic phase, in which an irreversible deformation of the hECT occurs. The irreversibility is based on initial microfractures of the tissue and results at the end in the ultimate rupture of the

tissue. To characterize this phase, the ultimate tissue strength, the extensibility given by the ultimate strain, and the toughness were measured based on the stress-strain curves.

The ultimate strength increased in Ang II, TGF-β and AT compared to control at day 3, however, no changes were observed at day 5. The fibrotic treatment resulted in a decline in the ultimate strength between day 3 and day 5, which was found to be significant for the AT treatment (Fig. 30A). The ultimate strain to the failure point was decreased with AT compared to control at day 5 and to AT at day 3. Under all other conditions, the ultimate strain of the hECT cultured for 5 days were significantly or by trend lower than 2 days before (Fig. 30B). The toughness calculated from AUC of elastic and plastic regions was by trend or significantly increased with all pro-fibrotic mediators at day 3, but not at day 5. Consequently, a decline in the toughness was detectable between day 3 and day 5 in these conditions (Fig. 30C).

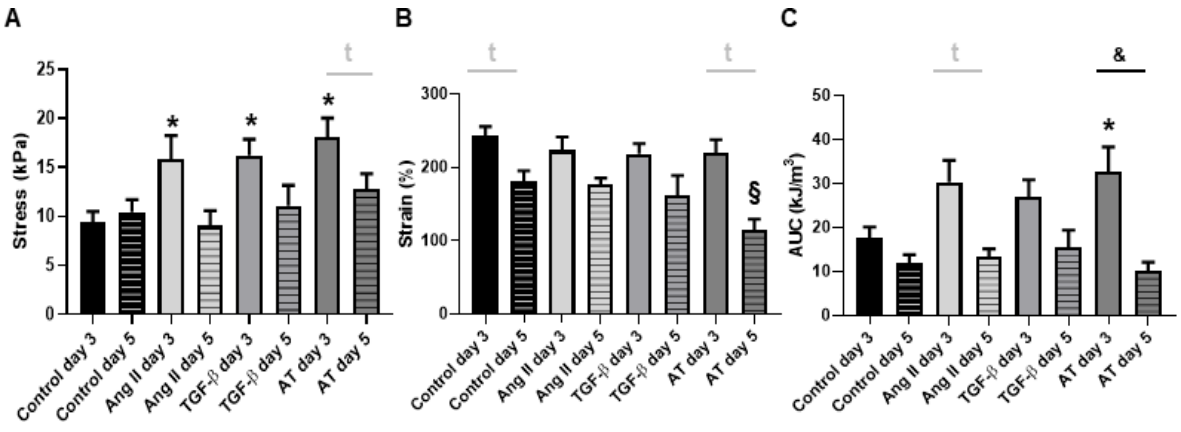

Figure 30: Influence of pro-fibrotic mediators on the strength and the extensibility of hECT.

*The ultimate strength **(A)**, the ultimate strain **(B)** and the toughness (total absorbed energy) **(C)** were determined based on the stress-strain analysis. The values are*

*given as means+SEM of 7-23 tissues per group, *p<0.05 vs. Control day 3, §p<0.05 vs. Control day 5 as assessed by one-way ANOVA with Dunnett's post hoc analysis, &p<0.05 as assessed by one-way ANOVA with Tukey's multiple comparisons, tp<0.05 as assessed by an unpaired t-test.*

4.3.4 Pro-fibrotic treatment had no influence on the cell number in hECT

To assess if any of the treatments had an impact on the viability of the embedded cells, the cells were re-isolated by collagenase and Accutase digestion and analyzed by electronic current exclusion technology. Although there was a general loss of cells, in particular with Ang II between day 3 and day 5, no influence of Ang II, TGF-β or AT could be detected (Fig. 31).

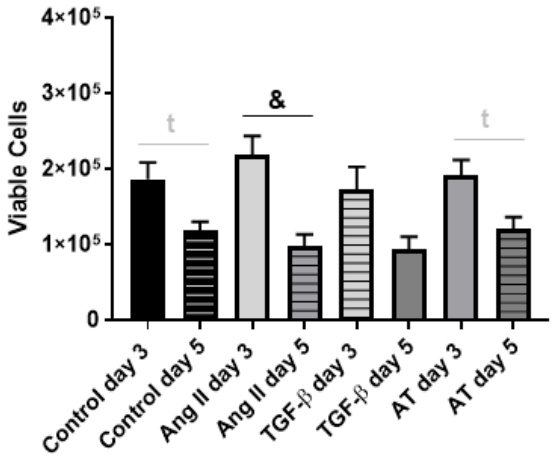

Figure 31: Influence of pro-fibrotic mediators on the cell number in hECT.

The hECT were cultured for 3 or 5 days in the presence of 100 nM Ang II, 5 ng/ml of TGF-β, or both factors. The cells were re-isolated from individual hECT by a collagenase/Accutase digest and the viable cells were counted by electronic current exclusion. The given values are means+SEM of 2-4 independent experiments with 6-12 hECT digested in each group, &p<0.05 as assessed by one-way ANOVA with Tukey's multiple comparisons, tp<0.05 as assessed by an unpaired t-test.

4.3.5 Pro-fibrotic mediators moderately influenced the cell-cycle activity of NHCF-V in hECT

Given that pro-fibrotic treatments had shown no effect on the viability of NHCF-V in hECT, the proliferation status was assessed next by studying cell-cycle activity. To this end, cells were re-isolated from tissues cultured in pro-fibrotic mediator conditions for 3 or 5 days and then stained with DNA-binding dye before flow cytometry analysis. In these experiments, it was found that approximately 80% cells were arrested in G_0/G1-phase in all conditions and a moderate increase was noted under basal control at day 5 compared to day 3. In S-phase, approximately 50% cells were decreased in control from day 3 to day 5 and a decline by trend was observed with pro-fibrotic treatments between both days. In G2/M-phase, a moderate decrease was shown from day 3 to day 5. In contrast to the differences between the two time points, the exposure to the pro-fibrotic mediators showed no effect compared to control at day 3 and day 5 (Fig. 32).

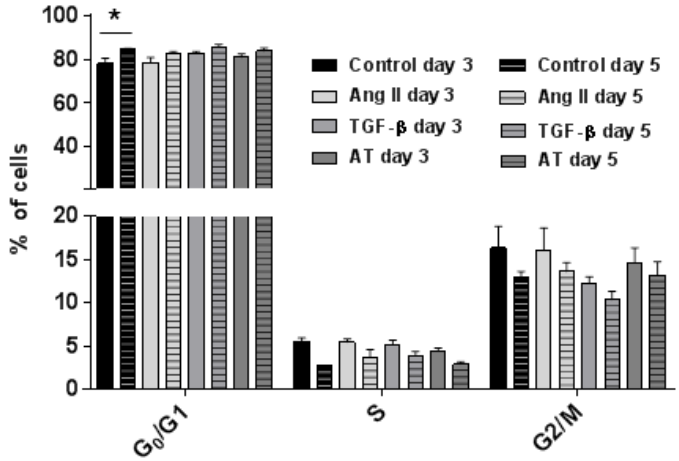

Figure 32: Influence of pro-fibrotic mediators on the cell-cycle activity in hECT.

The hECT were treated with100 nM Ang II, 5 ng/ml TGF-β or the combination of both (AT) for 3 or 5 days. The cells were re-isolated from individual hECT by a

*collagenase/Accutase digest and then stained with Hoechst 33342 for flow cytometry. The percentages of cells in the G1-, S-, and G2/M-phase of the cell cycle are shown. The given values are means+SEM of 5-7 hECT digested in each group, *p<0.05 as assessed by two-way ANOVA with Tukey's multiple comparisons.*

4.3.6 Pro-fibrotic mediators moderately up-regulated fibrosis-associated genes in hECT

To examine the molecular changes induced by pro-fibrotic mediators in hECT, transcript levels of fibrotic markers were investigated. Therefore, essential ECM-constituting or -regulating genes like COL1A1, CCN1 and CTGF were analyzed by RT-qPCR. The transcription of COL1A1 was up-regulated by TGF-β at day 3 and also increased by trend with AT at day 3 and day 5 (Fig. 33A). The transcripts of CTGF showed mild induction with TGF-β and AT at day 3 and day 5 (Fig. 33B). CCN1 was moderately up-regulated at the mRNA level with AT at day 5 and by trend increased with TGF-β and AT at day 3 (Fig. 33C).

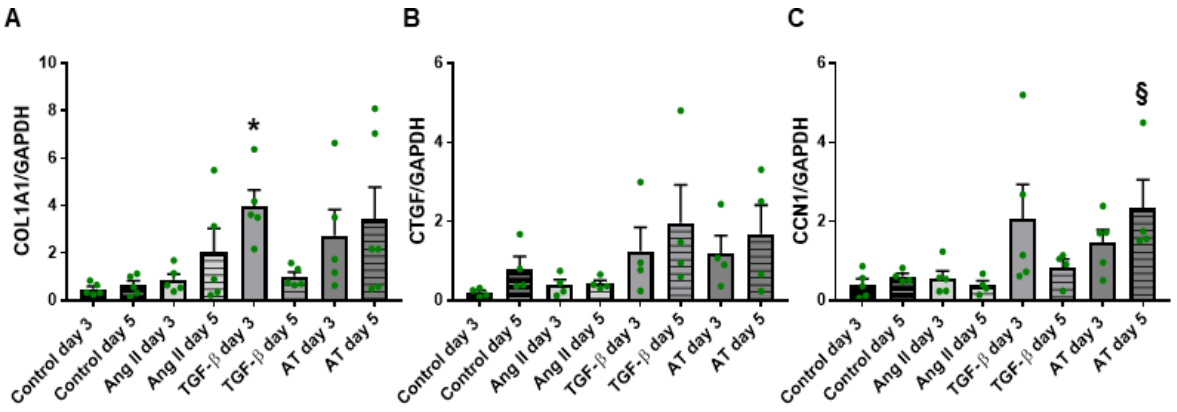

Figure 33: Influence of pro-fibrotic mediators on the fibrotic gene markers in hECT.

hECT were cultured with pro-fibrotic mediators 100 nM Ang II, 5 ng/ml TGF-β or combination of both (AT) for 3 or 5 days and changes in transcript levels of fibrotic gene markers were assessed by RT-qPCR. Quantification of transcripts of

COL1A1 ***(A)****, CTGF* ***(B)*** *and CCN1* ***(C)*** *normalized by GAPDH are given as means+SEM of 4-6 independent experiments with three technical replicates each. A minimum of three hECT were pooled/grouped in each experiment, *p<0.05 vs. Control day 3, §p<0.05 vs. Control day 5 as assessed by one-way ANOVA with Dunnett's post hoc analysis.*

4.3.7 Pro-fibrotic mediators had moderate influence on ER-stress markers in hECT

Next, the influence of pro-fibrotic mediators was assessed on ER-stress response genes. To this end, transcriptional changes in HSPA5 and DDIT3 were analyzed by RT-qPCR. The transcripts of HSPA5 did not show any pro-fibrotic mediators or day dependent effect (Fig. 34A) and DDIT3 revealed an increase by trend under basal control, Ang II and AT conditions from day 3 to day 5 (Fig. 34B).

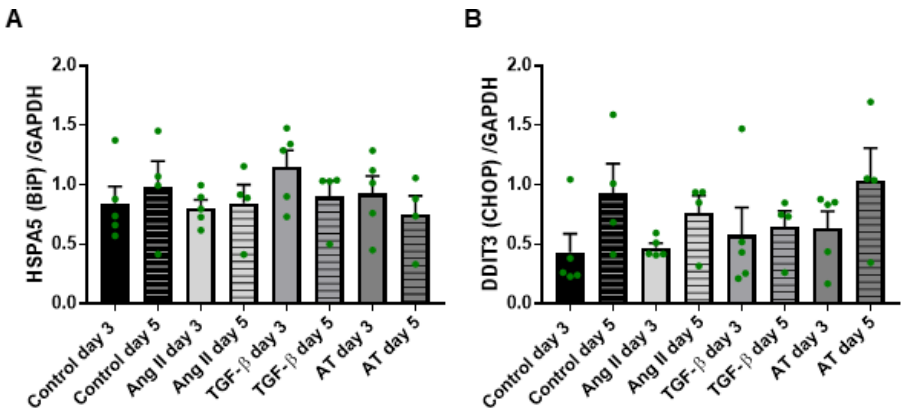

Figure 34: Influence of pro-fibrotic mediators on ER-stress markers in hECT.

hECT were cultured with pro-fibrotic mediators 100 nM Ang II, 5 ng/ml TGF-β or the combination of both (AT) for 3 or 5 days and changes in the levels of transcripts of ER-stress regulating genes were assessed by RT-qPCR. Quantification of transcripts of HSPA5 (BiP) ***(A)****, DDIT3 (CHOP)* ***(B)*** *normalized by GAPDH are given as means+SEM of 4-5 independent experiments with three technical replicates each. A minimum of three hECT were pooled/grouped in each experiment.*

4.3.8 The store-operated Ca^{2+} entry inhibitor BTP2 reduced contraction of hECT

The influence of the SOCE inhibitor BTP2 on hECT was measured under basal conditions as well as in the presence of 100 nM Ang II and 5 ng/ml TGF-β (AT). The inhibitor concentration used in these experiments was 10 µM, as this concentration showed in the 2D experiments the most prominent results. The effect of BTP2 on hECT contraction was assessed as a first readout of its anti-fibrotic potential. Thereby, it was found that BTP2 abrogated under basal conditions the contraction from day 2 until day 4, and in the presence of AT from day 2 to day 5 compared to AT (Fig. 35).

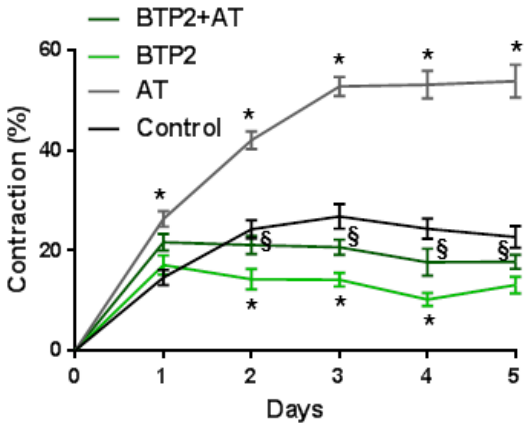

Figure 35: Effect of BTP2 on AT-induced contraction of hECT.

*hECT were generated from NHCF-V embedded in collagen type I and then treated with 10 µM BTP2 in the absence or presence of AT (100 nM Ang II and 5 ng/ml TGF-β) for 5 days. The deflection of flexible tissue-holding poles was recorded on daily basis for contraction measurements. The changes in contraction percentage compared to day 0 are given as means±SEM of 3-4 experiment with 12-48 tissues per group, *p<0.05 vs. Control, §p<0.05 vs. AT, as assessed by two-way ANOVA with Tukey's multiple comparisons.*

4.3.9 BTP2 reduced pro-fibrotic mediators induced compaction of hECT

Next, to assess the effect of BTP2 on the compaction of the hECT, CSA and volumes were measured after 3 or 5 days of culturing in the presence or absence of the pro-fibrotic mediator combination AT. Both the CSA and the volumes increased either significantly or by trend in all conditions between day 3 and day 5, except of in the presence of AT. BTP2 treatment moderately increased both parameters at both days when compared to control, however, the increase was only significant for the CSA at day 5. As shown before, the AT treatment resulted in a decline in CSA and volume at both days compared to control tissues, which was suppressed by BTP2 co-treatment. This inhibitory effect of BTP2 was especially apparent at day 5, as here no difference was visible between BTP2 only and BPT2 and AT-treated hECT (Fig. 36).

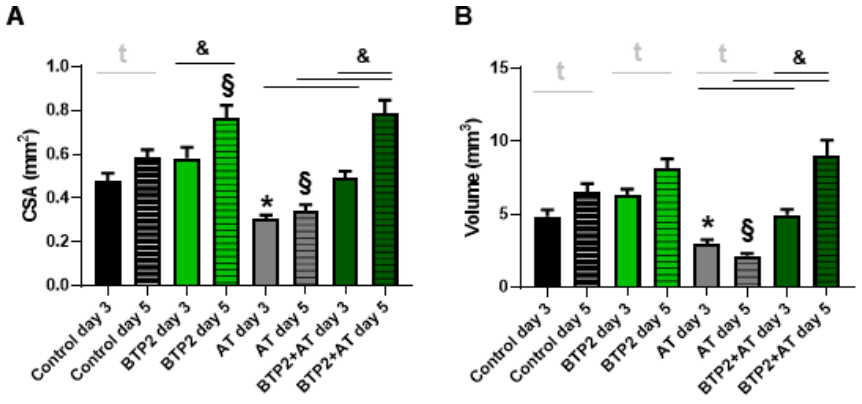

Figure 36: Effect of BTP2 on the compaction of hECT in fibrotic conditions.

hECT were generated from NHCF-V and collagen type I and treated with 10 µM BTP2 in the absence or presence of AT for 3 or 5 days. Then, the macroscopic images of hECT were taken to determine the cross-sectional area (CSA) ***(A)*** *and volumes* ***(B)*** *of the tissues. The values are given as means+SEM with 19-25 hECT per group, *p<0.05 vs. Control day 3, §p<0.05 vs. Control day 5, $^{&}$p<0.05 as*

assessed by one-way ANOVA with Tukey's multiple comparisons, $^{t}p<0.05$ as assessed by an unpaired t-test.

4.3.10 BTP2 reduced stiffness and increased extensibility of fibrotic model of hECT

The next aim was to investigate the interference of BTP2 with the pro-fibrotic mediator combination AT on the viscoelastic properties of the tissues. Therefore, rheometric measurements were performed after 3 or 5 days of tissue culturing. The Young's moduli were calculated from tissues' stress-strain relationship to assess the effect of BTP2 on stiffness. Strikingly, the AT dependent increase in stiffness, which was also demonstrated above, was completely abolished by BTP2 at both days. Otherwise, no significant BTP2 effect could be observed (Fig. 37).

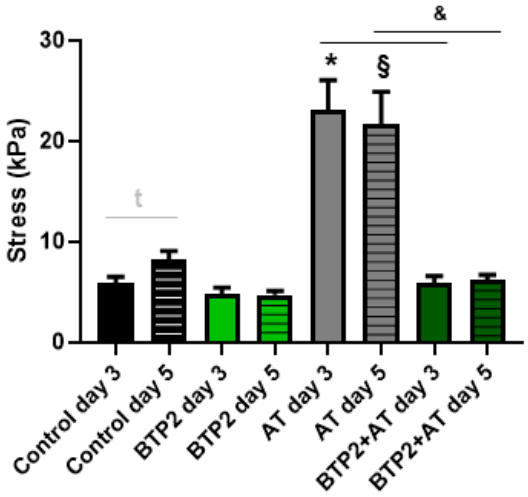

Figure 37: Effect of BTP2 on the stiffness of hECT in fibrotic conditions.

*hECT were generated with NHCF-V and collagen type I and treated with 10 µM BTP2 in the absence or presence of AT for 3 or 5 days. Rheometry was performed for stress-strain measurements to calculate the Young's moduli from the slope of linear region depicting the stiffness of the tissue. The values are given as means+SEM with 17-20 hECT per group, *p<0.05 vs. Control day 3, $^{§}p<0.05$ vs. Control day 5, $^{&}p<0.05$ as assessed by one-way ANOVA with Tukey's multiple comparisons, $^{t}p<0.05$ as assessed by an unpaired t-test.*

As the BTP2 treatment hampered the AT-induced stiffness of hECT, next its influence on other parameters determining the elastic region were investigated, including the yield point strain and stress, and the resilience. Similar as shown before, the yield point strain was lower at day 5 compared to day 3 in all conditions, showing a significant decline for control-, BTP2- and AT-treated hECT. In addition, at day 3, the application of BTP2 increased the yield point strain in the absence and presence of AT compared to control and AT, respectively. At day 5, a BTP2-dependent increase was apparent, but not significant (Fig. 38A). In contrast, the yield point stress seemed oppositely regulated in the presence of AT, as BTP2 pre-treatment resulted in a non-significant decline of the stress values at both days (Fig. 38B). Finally, the above-described general reduction in hECT resilience between day 3 and day 5 could be verified for all conditions and BTP2 was found to enhance the resilience of the tissues in the presence of AT (Fig. 38C).

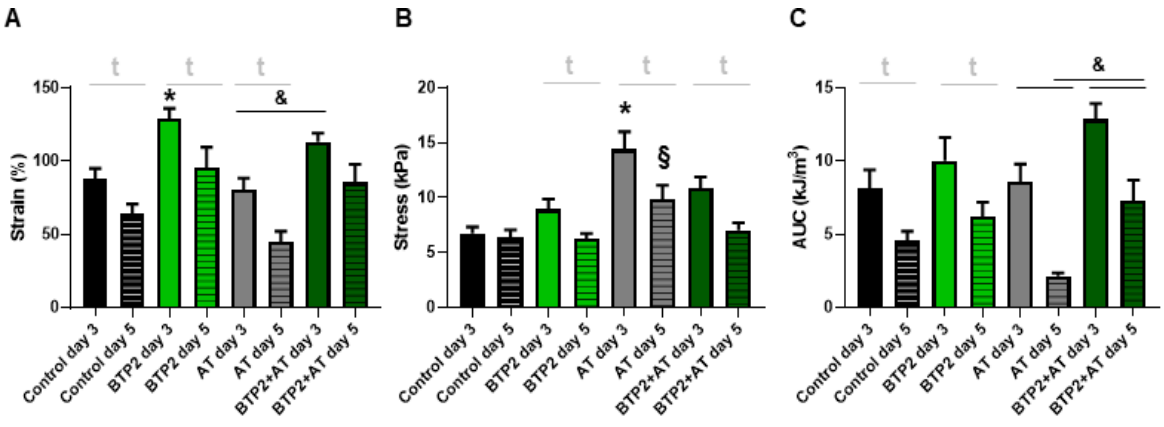

Figure 38: Effect of BTP2 on the yield point and the resilience of hECT in fibrotic conditions.

*The yield point was determined in the stress-strain curves and the strain **(A)** and stress **(B)** values are given. The energy absorbed as resilience was calculated from area under the curve of elastic phase **(C)**. Given are the values as means+SEM with 14-23 hECT per group, *p<0.05 vs. Control day 3, §p<0.05 vs.*

Control day 5, [&]p<0.05 as assessed by one-way ANOVA with Tukey's multiple comparisons, [t]p<0.05 as assessed by an unpaired t-test.

Next, the influence of BTP2 on the ultimate strength and strain, as well as the toughness was evaluated. It was found that the AT-dependent increase in ultimate strength was by trend decreased with BTP2 at day 3 and day 5 (Fig. 39A). The ultimate strain was increased with BTP2 compared to control at day 3 and by trend at day 5. The AT-mediated reduction of the ultimate strain was reversed by pre-treatment with BTP2 at both days. As mentioned before, the strain values from each treatment group were smaller at day 5 compared to day 3 (Fig. 39B). This was also true for the toughness values. BTP2 application was otherwise without effect (Fig. 39C).

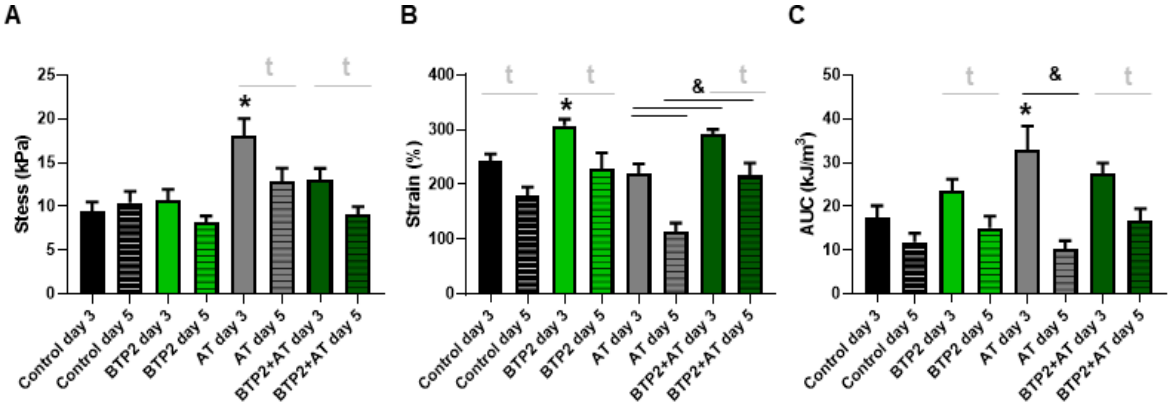

Figure 39: Effect of BTP2 on the strength and the extensibility of hECT in fibrotic conditions.

*The ultimate strength **(A)**, the ultimate strain **(B)** and the toughness (total absorbed energy) **(C)** were determined based on the stress-strain analysis. The values are given as means+SEM of 16-23 tissues per group, *p<0.05 vs. Control day 3, [§]p<0.05 vs. Control day 5, [&]p<0.05 as assessed by one-way ANOVA with Tukey's multiple comparisons, [t]p<0.05 as assessed by an unpaired t-test.*

4.3.11 BTP2 reduced cell number at early time point of hECT culturing

In 2D cultures of NHCF-V, BTP2 showed anti-proliferative and pro-apoptotic/-necrotic effects, therefore, its influence on the viability of the 3D cultured cells was studied in the following. As described before, a decline in cell numbers were found between day 3 and 5 under basal conditions and in the presence of AT. The BTP2 treatment resulted in a reduction of re-isolated viable cells at day 3, but not at day 5 compared to control and AT (Fig. 40).

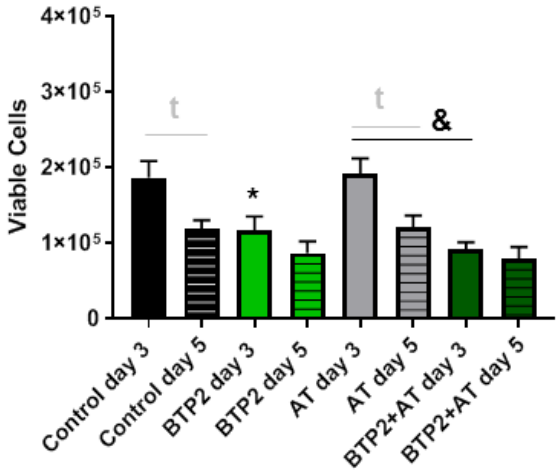

Figure 40: Effect of BTP2 on the cell number of hECT in basal and fibrotic conditions.

*hECT were cultured with 10 µM BTP in the absence or presence of AT for 3 or 5 days. The cells were re-isolated from individual tissues with collagenase/Accutase matrix digestion and then viable cells were counted by electronic current exclusion. The given values are means+SEM of four independent experiments with 11-12 hECT digested for each group, *p<0.05 vs. Control day 3, $^{\&}$p<0.05 as assessed by one-way ANOVA with Tukey's multiple comparisons, ^{t}p<0.05 as assessed by an unpaired t-test.*

4.3.12 SOCE inhibitor BTP2 influenced the cell-cycle activity at the later time point of hECT culturing

The influence of BTP2 on the status of cell cycle was assessed in the same manner as described above for the fibrotic treatments. As shown before, in G_0/G1-phase a moderate increase was noted under basal control between day 3 and day 5. BTP2 alone did not show this time-dependent effect. In contrast, when BTP2 was applied together with AT, a decline in the percentage of cells in G_0/G1-phase could be observed between day3 and day 5. Moreover, the percentage of G_0/G1-phase cells declined by BTP2 treatment in fibrotic conditions at day 5. The percentages of S-phase G2/M-phase cells followed an opposite pattern (Fig. 41).

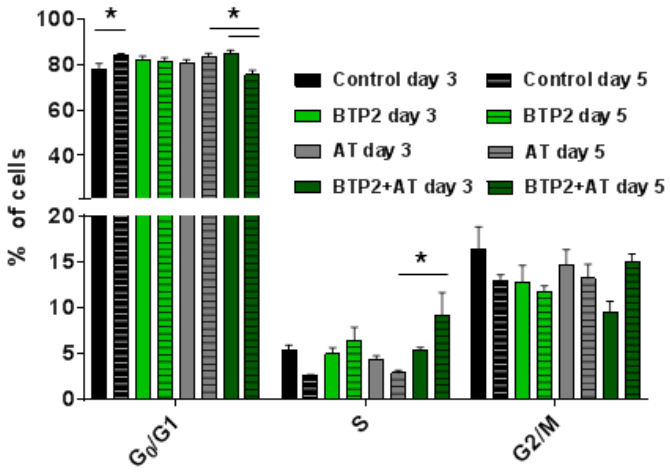

Figure 41: Effect of BTP2 on the cell-cycle activity of NHCF-V in hECT.

*The hECT were treated with 10 µM BTP2 in the absence or presence of AT for 3 or 5 days. The cells were re-isolated from individual hECT by a collagenase/Accutase digest and then fixed and stained with Hoechst 33342 for flow cytometry analysis. The percentages of cells in the G1-, S-, and G2/M-phase of the cell cycle are given. The given values are means+SEM of 5-7 hECT digested in each group. *p<0.05 as assessed by two-way ANOVA with Tukey's multiple comparisons.*

4.3.13 BTP2 down-regulated fibrotic markers at the mRNA level

The expression analysis in 2D cultures have shown that 10 µM BTP2 downregulates fibrotic markers. Therefore, the effect of BTP2 on fibrosis-associated genes like COL1A1, CCN1 and CTGF were studied by RT-qPCR in hECT. By this it could be shown that BTP2 treatment reduced the COL1A1 transcript levels in the presence of AT at day 3 and day 5 (Fig. 42A). However, no effect on the gene transcription of CTGF was found and only after 5 days in culture a reduction was detected for CCN1 (Fig. 42B, 42C).

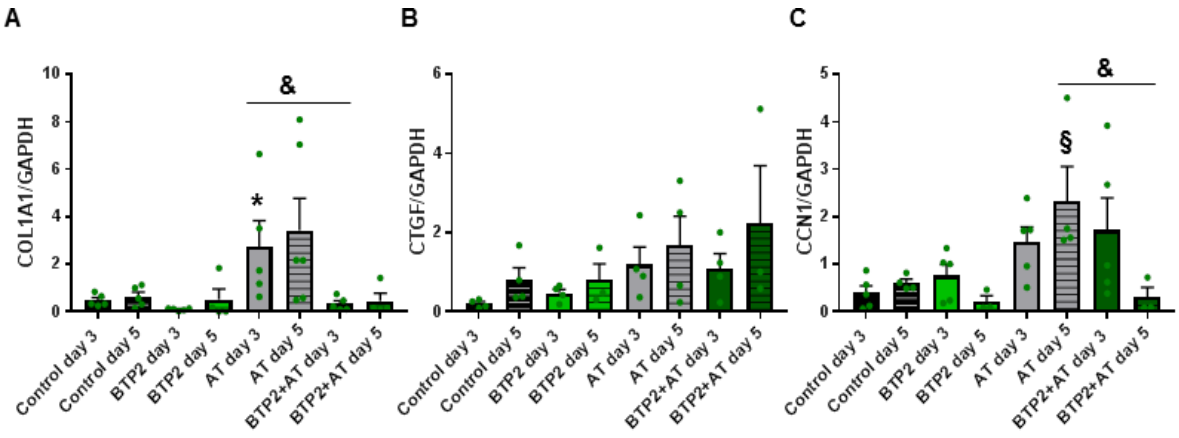

Figure 42: Effect of BTP2 on the fibrotic gene markers of hECT in fibrotic conditions.

hECT were cultured with 10 µM BTP2 in the absence or presence of AT for 3 or 5 days. The transcriptional changes in fibrotic gene markers were assessed by RT-qPCR. The quantification of transcripts of COL1A1 ***(A)****, CTGF* ***(B)*** *and CCN1* ***(C)*** *normalized by GAPDH are given as means+SEM of 3-6 independent experiments with three technical replicates each. A minimum of three hECT were pooled/grouped in each experiment, *p<0.05 vs. Control day 3, §p<0.05 vs. Control day 5, $^{&}$p<0.05 as assessed by one-way ANOVA with Tukey's post hoc analysis.*

4.3.14 BTP2 up-regulated ER-stress markers at the mRNA level

In 2D cultures of NHCF-V, treatment with BTP2 up-regulated ER-stress markers genes. Therefore, the influence of BTP2 on ER-stress genes markers was

examined in hECT by RT-qPCR. The transcriptional changes of HSPA5 revealed that only a moderate increase could be noted with BTP2 in fibrotic conditions at both days (Fig. 43A). The transcripts of DDIT3 showed significant up-regulation upon BTP2 treatment at day 3 and a non-significant increase at day 5 (Fig. 43B).

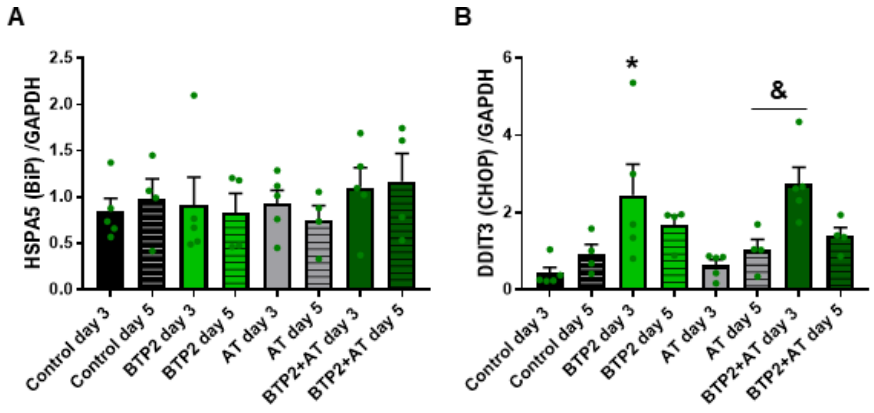

Figure 43: Influence of BTP2 on ER-stress regulating genes of hECT in fibrotic conditions.

hECT were cultured with 10 µM BTP2 in the absence or presence of AT for 3 or 5 days. The transcriptional changes in ER-stress marker genes were assessed by RT-qPCR. The quantification of transcripts of HSPA5 (BiP) ***(A)*** *and DDIT3 (CHOP)* ***(B)*** *normalized by GAPDH are given as means+SEM of 4-5 independent experiments with three technical replicates each. A minimum of three hECT were pooled/grouped in each experiment, *p<0.05 vs. Control day 3, $^{\&}$p<0.05 as assessed by one-way ANOVA with Tukey's multiple comparisons.*

4.4 Influence of the TRPC3 inhibition on the fibrotic remodeling of hECT

4.4.1 TRPC3 inhibition reduced the AT-mediated contraction, but had no effect on hECT compaction

Given that, in 2D cultures of NHCF-V, Pyr3 treatment has shown inhibitory effects on the Ca^{2+} handling and anti-proliferative and pro-apoptotic/-necrotic effects, we next investigated its effects in 3D cultures of hECT. To this end, NHCF-V

embedded in a collagen matrix were treated with 3 µM Pyr3 in the absence or presence of AT for 5 days. The influence of Pyr3 on hECT contraction was assessed first, which demonstrated that, under basal conditions and in the presence of Pyr3, tissue was around 22% after 5 days in culture. As shown before, AT treatment significantly increased hECT contraction. This increase was suppressed by Pyr3 pre-treatment (Fig. 44A). Next, the compaction of hECT was assessed by CSA and volume measurements, which revealed that both parameters were only slightly reduced by AT and Pyr3 had no effect in any condition (Fig. 44B, 44C).

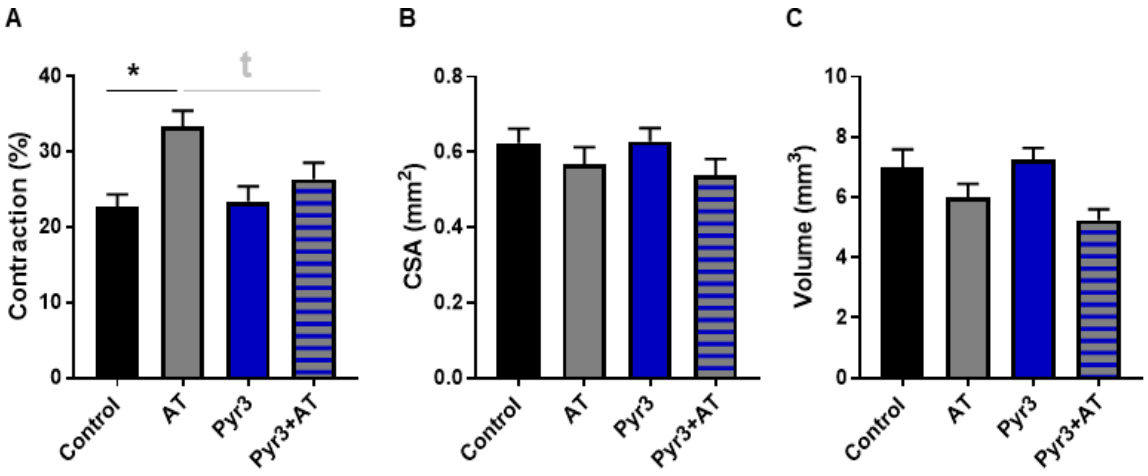

Figure 44: Influence of Pyr3 on hECT contraction and compaction in fibrotic condition.

hECT were generated from NHCF-V and collagen type I and treated with 3 µM Pyr3 in the absence or presence of 100 nM Ang II and 5 ng/ml TGF-β (AT) for 5 days. The deflection of the flexible tissue-holding poles was analyzed after casting (day 0) and at the end of treatment (day 5) to determine tissue contraction ***(A)****. The changes in percent compared to day 0 are given as means+SEM of 39-67 hECT per group, *p<0.05 as assessed by one-way ANOVA with Tukey's multiple comparisons, ^{t}p<0.05 as assessed by an unpaired t-test. Macroscopic images of the hECT were taken at day 5 to determine the cross-sectional areas (CSA)* ***(B)***

*and volumes **(C)** of the tissues. The values are given as means+SEM with 15-19 hECT per group.*

4.4.2 TRPC3 inhibition moderately influenced biomechanical properties of hECT in fibrotic condition

Next, the influence of TRPC3 inhibition by Pyr3 on the viscoelastic properties of hECT was investigated after 5 days of culture under the pro-fibrotic mediator combination AT. Rheometric measurements were performed and the obtained stress-strain curves were analyzed to calculate the Young's moduli depicting tissues' stiffness. As shown before, AT significantly induced the hECT stiffness. Pyr3 alone was without effect and in the presence of AT hECT stiffening was reduced to control conditions (Fig. 45).

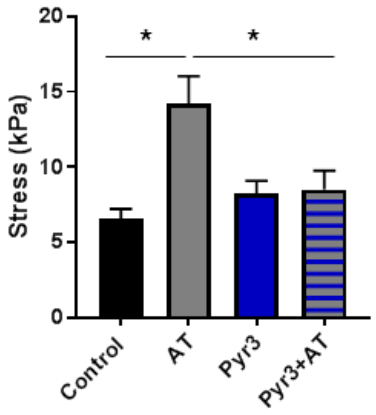

Figure 45: Influence of Pyr3 on the stiffness of hECT in fibrotic condition.

*hECT were generated from NHCF-V and collagen type I and treated with 3 µM Pyr3 in the absence or presence of AT for 5 days. Rheometry was performed and the obtained stress-strain curves were used to determine the Young's moduli as stiffness. The values are depicted as means+SEM with 11-17 hECT per group, *p<0.05 as assessed by one-way ANOVA with Tukey's multiple comparisons.*

Next, the interference of Pyr3 with other parameters of the elastic phase was assessed, including the yield point strain and stress, and the resilience. The yield

point strain was moderately reduced with AT in the absence or presence of Pyr3 (Fig. 46A), whereas the yield point stress was not affected by the treatments (Fig. 46B). The resilience showed also no significant differences (Fig. 46C).

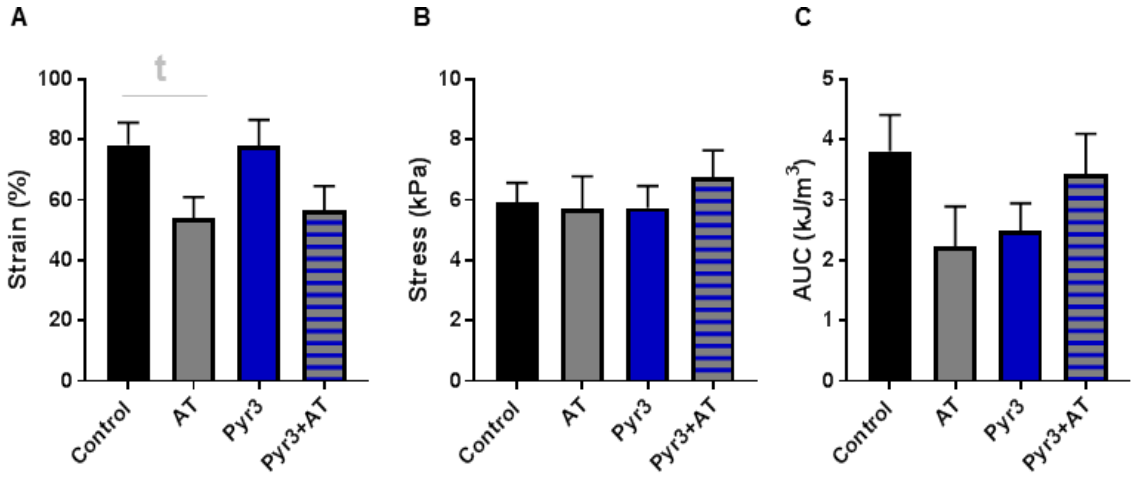

Figure 46: Influence of TRPC3 inhibition on the yield point and the resilience of hECT in fibrotic condition.

*The yield point was determined in the stress-strain curves and the strain **(A)** and stress **(B)** values are given. The resilience was calculated as area under the curve of the elastic phase **(C)**. Given are the values as means+SEM with 10-17 hECT per group, $^{t}p<0.05$ as assessed by an unpaired t-test.*

The next phase of stress-strain curve, i.e. plastic phase, was evaluated by characteristic parameters including the ultimate strength, strain and the toughness. Here, no significant change could be observed in any parameter or condition (Fig. 47).

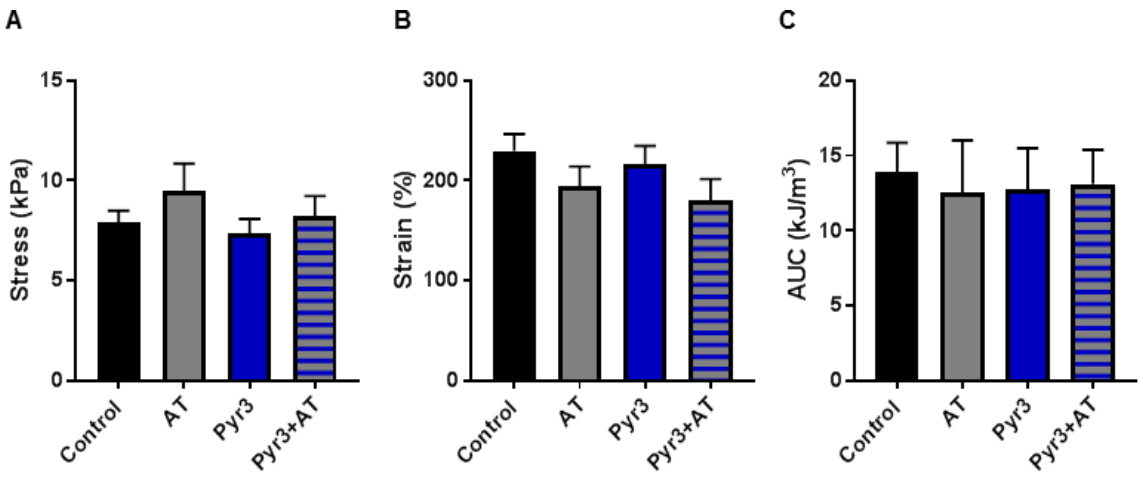

Figure 47: Influence of Pyr3 on the strength and the extensibility of hECT in fibrotic condition.

*The ultimate strength **(A)**, the ultimate strain **(B)** and the toughness **(C)** were determined based on the stress-strain analysis. The values are given as means+SEM of 13-18 tissues per group.*

4.4.3 TRPC3 inhibition had no influence on the cell number in hECT

In 2D cultures of NHCF-V, Pyr3 showed necrotic/apoptotic potential, therefore, its effect on cell viability in 3D cultures was studied by collagenase and Accutase digestion of hECT. Counting of the number of re-isolated viable cells demonstrated that none of the treatments showed a noticeable effect on the cell number after 5 days of culturing (Fig. 48).

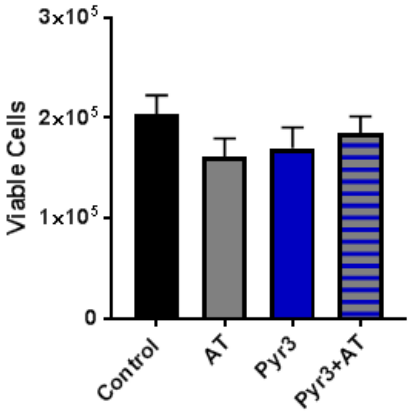

Figure 48: Influence of TRPC3 inhibition on the cell number in hECT in fibrotic condition.

The hECT were cultured with 3 µM Pyr3 in the absence or presence of AT for 5 days. The cells were re-isolated from individual hECT by a collagenase/Accutase digest and the viable cells were counted. The given values are means+SEM of 6-7 hECT digested in each group.

5. Discussion

Despite rigorous efforts to elucidate the pathophysiological mechanisms underlying fibrotic processes, cardiac fibrosis remained the ultimate fate for almost every heart disease. Although several cell types are involved in the pathogenesis of cardiac fibrosis, CF are the principle regulators of ECM remodeling, as they secret a number of growth factors and cytokines during the course of fibrosis development. In addition to this, Ca^{2+} influx has also been shown to enhanced in CF isolated from HF patients [113] and in response to pro-fibrotic factors [65]. However, the mechanisms of Ca^{2+}-influx-dependent regulation of ECM proteins are still not clear. In this work, we provide insight to the involvement of Ca^{2+}-influx mechanisms in the basal and receptor-agonist-dependent Ca^{2+} handling in NHCF. We further showed that Ca^{2+} influx-inhibition-induced ER stress interfere with the synthesis of fibrosis-associated proteins. Then, the impact of Ca^{2+}-influx mechanisms was investigated in a fibrotic 3D construct of hECT. Here, we observed that pro-fibrotic mediators successfully induced fibrotic features in the 3D construct and Ca^{2+}-influx inhibition downregulates fibrotic parameters of the hECT model. Mechanistically, Ca^{2+}-influx inhibition triggered ER stress which suppressed pro-fibrotic gene markers and thus reversed fibrotic biomechanical parameters of the hECT.

5.1 Interference of Ca^{2+}-influx mechanisms with Ca^{2+} transient in NHCF-V

Ca^{2+} regulation has been extensively studied in cardiomyocytes, but it is not well characterized in CF. In this thesis, one of the aims was to study the role of Ca^{2+}-influx mechanisms in the regulation of the behavior of CF. Therefore, in a first approach, the influence of the SOCE inhibitor BTP2 and the TRPC3 inhibitor Pyr3 on the oscillation of Ca^{2+} and on the receptor agonist-induced Ca^{2+} transients were

studied. There data demonstrated that both inhibitors efficiently reduced the basal and receptor-induced Ca^{2+} oscillations in CF and thus confirmed the already described involvement of SOCE and TRPC3 in this process [104, 106, 139, 189]. Both inhibitors also affected the Ang II-induced calcium transients in CF. Main effects were reductions of the transient amplitudes and post-transient resting Ca^{2+} signals. A similar effect was seen for BTP2 when TGF-β instead of Ang II was applied to the cells. A transient increase in calcium in response to Ang II in CF has been described several times before [63, 65, 105, 190], whereas a TGF-β-induced transient in CF was not reported before. The effect of an acute application of TGF-β on the calcium regulation seems dependent on the cell type. It ranges from a slow constant increase in calcium with or without a slow decay phase to an induction of calcium oscillations. Potential involvements of the IP3 receptors, TRPC1, and NCX1 were discussed [191-194].

The data obtained in this study suggest that the SOCE is also involved in the TGF-β-dependent calcium regulation as the highest concentration of BTP2, strongly diminishing the transient amplitude and markedly lowering the post-transient resting calcium. The observed effects were similar compared to when Ang II was used as an agonist and in line with effects shown for other SOCE inhibitors in CF [61, 65]. Pyr3, which was only tested with Ang II, showed similar, but not so pronounced effects as BTP2. There data indicate that both TRPC3 and SOCE are involved in the calcium influx in cells, however, a recent publication raised substantial doubts about an involvement of TRPC3 in this process. In mouse cardiac fibroblasts it was demonstrated that a knockout of all seven TRPC channels did not impair the Ang II-dependent calcium transient, suggesting that

TRPC channels do not play any role in this setting. This is sharply in contrast to what has been suggested before in studies using Pyr3, however, former studies were using CF from rat hearts [70, 195]. Whether species differences, culture conditions or other factors could account for the observed discrepant data is completely unclear and argues for a better phenotype control of the CF in such studies.

A further possible explanation for these findings is related to the specificity of Pyr3. It was shown that Pyr3 inhibits equally well ROCE and SOCE [196]. The idea that the observed Pyr3 effects in CF are dependent on its unspecific inhibition of SOCE is supported by the before-mentioned study, which demonstrated not only that all seven TRPC channels are dispensable for the Ang II response, but also that SOCE inhibition clearly reduced the calcium transient [65]. Moreover, a direct comparison of Pyr3 with BTP2 showed that BTP2 is not only more potent in SOCE inhibition but also more efficient, which could explain the stronger BTP2 effect observed in this thesis. Nevertheless, it is important to mention that BTP2 is also not specific for SOCE inhibitor but showed substantial ROCE inhibitory activity by influencing the calcium influx via TRPC3, TRPC6, and TRPC7 [196, 197]. Therefore, future studies are needed in which a knockout/knockdown of TRPC3 and the Orai channel will be performed side-by-side.

5.2 Influence of SOCE and TRPC3 inhibition on NHCF-V proliferation and apoptosis

Regardless of the type of cardiac injury, the induction of CF proliferation is a common feature of the initial fibrotic response [48, 198-204]. Therefore, we investigated the effect of Ca^{2+}-influx inhibition on CF proliferation in 2D cultures,

which showed that both BTP2 and Pyr3 significantly reduced proliferation and enhanced the death rates of NHCF-V. The anti-proliferative and cytotoxic effects of Pyr3 has been shown before for CF and other fibroblasts [70, 195, 205] and BTP2 was found to inhibit the proliferation of smooth muscle cells, breast cancer cells, and breast cancer-derived endothelial colony-forming cells [206-209]. In these studies, the used concentrations were all in the lower micromolar range and thus in line with the observations in this thesis. However, as mentioned above, both inhibitors interfere with ROCE and SOCE, therefore, it is not clear which of both mechanisms might contribute more pronouncedly to the anti-proliferative and cytotoxic effect. In a more targeted approach it was shown that the knockdown of Orai inhibited the proliferation of different cancer cells and decreased cell viability [210, 211]. Moreover, Orai channels were demonstrated to be necessary for the G1-to-S-phase transition in the cell cycle supporting the important role of SOCE in cell proliferation [212]. But likewise, it was also shown that a TRPC3 knockdown inhibits proliferation of e.g. myoblast and mesangial cell [213, 214]. Similar as suggested for the contribution of SOCE and TRPC3 in calcium entry, a comparative analysis for their role in CF proliferation is necessary.

Finally, we also observed that a pro-fibrotic treatment with Ang II moderately enhanced the apoptosis of the NHCF-V, but no further increase was observed by the co-treatment with the Ca^{2+}-influx inhibitors. In agreement with this observation, it was shown that the AT_1R-induced apoptosis in CF is dependent on the Ca^{2+} influx from the extracellular space [215]. This finding indicates that the fine-tuning of the upper and lower intracellular calcium levels is of utmost importance for cell viability.

5.3 Regulation of fibrosis-associated markers by SOCE inhibitor BTP2

Besides the role of the calcium entry in cell proliferation, we investigated its influence on the regulation of fibrosis-associated factors. We found that the highest concentration of BTP2 strongly reduced the mRNA and protein levels of COL1A1/Pro-Col1a1 and CTGF. This effect was independent of the co-treatment with pro-fibrotic factors, which indicated that the expression blockade could not only result from an inhibition of a certain fibrotic pathway as it was suggest before with the SOCE inhibitor SKF96365 in adult rat cardiac fibroblasts [61]. Moreover, by investigating the ratio of the secreted and cytosolic protein amounts, it became clear that in BTP2-treated cells more protein is proportionally secreted as in control conditions.

This could be on one hand explained by an accumulation of secreted proteins, but also by a disturbance in the trafficking of these factors. This observation prompted the following investigation of factors involved in ER stress. On RNA level, the expression of HSPA5 (encoding for BiP) and DDIT3 (encoding for CHOP) were analyzed and found to be strongly up-regulated in all conditions with 10 µM of BTP2. BiP was also up-regulated on protein level, however, to a lesser extent. Additionally, the expression of PERK was studied, but no changes were found. The more relevant detection of phosphorylated PERK (P-PERK) did unfortunately fail due to the quality of the used antibody and also CHOP could not be detected on protein level.

Especially, difficulties in the detection of P-PERK seems to be a general problem [216]. To further verify that the induction of ER stress can have an impact on the

expression of COL1A1 and CTGF, the NHCF-V were treated with the SERCA pump inhibitor thapsigargin (TG), a commonly used inducer of ER stress [153-156]. This treatment resulted in a similar strong suppression of Pro-Col1a1 and CTGF expression as seen with BTP2. These data suggested that BTP2 exerts its effect on fibrotic gene expression by an induction of ER stress in 2D cultured NHCF-V, most likely via the detected reduction in the ER calcium load. In line, negative interference with SOCE was shown to result in an induction of the UPR and ER stress in different cells [157-162] and ER stress has been shown before to inhibit collagen synthesis [217]. However, there are also opposing data showing that TG-induced ER stress can result in an accumulation of intracellular procollagen in cultured CF [218]. The reason for this discrepancy is unclear and needs further investigation. Surprisingly, Pyr3 treatment had no effect on Pro-Col1a1 expression in NHCF-V. A possible explanation could be the above-mentioned lower potency and efficacy in SOCE inhibition [196].

5.4 Characterization of *in vitro* fibrotic model of hECT

To date, the absence of any effective treatment for cardiac fibrosis highlights the gap of knowledge on the involved fibrotic mechanisms. Most of the work elucidating responsible mechanisms in this context is based on *in vivo* animal models and *in vitro* 2D culturing of CF. Although animal models were proven to be useful, e.g. to provide information on the origin of myofibroblasts, dissecting endo-, para-, and autocrine mechanisms is more than difficult. 2D culturing of CF, in contrast, is highly artificial and brings the problem of the rapid transdifferentiation of CF into MyoF, because of the unnatural high stiffness of culture plates (10^6 kPa), the missing 3D environment and the rich medium compositions [219, 220].

To overcome such experimental problems, 3D-engineered tissue models of CF mostly in the form of a disc or sheet have been used to investigate fibrotic mechanisms in a more physiological environment than in 2D cultures. These tissue shapes, however, limit the measurements of functional parameters including the biomechanics of the tissues [184, 185]. Therefore, we used in this study ring-shaped hECT, which offer a simple and convenient way to study effects of different pro-fibrotic mediators and anti-fibrotic interventions in a controlled way.

In a first step, hECT were treated with Ang II, TGF-β or a combination of both factors to induce pro-fibrotic processes. Initial readouts included hECT compaction and contraction. We were able to show that hECT compaction and contraction, given by the reduction in the CSA and the tissue length, respectively, were largely enhanced by TGF-β. This is line with other publications, which have already demonstrated that TGF-β induces a strong pro-contractile effect on engineered fibroblasts tissues [185, 221-223]. In contrast, Ang II treatment was sufficient to increase the lateral hECT compaction, but not the longitudinal hECT contraction. The missing effect of Ang II on tissue contraction was surprising as it is one of the most commonly used pro-fibrotic factors, inducing CF activation *in vitro* and cardiac fibrosis *in vivo* [61, 224]. A plausible explanation for this finding is that the increase in the cellular traction force in response to Ang II was not high enough to exceed the passive force given by the bending stiffness of the poles, but sufficient for further lateral compaction. Both, compaction and contraction are actin-dependent processes, however, compaction needs lower traction forces than contraction and occurs independent of contraction. In fact, compaction seems to be a prerequisite for longitudinal contraction [221, 225].

In addition, technical difficulties might have added to the observed weak Ang II effects, as it was shown that Ang II can be rapidly metabolized in *in vitro* conditions. In neuronal cell cultures, exogenously applied Ang II remained elevated for only 30 min and declined to baseline levels already 3 h after application [226]. Whether this Ang II metabolism also occurs in CF cultures is not clear, but it was shown that the main metabolizing enzyme, the angiotensin-converting enzyme 2 (ACE2), is expressed and functional active in MyoF cultures [227]. To prevent an inefficient treatment with Ang II, it could be more frequently added than every second day as performed in this thesis. Moreover, using an additional ACE2 inhibitor could also serve to increase the efficacy of Ang II [228].

However, in line with other data it can be expected that even with an optimized Ang II treatment, the induced effects on tissue contraction would be not as strong as with TGF-β [229]. How much force a cell can exert to the matrix predominantly depends on the expression pattern of the different actin isoforms. Especially high levels of the contractile SMA proteins are necessary for maximum contraction. In this context, there are data suggesting that Ang II might be less effective in SMA induction than TGF-β [54, 230]. Finally, the addition of Ang II to TGF-β resulted in no further increase in hECT compaction and a very minor additional increase in tissue contraction, indicating that TGF-β signaling dominates the regulation of the pro-contractile function of the embedded cells.

In the next step, the biomechanical properties of the hECT were assessed by rheometry with subsequent stress-strain analysis. Similar to the contractile response, it could be shown that the stiffening effect of TGF-β was more pronounced than of Ang II. The combination of both factors further increased tissue

stiffness, although the differences were not significant due to the high data variance. This enhanced hECT stiffness was especially visible at day 3, which was interestingly the only time point when Ang II addition resulted in a significant increase in the TGF-β-mediated longitudinal contraction. Tissue stiffening is dependent on a two-step process. Firstly, the cells compact and contract the matrix, and secondly, the condensed matrix is stabilized e.g. by collagen storage and cross-linking. Several studies have shown that in the end, the matrix is the major determinant for the stiffness of the tissue [221, 231, 232]. In line with this mechanism and published data, exposure to TGF-β enhanced not only the hECT contraction, but also increased the expression of COL1A1, explaining the enhanced stiffness [181, 221, 233]. Ang II, in contrast, had only minor effects, none of them significant, and therefore its effect of hECT stiffness was likewise marginal. The interesting question in this context is how both fibrotic factors could result in the highest tissue stiffness. Differences in COL1A1 expression between TGF-β and AT were not detected, therefore, the enhanced contraction might have led to the observed effect.

However, other contributors must be taken into consideration and studied in the future. This includes e.g. lysyl oxidase, which is the main collagen cross-linking enzyme. Its role in tissue stiffening, in the presence and absence of TGF-β, has been demonstrated in different publications [181, 221, 233]. Independent on how the pro-fibrotic factors elicited their effects on the hECT stiffness, it is important to mention that the detected stiffness of control and AT-treated tissues, with around 8 kPa and 22 kPa, respectively, resemble the stiffnesses of the healthy and fibrotic heart [220, 234, 235].

In addition to hECT stiffness, the stress at the yield point and the ultimate strength were determined. In contrast to the tissue stiffness, these parameters did not show a gradual increase with Ang II, TGF-β and AT. Instead, they were moderately enhanced at day 3 and lowered at day 5. This loss in tissue strength can be mainly explained by a decline in strain resistance, as shown by the yield point and failure point strains. In other words, a reduction in tissue elasticity and extensibility consequently results in diminished tissue strength. This is supported by the resilience and toughness data demonstrating that the energy absorption is lower at day 5 compared to day 3. So far, it is not clear what could have caused the enhanced strain susceptibility between day 3 and day 5. Interestingly, the cell number declined in the same period of time in all conditions. Although it was shown that the strain resistance in connective tissues is largely dependent on the matrix component [236, 237], the death of cells could contribute to tissue instability. In line, it was shown that decellularization of arteries significantly reduced the ultimate strain, but not the Young's modulus similar as seen in the hECT model [238].

To further investigate the effect of the pro-fibrotic factors on the cells, a cell-cycle analysis was performed. However, none of the pro-fibrotic treatments had an influence. In contrast, in all conditions a trend for a decline in cell-cycle activity between day 3 and day 5 was visible. This decline most likely results from a progressive loss in cell-cycle activity due to the embedment of formerly 2D cultured cells, being highly proliferative, into a 3D matrix. Such an inhibitory effect on the cell-cycle activity was already demonstrated before for the rat ECT model and other 3D collagen-based tissue constructs [181, 239]. It seemed surprising that TGF-β did not induce the cell-cycle activity in hECT, however, the data on the role

of TGF-β in CF proliferation are not clear. While some studies were able to show a pro-proliferative effect of TGF-β in 2D and 3D cultures, others were not [223, 240, 241]. The effect of TGF-β might be largely dependent on the phenotypic state of the cells, which in this thesis was myofibroblastic, as well as on the collagen and cell density [219].

Taken together, the obtained data clearly demonstrate that TGF-β induces fibrotic features in the hECT model, whereas Ang II was not able to generate a full fibrotic response. The combination of both factors resulted for some parameters in an enhanced effect and, therefore, the combination was used in the next step for studying the effects of the SOCE inhibitor BTP2 and the TRPC3 channel blocker Pyr3.

5.5 Effects of the SOCE inhibitor BTP2 and the TRPC3 channel blocker Pyr3 in the fibrotic model of hECT

Both, the SOCE- and TRPC3-dependent calcium influx have been shown to regulate pro-fibrotic mechanisms in CF *in vitro* and *in vivo* conditions [107, 113, 114, 190, 195]. However, to the best of our knowledge, the effect of SOCE and TRPC3 inhibition has not been studied yet in a fibrotic 3D CF model. Therefore, the hECT were generated in the presence of AT and BTP2 or Pyr3 and the first analyzed parameters were compaction and contraction.

Interestingly, BTP2 treatment gradually reduced the basal and AT-dependent increase of both of these parameters over time. As discussed above, the cell component of the tissue is largely responsible for tissue compaction and contraction. Based on the observed effect of BTP2 on the Ang II- and TGF-β-induced calcium transients in 2D cultured cells, its inhibitory action on the calcium

influx might, at least in part, account for this observation. In line, BTP2 was shown before to inhibit the formation of actin fibers as well as the agonist-induced contraction of 3D smooth muscle cell constructs [242, 243]. Importantly, BTP2 treatment resulted in a more pronounced loss of cells within the first 3 days compared to the other conditions, which probably added to the failure in compaction and contraction [184, 225, 236, 242, 244, 245]. In contrast to BTP2, Pyr3 reduced only hECT contraction, but not compaction and, surprisingly, it displayed no cytotoxic effect in hECT. This indicates that the effect of Pyr3 is largely dependent on the regulation of the actin cytoskeleton. In agreement, in 2016 it was shown that Pyr3 suppressed the TGF-β-induced expression of SMA in CF [107], which could clearly explain the inhibition in longitudinal tissue contraction. The difference between both substances could be also seen in the rheometric analysis. Although BTP2 and Pyr3 reduced both the AT-induced increase in hECT stiffness, only BTP2 had an influence on the strain values of the hECT. While the inhibitory effect of Pyr3 on the AT-dependent stiffening can be understood as a consequence of the reduced tissue contraction, the generalized effect of BTP2 is probably a consequence of several factors. First, the impaired compaction and contraction do not allow for forming cross-linked, dense, and stiff tissues. Second, the AT-dependent induction in COL1A1 expression was completely suppressed by BTP2 diminishing the amount of produced ECM. And third, the cell number declined faster in the presence of BTP2 during the initial culture phase. Altogether this resulted in hECT which were less stiff, but more elastic and extensible.

5.6 Effects of the SOCE inhibitor BTP2 on the expression of pro-fibrotic and UPR genes in the fibrotic model of hECT

In line with 2D-cultured NHCF-V, BTP2 treatment also significantly downregulated the expression of pro-fibrotic genes in hECT, including COL1A1 and CCN1. In contrast, expression of CTGF was not regulated in the 3D model. This indicated that the effects in the 3D model were less pronounced as in 2D, suggesting that the UPR activation by BTP2 in hECT might be less intense. Accordingly, BTP2 treatment moderately induced the expression of DDIT3 but not of HSPA5 in these tissues. A plausible explanation could be the phenotypic difference between the cells in 2D and 3D cultures. It has been shown that CF in 3D constructs phenotypically shift from myofibroblasts to less activated CF with reduced secretory activities (*unpublished data by our group and [180]*). The high secretory activity of myofibroblast is it, however, which makes these cells more susceptible to ER stress [41, 246]. Together, the pro-fibrotic and UPR gene expression data indicate that the BTP2-induced UPR might have interfered with fibrotic gene expression in hECT.

5.7 Conclusion

This study demonstrates that Ca^{2+}-influx inhibition with BTP2 interferes with the agonist-dependent and basal Ca^{2+} regulation in CF. This interference induces ER stress, most likely by the observed reduction of the ER Ca^{2+} content. As a consequence, an increase in cell death and a reduction in fibrotic gene expression were observed. The data further suggest that the effects of BTP2 are more pronounced in myofibroblasts than in the less activated CF. Therefore, these findings highlight the therapeutic potential of the UPR pathways in cardiac fibrosis. However, BTP2 interferes with a ubiquitous mechanism and is therefore most likely

not suitable as an anti-fibrotic drug. More specific approaches are required to interfere with the UPR specifically in the diseased myofibroblasts.

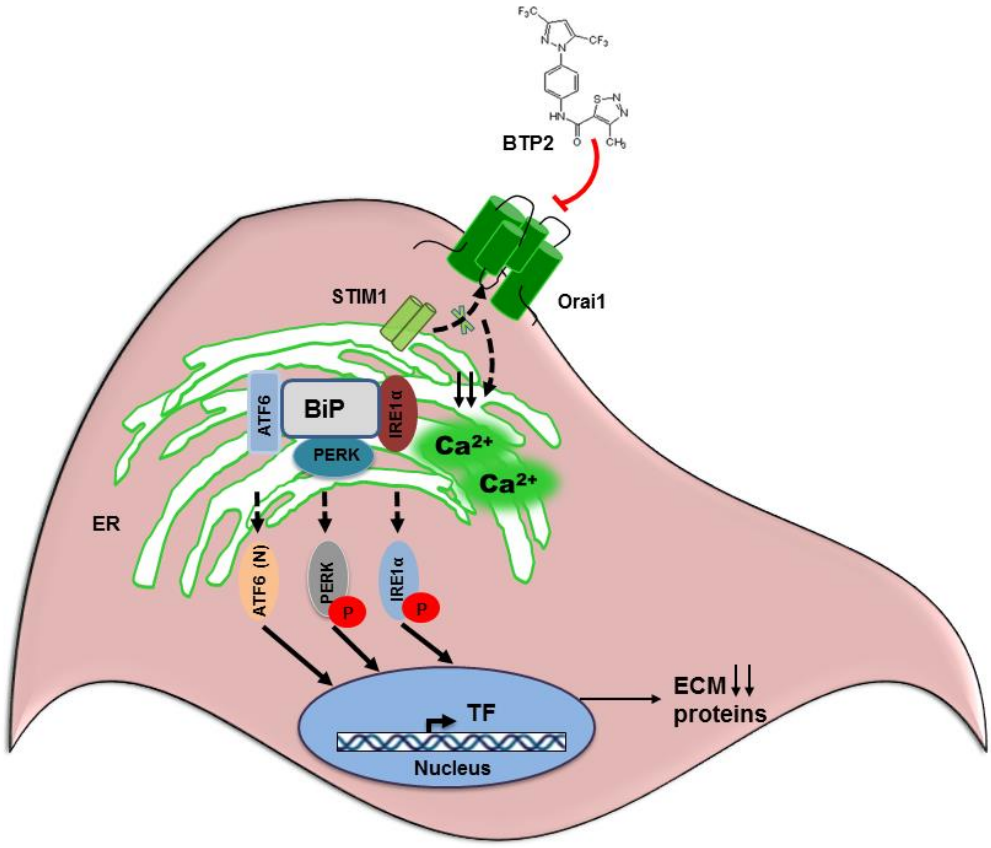

Figure 49: BTP2-induced depletion of ER Ca^{2+} results in ER stress.

SOCE inhibition with BTP2 induces ER Ca^{2+} release which ultimately leads to ER-stress. This results in release of BiP from IRE1α, PERK and ATF6 which translocate to the nucleus and downregulates the ECM proteins expression.

5.8 Outlook

The findings of this study suggest further investigations as follows:

- Generation of genetically encoded Ca^{2+} indicators to assess the Ca^{2+} regulation in different compartments of NHCF-V

- Investigation of SOCE-mediated Ca^{2+} influx in hECT to correlate the Ca^{2+} handling with fibrotic markers expression
- Genetic knockout or knockdown of UPR mediators to identify a specific anti-fibrotic target

6. BIBLIOGRAPHY

1. Savarese, G. and L.H. Lund, *Global Public Health Burden of Heart Failure.* Card Fail Rev, 2017. **3**(1): p. 7-11.
2. Wynn, T.A., *Cellular and molecular mechanisms of fibrosis.* J Pathol, 2008. **214**(2): p. 199-210.
3. Taylor, C.J., et al., *Survival following a diagnosis of heart failure in primary care.* Fam Pract, 2017. **34**(2): p. 161-168.
4. Gourdie, R.G., S. Dimmeler, and P. Kohl, *Novel therapeutic strategies targeting fibroblasts and fibrosis in heart disease.* Nat Rev Drug Discov, 2016. **15**(9): p. 620-638.
5. Shinde, A.V. and N.G. Frangogiannis, *Fibroblasts in myocardial infarction: a role in inflammation and repair.* J Mol Cell Cardiol, 2014. **70**: p. 74-82.
6. Gyöngyösi, M., et al., *Myocardial fibrosis: biomedical research from bench to bedside.* Eur J Heart Fail, 2017. **19**(2): p. 177-191.
7. Azevedo, C.F., et al., *Prognostic significance of myocardial fibrosis quantification by histopathology and magnetic resonance imaging in patients with severe aortic valve disease.* J Am Coll Cardiol, 2010. **56**(4): p. 278-87.
8. Aoki, T., et al., *Prognostic impact of myocardial interstitial fibrosis in non-ischemic heart failure. -Comparison between preserved and reduced ejection fraction heart failure.* Circ J, 2011. **75**(11): p. 2605-13.
9. Kong, P., P. Christia, and N.G. Frangogiannis, *The pathogenesis of cardiac fibrosis.* Cell Mol Life Sci, 2014. **71**(4): p. 549-74.
10. Weber, K.T., et al., *Regression of Established Cardiac Fibrosis in Hypertensive Heart Disease.* Am J Hypertens, 2017. **30**(11): p. 1049-1052.
11. McAloon, C.J., et al., *Characterisation of circulating biomarkers before and after cardiac resynchronisation therapy and their role in predicting CRT response: the COVERT-HF study.* Open Heart, 2018. **5**(2): p. e000899.
12. Shanbhag, S.M., et al., *Prevalence and prognosis of ischaemic and non-ischaemic myocardial fibrosis in older adults.* Eur Heart J, 2019. **40**(6): p. 529-538.

13. Baudino, T.A., et al., *Cardiac fibroblasts: friend or foe?* Am J Physiol Heart Circ Physiol, 2006. **291**(3): p. H1015-26.
14. Travers, J.G., et al., *Cardiac Fibrosis: The Fibroblast Awakens.* Circ Res, 2016. **118**(6): p. 1021-40.
15. Leask, A., *Potential therapeutic targets for cardiac fibrosis: TGFbeta, angiotensin, endothelin, CCN2, and PDGF, partners in fibroblast activation.* Circ Res, 2010. **106**(11): p. 1675-80.
16. Iwanaga, Y., et al., *Excessive activation of matrix metalloproteinases coincides with left ventricular remodeling during transition from hypertrophy to heart failure in hypertensive rats.* J Am Coll Cardiol, 2002. **39**(8): p. 1384-91.
17. Czubryt, M.P., *Common threads in cardiac fibrosis, infarct scar formation, and wound healing.* Fibrogenesis Tissue Repair, 2012. **5**(1): p. 19.
18. Talman, V. and H. Ruskoaho, *Cardiac fibrosis in myocardial infarction-from repair and remodeling to regeneration.* Cell Tissue Res, 2016. **365**(3): p. 563-81.
19. Westermann, D., et al., *Cardiac inflammation contributes to changes in the extracellular matrix in patients with heart failure and normal ejection fraction.* Circ Heart Fail, 2011. **4**(1): p. 44-52.
20. Russo, I., et al., *Protective Effects of Activated Myofibroblasts in the Pressure-Overloaded Myocardium Are Mediated Through Smad-Dependent Activation of a Matrix-Preserving Program.* Circ Res, 2019. **124**(8): p. 1214-1227.
21. Berk, B.C., K. Fujiwara, and S. Lehoux, *ECM remodeling in hypertensive heart disease.* J Clin Invest, 2007. **117**(3): p. 568-75.
22. Schelbert, E.B., et al., *Employing Extracellular Volume Cardiovascular Magnetic Resonance Measures of Myocardial Fibrosis to Foster Novel Therapeutics.* Circ Cardiovasc Imaging, 2017. **10**(6).
23. Beltrami, C.A., et al., *Structural basis of end-stage failure in ischemic cardiomyopathy in humans.* Circulation, 1994. **89**(1): p. 151-63.
24. Weber, K.T., et al., *Myocardial fibrosis: role of angiotensin II and aldosterone.* Basic Res Cardiol, 1993. **88 Suppl 1**: p. 107-24.

25. López, B., et al., *Myocardial Collagen Cross-Linking Is Associated With Heart Failure Hospitalization in Patients With Hypertensive Heart Failure.* J Am Coll Cardiol, 2016. **67**(3): p. 251-60.
26. Fan, D., et al., *Cardiac fibroblasts, fibrosis and extracellular matrix remodeling in heart disease.* Fibrogenesis Tissue Repair, 2012. **5**(1): p. 15.
27. Weber, K.T., et al., *Myofibroblast-mediated mechanisms of pathological remodelling of the heart.* Nat Rev Cardiol, 2013. **10**(1): p. 15-26.
28. Weber, K.T. and J.S. Janicki, *Angiotensin and the remodelling of the myocardium.* Br J Clin Pharmacol, 1989. **28 Suppl 2**(Suppl 2): p. 141S-149S; discussion 149S-150S.
29. Ivey, M.J. and M.D. Tallquist, *Defining the Cardiac Fibroblast.* Circ J, 2016. **80**(11): p. 2269-2276.
30. Porter, K.E. and N.A. Turner, *Cardiac fibroblasts: at the heart of myocardial remodeling.* Pharmacol Ther, 2009. **123**(2): p. 255-78.
31. Moore-Morris, T., et al., *Cardiac fibroblasts: from development to heart failure.* J Mol Med (Berl), 2015. **93**(8): p. 823-30.
32. Camelliti, P., T.K. Borg, and P. Kohl, *Structural and functional characterisation of cardiac fibroblasts.* Cardiovasc Res, 2005. **65**(1): p. 40-51.
33. Tallquist, M.D. and J.D. Molkentin, *Redefining the identity of cardiac fibroblasts.* Nat Rev Cardiol, 2017. **14**(8): p. 484-491.
34. Smith, C.L., et al., *Epicardial-derived cell epithelial-to-mesenchymal transition and fate specification require PDGF receptor signaling.* Circ Res, 2011. **108**(12): p. e15-26.
35. Acharya, A., et al., *The bHLH transcription factor Tcf21 is required for lineage-specific EMT of cardiac fibroblast progenitors.* Development, 2012. **139**(12): p. 2139-49.
36. Moore-Morris, T., et al., *Resident fibroblast lineages mediate pressure overload-induced cardiac fibrosis.* J Clin Invest, 2014. **124**(7): p. 2921-34.
37. Ali, S.R., et al., *Developmental heterogeneity of cardiac fibroblasts does not predict pathological proliferation and activation.* Circ Res, 2014. **115**(7): p. 625-35.

38. Moore-Morris, T., et al., *Origins of cardiac fibroblasts.* J Mol Cell Cardiol, 2016. **91**: p. 1-5.
39. Pinto, A.R., et al., *Revisiting Cardiac Cellular Composition.* Circ Res, 2016. **118**(3): p. 400-9.
40. Baum, J. and H.S. Duffy, *Fibroblasts and myofibroblasts: what are we talking about?* J Cardiovasc Pharmacol, 2011. **57**(4): p. 376-9.
41. van den Borne, S.W., et al., *Myocardial remodeling after infarction: the role of myofibroblasts.* Nat Rev Cardiol, 2010. **7**(1): p. 30-7.
42. Stempien-Otero, A., D.H. Kim, and J. Davis, *Molecular networks underlying myofibroblast fate and fibrosis.* J Mol Cell Cardiol, 2016. **97**: p. 153-61.
43. Frangogiannis, N.G., L.H. Michael, and M.L. Entman, *Myofibroblasts in reperfused myocardial infarcts express the embryonic form of smooth muscle myosin heavy chain (SMemb).* Cardiovasc Res, 2000. **48**(1): p. 89-100.
44. Pichler, M., et al., *Cardiac fibrosis in human transplanted hearts is mainly driven by cells of intracardiac origin.* J Am Coll Cardiol, 2012. **59**(11): p. 1008-16.
45. Kanisicak, O., et al., *Genetic lineage tracing defines myofibroblast origin and function in the injured heart.* Nat Commun, 2016. **7**: p. 12260.
46. Ruiz-Villalba, A., et al., *Interacting resident epicardium-derived fibroblasts and recruited bone marrow cells form myocardial infarction scar.* J Am Coll Cardiol, 2015. **65**(19): p. 2057-66.
47. Zeisberg, E.M., et al., *Endothelial-to-mesenchymal transition contributes to cardiac fibrosis.* Nat Med, 2007. **13**(8): p. 952-61.
48. Fu, X., et al., *Specialized fibroblast differentiated states underlie scar formation in the infarcted mouse heart.* J Clin Invest, 2018. **128**(5): p. 2127-2143.
49. Farbehi, N., et al., *Single-cell expression profiling reveals dynamic flux of cardiac stromal, vascular and immune cells in health and injury.* Elife, 2019. **8**.

50. Forte, E., et al., *Dynamic Interstitial Cell Response during Myocardial Infarction Predicts Resilience to Rupture in Genetically Diverse Mice.* Cell Rep, 2020. **30**(9): p. 3149-3163.e6.
51. Gladka, M.M., et al., *Single-Cell Sequencing of the Healthy and Diseased Heart Reveals Cytoskeleton-Associated Protein 4 as a New Modulator of Fibroblasts Activation.* Circulation, 2018. **138**(2): p. 166-180.
52. Hayakawa, K., et al., *Inhibition of granulation tissue cell apoptosis during the subacute stage of myocardial infarction improves cardiac remodeling and dysfunction at the chronic stage.* Circulation, 2003. **108**(1): p. 104-9.
53. Campbell, S.E. and L.C. Katwa, *Angiotensin II stimulated expression of transforming growth factor-beta1 in cardiac fibroblasts and myofibroblasts.* J Mol Cell Cardiol, 1997. **29**(7): p. 1947-58.
54. van Beusekom, C.D. and T.M. Zimmering, *Profibrotic effects of angiotensin II and transforming growth factor beta on feline kidney epithelial cells.* J Feline Med Surg, 2019. **21**(8): p. 780-787.
55. Yu, J., et al., *Transgenic expression of an altered angiotensin type I AT1 receptor resulting in marked modulation of vascular type I collagen.* J Cell Physiol, 2012. **227**(5): p. 2013-21.
56. Lavoie, J.L. and C.D. Sigmund, *Minireview: overview of the renin-angiotensin system--an endocrine and paracrine system.* Endocrinology, 2003. **144**(6): p. 2179-83.
57. Kaschina, E., P. Namsolleck, and T. Unger, *AT2 receptors in cardiovascular and renal diseases.* Pharmacol Res, 2017. **125**(Pt A): p. 39-47.
58. Ohtsu, H., et al., *Central role of Gq in the hypertrophic signal transduction of angiotensin II in vascular smooth muscle cells.* Endocrinology, 2008. **149**(7): p. 3569-75.
59. Mehta, P.K. and K.K. Griendling, *Angiotensin II cell signaling: physiological and pathological effects in the cardiovascular system.* Am J Physiol Cell Physiol, 2007. **292**(1): p. C82-97.
60. Ongherth, A., et al., *p63RhoGEF regulates auto- and paracrine signaling in cardiac fibroblasts.* J Mol Cell Cardiol, 2015. **88**: p. 39-54.

61. Zhang, B., et al., *Store-Operated Ca(2+) Entry (SOCE) contributes to angiotensin II-induced cardiac fibrosis in cardiac fibroblasts.* J Pharmacol Sci, 2016. **132**(3): p. 171-180.
62. Hou, M., et al., *Angiotensin II type 1 receptors stimulate protein synthesis in human cardiac fibroblasts via a Ca2+-sensitive PKC-dependent tyrosine kinase pathway.* Acta Physiol Scand, 2000. **168**(2): p. 301-9.
63. Brilla, C.G., C. Scheer, and H. Rupp, *Angiotensin II and intracellular calcium of adult cardiac fibroblasts.* J Mol Cell Cardiol, 1998. **30**(6): p. 1237-46.
64. Letavernier, E., et al., *Targeting the calpain/calpastatin system as a new strategy to prevent cardiovascular remodeling in angiotensin II-induced hypertension.* Circ Res, 2008. **102**(6): p. 720-8.
65. Camacho Londoño, J.E., et al., *Angiotensin-II-Evoked Ca(2+) Entry in Murine Cardiac Fibroblasts Does Not Depend on TRPC Channels.* Cells, 2020. **9**(2).
66. Rose, R.A., et al., *C-type natriuretic peptide activates a non-selective cation current in acutely isolated rat cardiac fibroblasts via natriuretic peptide C receptor-mediated signalling.* J Physiol, 2007. **580**(Pt 1): p. 255-74.
67. Schelling, J.R., et al., *Angiotensin II activates the beta 1 isoform of phospholipase C in vascular smooth muscle cells.* Am J Physiol, 1997. **272**(5 Pt 1): p. C1558-66.
68. Crabos, M., et al., *Characterization of angiotensin II receptors in cultured adult rat cardiac fibroblasts. Coupling to signaling systems and gene expression.* J Clin Invest, 1994. **93**(6): p. 2372-8.
69. Olson, E.R., et al., *Angiotensin II-induced extracellular signal-regulated kinase 1/2 activation is mediated by protein kinase Cdelta and intracellular calcium in adult rat cardiac fibroblasts.* Hypertension, 2008. **51**(3): p. 704-11.
70. Harada, M., et al., *Transient receptor potential canonical-3 channel-dependent fibroblast regulation in atrial fibrillation.* Circulation, 2012. **126**(17): p. 2051-64.
71. Murasawa, S., et al., *Angiotensin II type 1 receptor-induced extracellular signal-regulated protein kinase activation is mediated by Ca2+/calmodulin-*

dependent transactivation of epidermal growth factor receptor. Circ Res, 1998. **82**(12): p. 1338-48.

72. Kim, S., et al., *Angiotensin II induces cardiac phenotypic modulation and remodeling in vivo in rats.* Hypertension, 1995. **25**(6): p. 1252-9.
73. Tan, L.B., et al., *Cardiac myocyte necrosis induced by angiotensin II.* Circ Res, 1991. **69**(5): p. 1185-95.
74. Kaur, H., et al., *Targeted Ablation of Periostin-Expressing Activated Fibroblasts Prevents Adverse Cardiac Remodeling in Mice.* Circ Res, 2016. **118**(12): p. 1906-17.
75. Acharya, A., et al., *Efficient inducible Cre-mediated recombination in Tcf21 cell lineages in the heart and kidney.* Genesis, 2011. **49**(11): p. 870-7.
76. Doetschman, T., et al., *Transforming growth factor beta signaling in adult cardiovascular diseases and repair.* Cell Tissue Res, 2012. **347**(1): p. 203-23.
77. Edgley, A.J., H. Krum, and D.J. Kelly, *Targeting fibrosis for the treatment of heart failure: a role for transforming growth factor-β.* Cardiovasc Ther, 2012. **30**(1): p. e30-40.
78. Thompson, N.L., et al., *Expression of transforming growth factor-beta 1 in specific cells and tissues of adult and neonatal mice.* J Cell Biol, 1989. **108**(2): p. 661-9.
79. Wünsch, M., et al., *In situ localization of transforming growth factor beta 1 in porcine heart: enhanced expression after chronic coronary artery constriction.* J Mol Cell Cardiol, 1991. **23**(9): p. 1051-62.
80. Robertson, I.B. and D.B. Rifkin, *Regulation of the Bioavailability of TGF-β and TGF-β-Related Proteins.* Cold Spring Harb Perspect Biol, 2016. **8**(6).
81. Meyer, A., et al., *Platelet TGF-β1 contributions to plasma TGF-β1, cardiac fibrosis, and systolic dysfunction in a mouse model of pressure overload.* Blood, 2012. **119**(4): p. 1064-74.
82. van Amerongen, M.J., et al., *Macrophage depletion impairs wound healing and increases left ventricular remodeling after myocardial injury in mice.* Am J Pathol, 2007. **170**(3): p. 818-29.

83. Kaur, K., et al., *TGF-β1, released by myofibroblasts, differentially regulates transcription and function of sodium and potassium channels in adult rat ventricular myocytes.* PLoS One, 2013. **8**(2): p. e55391.
84. Desmoulière, A., et al., *Transforming growth factor-beta 1 induces alpha-smooth muscle actin expression in granulation tissue myofibroblasts and in quiescent and growing cultured fibroblasts.* J Cell Biol, 1993. **122**(1): p. 103-11.
85. Heldin, C.H. and A. Moustakas, *Signaling Receptors for TGF-β Family Members.* Cold Spring Harb Perspect Biol, 2016. **8**(8).
86. Heldin, C.H., K. Miyazono, and P. ten Dijke, *TGF-beta signalling from cell membrane to nucleus through SMAD proteins.* Nature, 1997. **390**(6659): p. 465-71.
87. Wrana, J.L., et al., *Mechanism of activation of the TGF-beta receptor.* Nature, 1994. **370**(6488): p. 341-7.
88. Khalil, H., et al., *Fibroblast-specific TGF-β-Smad2/3 signaling underlies cardiac fibrosis.* J Clin Invest, 2017. **127**(10): p. 3770-3783.
89. Lewis, G.A., et al., *Pirfenidone in Heart Failure with Preserved Ejection Fraction-Rationale and Design of the PIROUETTE Trial.* Cardiovasc Drugs Ther, 2019. **33**(4): p. 461-470.
90. Ruwanpura, S.M., B.J. Thomas, and P.G. Bardin, *Pirfenidone: Molecular Mechanisms and Potential Clinical Applications in Lung Disease.* Am J Respir Cell Mol Biol, 2020. **62**(4): p. 413-422.
91. Fisher, S.A. and M. Absher, *Norepinephrine and ANG II stimulate secretion of TGF-beta by neonatal rat cardiac fibroblasts in vitro.* Am J Physiol, 1995. **268**(4 Pt 1): p. C910-7.
92. Chen, K., et al., *Transforming growth factor beta receptor endoglin is expressed in cardiac fibroblasts and modulates profibrogenic actions of angiotensin II.* Circ Res, 2004. **95**(12): p. 1167-73.
93. Zhang, Y., et al., *miR-29b as a therapeutic agent for angiotensin II-induced cardiac fibrosis by targeting TGF-β/Smad3 signaling.* Mol Ther, 2014. **22**(5): p. 974-85.

94. Zhou, H.T., X.F. Yu, and G.M. Zhou, *Diosgenin inhibits angiotensin II-induced extracellular matrix remodeling in cardiac fibroblasts through regulating the TGF‑β1/Smad3 signaling pathway.* Mol Med Rep, 2017. **15**(5): p. 2823-2828.

95. Wong, C.K.S., et al., *Connective tissue growth factor expression after angiotensin II exposure is dependent on transforming growth factor-β signaling via the canonical Smad-dependent pathway in hypertensive induced myocardial fibrosis.* J Renin Angiotensin Aldosterone Syst, 2018. **19**(1): p. 1470320318759358.

96. Rosenkranz, S., *TGF-beta1 and angiotensin networking in cardiac remodeling.* Cardiovasc Res, 2004. **63**(3): p. 423-32.

97. Gallagher, A.M., et al., *Species variability in angiotensin receptor expression by cultured cardiac fibroblasts and the infarcted heart.* Am J Physiol, 1998. **274**(3): p. H801-9.

98. Sandmann, S., et al., *Calcium channel blockade limits cardiac remodeling and improves cardiac function in myocardial infarction-induced heart failure in rats.* J Cardiovasc Pharmacol, 2001. **37**(1): p. 64-77.

99. Yue, H., et al., *Different effects of calcium channel blockers on matrix metalloproteinase-2 expression in cultured rat cardiac fibroblasts.* J Cardiovasc Pharmacol, 2004. **44**(2): p. 223-30.

100. Jia, Y., et al., *Nifedipine inhibits angiotensin II-induced cardiac fibrosis via downregulating Nox4-derived ROS generation and suppressing ERK1/2, JNK signaling pathways.* Pharmazie, 2013. **68**(6): p. 435-41.

101. Huang, C.L., *The transient receptor potential superfamily of ion channels.* J Am Soc Nephrol, 2004. **15**(7): p. 1690-9.

102. Ong, H.L., et al., *Physiological functions and regulation of TRPC channels.* Handb Exp Pharmacol, 2014. **223**: p. 1005-34.

103. Plant, T.D., *TRPs in mechanosensing and volume regulation.* Handb Exp Pharmacol, 2014. **223**: p. 743-66.

104. Chen, J.B., et al., *Multiple Ca2+ signaling pathways regulate intracellular Ca2+ activity in human cardiac fibroblasts.* J Cell Physiol, 2010. **223**(1): p. 68-75.

105. Ikeda, K., et al., *Roles of transient receptor potential canonical (TRPC) channels and reverse-mode Na+/Ca2+ exchanger on cell proliferation in human cardiac fibroblasts: effects of transforming growth factor β1.* Cell Calcium, 2013. **54**(3): p. 213-25.
106. Kiyonaka, S., et al., *Selective and direct inhibition of TRPC3 channels underlies biological activities of a pyrazole compound.* Proc Natl Acad Sci U S A, 2009. **106**(13): p. 5400-5.
107. Numaga-Tomita, T., et al., *TRPC3-GEF-H1 axis mediates pressure overload-induced cardiac fibrosis.* Sci Rep, 2016. **6**: p. 39383.
108. Nishida, M., et al., *Galpha12/13-mediated up-regulation of TRPC6 negatively regulates endothelin-1-induced cardiac myofibroblast formation and collagen synthesis through nuclear factor of activated T cells activation.* J Biol Chem, 2007. **282**(32): p. 23117-28.
109. Davis, J., et al., *A TRPC6-dependent pathway for myofibroblast transdifferentiation and wound healing in vivo.* Dev Cell, 2012. **23**(4): p. 705-15.
110. Kapur, N.K., et al., *Reducing endoglin activity limits calcineurin and TRPC-6 expression and improves survival in a mouse model of right ventricular pressure overload.* J Am Heart Assoc, 2014. **3**(4).
111. Lewis, R.S., *Store-Operated Calcium Channels: From Function to Structure and Back Again.* Cold Spring Harb Perspect Biol, 2020. **12**(5).
112. Čendula, R., et al., *Changes in STIM isoforms expression and gender-specific alterations in Orai expression in human heart failure.* Physiol Res, 2019. **68**(Suppl 2): p. S165-s172.
113. Ross, G.R., et al., *Enhanced store-operated Ca(2+) influx and ORAI1 expression in ventricular fibroblasts from human failing heart.* Biol Open, 2017. **6**(3): p. 326-332.
114. Bartoli, F., et al., *Orai1 Channel Inhibition Preserves Left Ventricular Systolic Function and Normal Ca(2+) Handling After Pressure Overload.* Circulation, 2020. **141**(3): p. 199-216.
115. Horton, J.S., et al., *The calcium release-activated calcium channel Orai1 represents a crucial component in hypertrophic compensation and the*

development of dilated cardiomyopathy. Channels (Austin), 2014. **8**(1): p. 35-48.

116. Mohis, M., et al., *Aging-related increase in store-operated Ca(2+) influx in human ventricular fibroblasts.* Am J Physiol Heart Circ Physiol, 2018. **315**(1): p. H83-h91.
117. Luik, R.M., et al., *The elementary unit of store-operated Ca2+ entry: local activation of CRAC channels by STIM1 at ER-plasma membrane junctions.* J Cell Biol, 2006. **174**(6): p. 815-25.
118. Reichling, D.B. and A.B. MacDermott, *Lanthanum actions on excitatory amino acid-gated currents and voltage-gated calcium currents in rat dorsal horn neurons.* J Physiol, 1991. **441**: p. 199-218.
119. Kamkin, A., I. Kiseleva, and G. Isenberg, *Activation and inactivation of a non-selective cation conductance by local mechanical deformation of acutely isolated cardiac fibroblasts.* Cardiovasc Res, 2003. **57**(3): p. 793-803.
120. Franzius, D., M. Hoth, and R. Penner, *Non-specific effects of calcium entry antagonists in mast cells.* Pflugers Arch, 1994. **428**(5-6): p. 433-8.
121. Djuric, S.W., et al., *3,5-Bis(trifluoromethyl)pyrazoles: a novel class of NFAT transcription factor regulator.* J Med Chem, 2000. **43**(16): p. 2975-81.
122. Trevillyan, J.M., et al., *Potent inhibition of NFAT activation and T cell cytokine production by novel low molecular weight pyrazole compounds.* J Biol Chem, 2001. **276**(51): p. 48118-26.
123. Ishikawa, J., et al., *A pyrazole derivative, YM-58483, potently inhibits store-operated sustained Ca2+ influx and IL-2 production in T lymphocytes.* J Immunol, 2003. **170**(9): p. 4441-9.
124. Zitt, C., et al., *Potent inhibition of Ca2+ release-activated Ca2+ channels and T-lymphocyte activation by the pyrazole derivative BTP2.* J Biol Chem, 2004. **279**(13): p. 12427-37.
125. Takezawa, R., et al., *A pyrazole derivative potently inhibits lymphocyte Ca2+ influx and cytokine production by facilitating transient receptor potential melastatin 4 channel activity.* Mol Pharmacol, 2006. **69**(4): p. 1413-20.

126. He, L.P., et al., *A functional link between store-operated and TRPC channels revealed by the 3,5-bis(trifluoromethyl)pyrazole derivative, BTP2.* J Biol Chem, 2005. **280**(12): p. 10997-1006.
127. Law, M., et al., *Structural requirements for the inhibition of calcium mobilization and mast cell activation by the pyrazole derivative BTP2.* Int J Biochem Cell Biol, 2011. **43**(8): p. 1228-39.
128. Zhang, W., Z. Qi, and Y. Wang, *BTP2, a Store-Operated Calcium Channel Inhibitor, Attenuates Lung Ischemia-Reperfusion Injury in Rats.* Inflammation, 2017. **40**(3): p. 778-787.
129. Sogkas, G., et al., *The Pyrazole Derivative BTP2 Attenuates IgG Immune Complex-induced Inflammation.* Inflammation, 2018. **41**(1): p. 42-49.
130. Derler, I., et al., *The extended transmembrane Orai1 N-terminal (ETON) region combines binding interface and gate for Orai1 activation by STIM1.* J Biol Chem, 2013. **288**(40): p. 29025-34.
131. Nash, M.S., et al., *Intracellular signalling. Receptor-specific messenger oscillations.* Nature, 2001. **413**(6854): p. 381-2.
132. Harootunian, A.T., et al., *Generation of calcium oscillations in fibroblasts by positive feedback between calcium and IP3.* Science, 1991. **251**(4989): p. 75-8.
133. Wöll, E., et al., *Mechanism of intracellular calcium oscillations in fibroblasts expressing the ras oncogene.* Pflugers Arch, 1992. **420**(2): p. 208-12.
134. Kawanishi, T., et al., *Ca2+ oscillations induced by hormonal stimulation of individual fura-2-loaded hepatocytes.* J Biol Chem, 1989. **264**(22): p. 12859-66.
135. Lewis, R.S. and M.D. Cahalan, *Mitogen-induced oscillations of cytosolic Ca2+ and transmembrane Ca2+ current in human leukemic T cells.* Cell Regul, 1989. **1**(1): p. 99-112.
136. Bird, G.S. and J.W. Putney, Jr., *Capacitative calcium entry supports calcium oscillations in human embryonic kidney cells.* J Physiol, 2005. **562**(Pt 3): p. 697-706.

137. Wedel, B., et al., *Role of the store-operated calcium entry proteins Stim1 and Orai1 in muscarinic cholinergic receptor-stimulated calcium oscillations in human embryonic kidney cells.* J Physiol, 2007. **579**(Pt 3): p. 679-89.
138. Brandman, O., et al., *STIM2 is a feedback regulator that stabilizes basal cytosolic and endoplasmic reticulum Ca2+ levels.* Cell, 2007. **131**(7): p. 1327-39.
139. Peltonen, H.M., et al., *Involvement of TRPC3 channels in calcium oscillations mediated by OX(1) orexin receptors.* Biochem Biophys Res Commun, 2009. **385**(3): p. 408-12.
140. Castella, L.F., et al., *A new lock-step mechanism of matrix remodelling based on subcellular contractile events.* J Cell Sci, 2010. **123**(Pt 10): p. 1751-60.
141. Parkash, J. and K. Asotra, *Calcium oscillations and waves in cells.* Adv Exp Med Biol, 2012. **740**: p. 521-9.
142. Godbout, C., et al., *The mechanical environment modulates intracellular calcium oscillation activities of myofibroblasts.* PLoS One, 2013. **8**(5): p. e64560.
143. Mauban, J.R., et al., *A method for noninvasive longitudinal measurements of [Ca2+] in arterioles of hypertensive optical biosensor mice.* Am J Physiol Heart Circ Physiol, 2014. **307**(2): p. H173-81.
144. Boerman, E.M., J.E. Everhart, and S.S. Segal, *Advanced age decreases local calcium signaling in endothelium of mouse mesenteric arteries in vivo.* Am J Physiol Heart Circ Physiol, 2016. **310**(9): p. H1091-6.
145. Senft, D. and Z.A. Ronai, *UPR, autophagy, and mitochondria crosstalk underlies the ER stress response.* Trends Biochem Sci, 2015. **40**(3): p. 141-8.
146. Harding, H.P., et al., *Perk is essential for translational regulation and cell survival during the unfolded protein response.* Mol Cell, 2000. **5**(5): p. 897-904.
147. Choy, K.W., D. Murugan, and M.R. Mustafa, *Natural products targeting ER stress pathway for the treatment of cardiovascular diseases.* Pharmacol Res, 2018. **132**: p. 119-129.

148. Walter, P. and D. Ron, *The unfolded protein response: from stress pathway to homeostatic regulation.* Science, 2011. **334**(6059): p. 1081-6.
149. Suzuki, C.K., et al., *Regulating the retention of T-cell receptor alpha chain variants within the endoplasmic reticulum: Ca(2+)-dependent association with BiP.* J Cell Biol, 1991. **114**(2): p. 189-205.
150. Narindrasorasak, S., P. Yao, and B. Sarkar, *Protein disulfide isomerase, a multifunctional protein chaperone, shows copper-binding activity.* Biochem Biophys Res Commun, 2003. **311**(2): p. 405-14.
151. Michalak, M., et al., *Calreticulin, a multi-process calcium-buffering chaperone of the endoplasmic reticulum.* Biochem J, 2009. **417**(3): p. 651-66.
152. Corbett, E.F., et al., *Ca2+ regulation of interactions between endoplasmic reticulum chaperones.* J Biol Chem, 1999. **274**(10): p. 6203-11.
153. Gao, L., et al., *ER stress activation impairs the expression of circadian clock and clock-controlled genes in NIH3T3 cells via an ATF4-dependent mechanism.* Cell Signal, 2019. **57**: p. 89-101.
154. Kim, D.S., et al., *p38 Mitogen-activated protein kinase is involved in endoplasmic reticulum stress-induced cell death and autophagy in human gingival fibroblasts.* Biol Pharm Bull, 2010. **33**(4): p. 545-9.
155. Shin, Y.J., et al., *Autophagy induction and CHOP under-expression promotes survival of fibroblasts from rheumatoid arthritis patients under endoplasmic reticulum stress.* Arthritis Res Ther, 2010. **12**(1): p. R19.
156. Sadighi Akha, A.A., et al., *Heightened induction of proapoptotic signals in response to endoplasmic reticulum stress in primary fibroblasts from a mouse model of longevity.* J Biol Chem, 2011. **286**(35): p. 30344-51.
157. Eckstein, M., et al., *Store-operated Ca(2+) entry controls ameloblast cell function and enamel development.* JCI Insight, 2017. **2**(6): p. e91166.
158. Li, P., et al., *Blocking of stromal interaction molecule 1 expression influence cell proliferation and promote cell apoptosis in vitro and inhibit tumor growth in vivo in head and neck squamous cell carcinoma.* PLoS One, 2017. **12**(5): p. e0177484.

159. Waldron, R.T., et al., *The Orai Ca(2+) channel inhibitor CM4620 targets both parenchymal and immune cells to reduce inflammation in experimental acute pancreatitis.* J Physiol, 2019. **597**(12): p. 3085-3105.
160. Secondo, A., et al., *ORAI1/STIM1 Interaction Intervenes in Stroke and in Neuroprotection Induced by Ischemic Preconditioning Through Store-Operated Calcium Entry.* Stroke, 2019. **50**(5): p. 1240-1249.
161. Kono, T., et al., *Impaired Store-Operated Calcium Entry and STIM1 Loss Lead to Reduced Insulin Secretion and Increased Endoplasmic Reticulum Stress in the Diabetic β-Cell.* Diabetes, 2018. **67**(11): p. 2293-2304.
162. Nascimento Da Conceicao, V., et al., *Loss of Ca(2+) entry via Orai-TRPC1 induces ER stress, initiating immune activation in macrophages.* J Cell Sci, 2019. **133**(5).
163. Zhang, I.X., et al., *ER stress increases store-operated Ca(2+) entry (SOCE) and augments basal insulin secretion in pancreatic beta cells.* J Biol Chem, 2020. **295**(17): p. 5685-5700.
164. Zhou, J., J. Song, and S. Wu, *Autophagic degradation of stromal interaction molecule 2 mediates disruption of neuronal dendrites by endoplasmic reticulum stress.* J Neurochem, 2019. **151**(3): p. 351-369.
165. Maiers, J.L. and H. Malhi, *Endoplasmic Reticulum Stress in Metabolic Liver Diseases and Hepatic Fibrosis.* Semin Liver Dis, 2019. **39**(2): p. 235-248.
166. Cybulsky, A.V., *Endoplasmic reticulum stress, the unfolded protein response and autophagy in kidney diseases.* Nat Rev Nephrol, 2017. **13**(11): p. 681-696.
167. Burman, A., H. Tanjore, and T.S. Blackwell, *Endoplasmic reticulum stress in pulmonary fibrosis.* Matrix Biol, 2018. **68-69**: p. 355-365.
168. Dickens, J.A., et al., *Pulmonary endoplasmic reticulum stress-scars, smoke, and suffocation.* Febs j, 2019. **286**(2): p. 322-341.
169. Yang, Q., et al., *Sequential changes of endoplasmic reticulum stress and apoptosis in myocardial fibrosis of diabetes mellitus-induced rats.* Mol Med Rep, 2016. **13**(6): p. 5037-44.
170. Lakshmanan, A.P., et al., *The hyperglycemia stimulated myocardial endoplasmic reticulum (ER) stress contributes to diabetic cardiomyopathy in*

the transgenic non-obese type 2 diabetic rats: a differential role of unfolded protein response (UPR) signaling proteins. Int J Biochem Cell Biol, 2013. **45**(2): p. 438-47.

171. Martindale, J.J., et al., *Endoplasmic reticulum stress gene induction and protection from ischemia/reperfusion injury in the hearts of transgenic mice with a tamoxifen-regulated form of ATF6.* Circ Res, 2006. **98**(9): p. 1186-93.
172. Okada, K., et al., *Prolonged endoplasmic reticulum stress in hypertrophic and failing heart after aortic constriction: possible contribution of endoplasmic reticulum stress to cardiac myocyte apoptosis.* Circulation, 2004. **110**(6): p. 705-12.
173. Dally, S., et al., *Compartmentalized expression of three novel sarco/endoplasmic reticulum Ca2+ATPase 3 isoforms including the switch to ER stress, SERCA3f, in non-failing and failing human heart.* Cell Calcium, 2009. **45**(2): p. 144-54.
174. Ayala, P., et al., *Attenuation of endoplasmic reticulum stress using the chemical chaperone 4-phenylbutyric acid prevents cardiac fibrosis induced by isoproterenol.* Exp Mol Pathol, 2012. **92**(1): p. 97-104.
175. Glembotski, C.C., et al., *ATF6 as a Nodal Regulator of Proteostasis in the Heart.* Front Physiol, 2020. **11**: p. 267.
176. Stauffer, W.T., et al., *The ER Unfolded Protein Response Effector, ATF6, Reduces Cardiac Fibrosis and Decreases Activation of Cardiac Fibroblasts.* Int J Mol Sci, 2020. **21**(4).
177. Xiao, Y., et al., *Hippo pathway deletion in adult resting cardiac fibroblasts initiates a cell state transition with spontaneous and self-sustaining fibrosis.* Genes Dev, 2019. **33**(21-22): p. 1491-1505.
178. Herum, K.M., et al., *The Soft- and Hard-Heartedness of Cardiac Fibroblasts: Mechanotransduction Signaling Pathways in Fibrosis of the Heart.* J Clin Med, 2017. **6**(5).
179. Chen, X. and S.L. Thibeault, *Response of fibroblasts to transforming growth factor-β1 on two-dimensional and in three-dimensional hyaluronan hydrogels.* Tissue Eng Part A, 2012. **18**(23-24): p. 2528-38.

180. Wang, H., et al., *Redirecting valvular myofibroblasts into dormant fibroblasts through light-mediated reduction in substrate modulus.* PLoS One, 2012. **7**(7): p. e39969.
181. Santos, G.L., et al., *Inhibition of Rho-associated kinases suppresses cardiac myofibroblast function in engineered connective and heart muscle tissues.* J Mol Cell Cardiol, 2019. **134**: p. 13-28.
182. Yu, J., et al., *Topological Arrangement of Cardiac Fibroblasts Regulates Cellular Plasticity.* Circ Res, 2018. **123**(1): p. 73-85.
183. Elson, E.L. and G.M. Genin, *Tissue constructs: platforms for basic research and drug discovery.* Interface Focus, 2016. **6**(1): p. 20150095.
184. Galie, P.A., M.V. Westfall, and J.P. Stegemann, *Reduced serum content and increased matrix stiffness promote the cardiac myofibroblast transition in 3D collagen matrices.* Cardiovasc Pathol, 2011. **20**(6): p. 325-33.
185. Ngu, J.M., et al., *Human cardiac fibroblast extracellular matrix remodeling: dual effects of tissue inhibitor of metalloproteinase-2.* Cardiovasc Pathol, 2014. **23**(6): p. 335-43.
186. Vettel, C., et al., *PDE2-mediated cAMP hydrolysis accelerates cardiac fibroblast to myofibroblast conversion and is antagonized by exogenous activation of cGMP signaling pathways.* Am J Physiol Heart Circ Physiol, 2014. **306**(8): p. H1246-52.
187. Jatho, A., et al., *RhoA Ambivalently Controls Prominent Myofibroblast Characteritics by Involving Distinct Signaling Routes.* PLoS One, 2015. **10**(10): p. e0137519.
188. Dworatzek, E., et al., *Sex-specific regulation of collagen I and III expression by 17β-Estradiol in cardiac fibroblasts: role of estrogen receptors.* Cardiovasc Res, 2019. **115**(2): p. 315-327.
189. Grimaldi, M., M. Maratos, and A. Verma, *Transient receptor potential channel activation causes a novel form of [Ca 2+]I oscillations and is not involved in capacitative Ca 2+ entry in glial cells.* J Neurosci, 2003. **23**(11): p. 4737-45.

190. Saliba, Y., et al., *Transient Receptor Potential Canonical 3 and Nuclear Factor of Activated T Cells C3 Signaling Pathway Critically Regulates Myocardial Fibrosis.* Antioxid Redox Signal, 2019. **30**(16): p. 1851-1879.
191. McGowan, T.A., et al., *TGF-beta-induced Ca(2+) influx involves the type III IP(3) receptor and regulates actin cytoskeleton.* Am J Physiol Renal Physiol, 2002. **282**(5): p. F910-20.
192. Dong, H., et al., *Molecular mechanisms underlying Ca2+-mediated motility of human pancreatic duct cells.* Am J Physiol Cell Physiol, 2010. **299**(6): p. C1493-503.
193. Gooch, J.L., et al., *Involvement of calcineurin in transforming growth factor-beta-mediated regulation of extracellular matrix accumulation.* J Biol Chem, 2004. **279**(15): p. 15561-70.
194. Mukherjee, S., et al., *Transforming growth factor-β evokes Ca2+ waves and enhances gene expression in human pulmonary fibroblasts.* Am J Respir Cell Mol Biol, 2012. **46**(6): p. 757-64.
195. He, R., et al., *Upregulation of Transient Receptor Potential Canonical Type 3 Channel via AT1R/TGF-β1/Smad2/3 Induces Atrial Fibrosis in Aging and Spontaneously Hypertensive Rats.* Oxid Med Cell Longev, 2019. **2019**: p. 4025496.
196. Schleifer, H., et al., *Novel pyrazole compounds for pharmacological discrimination between receptor-operated and store-operated Ca(2+) entry pathways.* Br J Pharmacol, 2012. **167**(8): p. 1712-22.
197. Wu, Y.L., et al., *Inhibition of TRPC6 channels ameliorates renal fibrosis and contributes to renal protection by soluble klotho.* Kidney Int, 2017. **91**(4): p. 830-841.
198. Ivey, M.J., et al., *Resident fibroblast expansion during cardiac growth and remodeling.* J Mol Cell Cardiol, 2018. **114**: p. 161-174.
199. McEwan, P.E., et al., *Differential effects of angiotensin II on cardiac cell proliferation and intramyocardial perivascular fibrosis in vivo.* Circulation, 1998. **98**(24): p. 2765-73.

200. Stockand, J.D. and J.G. Meszaros, *Aldosterone stimulates proliferation of cardiac fibroblasts by activating Ki-RasA and MAPK1/2 signaling.* Am J Physiol Heart Circ Physiol, 2003. **284**(1): p. H176-84.
201. Burke, R.M., et al., *Sacubitril/Valsartan Decreases Cardiac Fibrosis in Left Ventricle Pressure Overload by Restoring PKG Signaling in Cardiac Fibroblasts.* Circ Heart Fail, 2019. **12**(4): p. e005565.
202. Park, S., et al., *Genetic Regulation of Fibroblast Activation and Proliferation in Cardiac Fibrosis.* Circulation, 2018. **138**(12): p. 1224-1235.
203. Tao, H., et al., *MicroRNA-29a suppresses cardiac fibroblasts proliferation via targeting VEGF-A/MAPK signal pathway.* Int J Biol Macromol, 2016. **88**: p. 414-23.
204. Soeki, T., et al., *C-type natriuretic peptide, a novel antifibrotic and antihypertrophic agent, prevents cardiac remodeling after myocardial infarction.* J Am Coll Cardiol, 2005. **45**(4): p. 608-16.
205. Saliba, Y., et al., *Evidence of a Role for Fibroblast Transient Receptor Potential Canonical 3 Ca2+ Channel in Renal Fibrosis.* J Am Soc Nephrol, 2015. **26**(8): p. 1855-76.
206. Azimi, I., et al., *Pharmacological inhibition of store-operated calcium entry in MDA-MB-468 basal A breast cancer cells: consequences on calcium signalling, cell migration and proliferation.* Cell Mol Life Sci, 2018. **75**(24): p. 4525-4537.
207. Lodola, F., et al., *VEGF-induced intracellular Ca(2+) oscillations are down-regulated and do not stimulate angiogenesis in breast cancer-derived endothelial colony forming cells.* Oncotarget, 2017. **8**(56): p. 95223-95246.
208. Lin, V.H., et al., *The rapid immunosuppression in phytohemagglutinin-activated human T cells is inhibited by the proliferative Ca(2+) influx induced by progesterone and analogs.* Steroids, 2016. **111**: p. 71-78.
209. Ichikawa, J. and R. Inoue, *TRPC6 regulates cell cycle progression by modulating membrane potential in bone marrow stromal cells.* Br J Pharmacol, 2014. **171**(23): p. 5280-94.

210. Zhan, Z.Y., et al., *Over-expression of Orai1 mediates cell proliferation and associates with poor prognosis in human non-small cell lung carcinoma.* Int J Clin Exp Pathol, 2015. **8**(5): p. 5080-8.
211. Dubois, C., et al., *Remodeling of channel-forming ORAI proteins determines an oncogenic switch in prostate cancer.* Cancer Cell, 2014. **26**(1): p. 19-32.
212. Chen, Y.W., et al., *The STIM1-Orai1 pathway of store-operated Ca2+ entry controls the checkpoint in cell cycle G1/S transition.* Sci Rep, 2016. **6**: p. 22142.
213. Meng, K., et al., *Calcium sensing receptor modulates extracellular calcium entry and proliferation via TRPC3/6 channels in cultured human mesangial cells.* PLoS One, 2014. **9**(6): p. e98777.
214. Woo, J.S., et al., *TRPC3 cation channel plays an important role in proliferation and differentiation of skeletal muscle myoblasts.* Exp Mol Med, 2010. **42**(9): p. 614-27.
215. Aránguiz-Urroz, P., et al., *Differential participation of angiotensin II type 1 and 2 receptors in the regulation of cardiac cell death triggered by angiotensin II.* Am J Hypertens, 2009. **22**(5): p. 569-76.
216. Sicari, D., et al., *A guide to assessing endoplasmic reticulum homeostasis and stress in mammalian systems.* Febs j, 2020. **287**(1): p. 27-42.
217. Vonk, L.A., et al., *Endoplasmic reticulum stress inhibits collagen synthesis independent of collagen-modifying enzymes in different chondrocyte populations and dermal fibroblasts.* Biochem Cell Biol, 2010. **88**(3): p. 539-52.
218. Humeres, C., et al., *4-Phenylbutyric acid prevent cytotoxicity induced by thapsigargin in rat cardiac fibroblast.* Toxicol In Vitro, 2014. **28**(8): p. 1443-8.
219. Driesen, R.B., et al., *Reversible and irreversible differentiation of cardiac fibroblasts.* Cardiovasc Res, 2014. **101**(3): p. 411-22.
220. Engler, A.J., et al., *Embryonic cardiomyocytes beat best on a matrix with heart-like elasticity: scar-like rigidity inhibits beating.* J Cell Sci, 2008. **121**(Pt 22): p. 3794-802.

221. Zhao, R., C.S. Chen, and D.H. Reich, *Force-driven evolution of mesoscale structure in engineered 3D microtissues and the modulation of tissue stiffening.* Biomaterials, 2014. **35**(19): p. 5056-64.
222. Mewhort, H.E., et al., *Monocytes increase human cardiac myofibroblast-mediated extracellular matrix remodeling through TGF-β1.* Am J Physiol Heart Circ Physiol, 2016. **310**(6): p. H716-24.
223. Sadeghi, A.H., et al., *Engineered 3D Cardiac Fibrotic Tissue to Study Fibrotic Remodeling.* Adv Healthc Mater, 2017. **6**(11).
224. Sigusch, H.H., S.E. Campbell, and K.T. Weber, *Angiotensin II-induced myocardial fibrosis in rats: role of nitric oxide, prostaglandins and bradykinin.* Cardiovasc Res, 1996. **31**(4): p. 546-54.
225. Fernandez, P. and A.R. Bausch, *The compaction of gels by cells: a case of collective mechanical activity.* Integr Biol (Camb), 2009. **1**(3): p. 252-9.
226. Basu, U., et al., *Rapid metabolism of exogenous angiotensin II by catecholaminergic neuronal cells in culture media.* Physiol Rep, 2015. **3**(2).
227. Guy, J.L., et al., *Functional angiotensin-converting enzyme 2 is expressed in human cardiac myofibroblasts.* Exp Physiol, 2008. **93**(5): p. 579-88.
228. Chappell, M.C., *Biochemical evaluation of the renin-angiotensin system: the good, bad, and absolute?* Am J Physiol Heart Circ Physiol, 2016. **310**(2): p. H137-52.
229. Lijnen, P.J., et al., *Reversal of angiotensin II-stimulated collagen gel contraction in cardiac fibroblasts by aminopeptidase inhibition.* J Cardiovasc Pharmacol, 2005. **45**(1): p. 68-73.
230. Swaney, J.S., et al., *Inhibition of cardiac myofibroblast formation and collagen synthesis by activation and overexpression of adenylyl cyclase.* Proc Natl Acad Sci U S A, 2005. **102**(2): p. 437-42.
231. Zhao, R., et al., *Decoupling cell and matrix mechanics in engineered microtissues using magnetically actuated microcantilevers.* Adv Mater, 2013. **25**(12): p. 1699-705.
232. Marquez, J.P., E.L. Elson, and G.M. Genin, *Whole cell mechanics of contractile fibroblasts: relations between effective cellular and extracellular*

matrix moduli. Philos Trans A Math Phys Eng Sci, 2010. **368**(1912): p. 635-54.

233. Huang, M., et al., *Lysyl oxidase enzymes mediate TGF-β1-induced fibrotic phenotypes in human skin-like tissues.* Lab Invest, 2019. **99**(4): p. 514-527.
234. Janmey, P.A. and R.T. Miller, *Mechanisms of mechanical signaling in development and disease.* J Cell Sci, 2011. **124**(Pt 1): p. 9-18.
235. Villemain, O., et al., *Myocardial Stiffness Evaluation Using Noninvasive Shear Wave Imaging in Healthy and Hypertrophic Cardiomyopathic Adults.* JACC Cardiovasc Imaging, 2019. **12**(7 Pt 1): p. 1135-1145.
236. Wakatsuki, T., et al., *Cell mechanics studied by a reconstituted model tissue.* Biophys J, 2000. **79**(5): p. 2353-68.
237. Schleifenbaum, S., et al., *Acellularization-Induced Changes in Tensile Properties Are Organ Specific - An In-Vitro Mechanical and Structural Analysis of Porcine Soft Tissues.* PLoS One, 2016. **11**(3): p. e0151223.
238. Pellegata, A.F., et al., *Detergent-enzymatic decellularization of swine blood vessels: insight on mechanical properties for vascular tissue engineering.* Biomed Res Int, 2013. **2013**: p. 918753.
239. Bott, K., et al., *The effect of matrix characteristics on fibroblast proliferation in 3D gels.* Biomaterials, 2010. **31**(32): p. 8454-64.
240. Rehman, M., et al., *High-throughput screening discovers antifibrotic properties of haloperidol by hindering myofibroblast activation.* JCI Insight, 2019. **4**(8).
241. Cho, N., S.E. Razipour, and M.L. McCain, *Featured Article: TGF-β1 dominates extracellular matrix rigidity for inducing differentiation of human cardiac fibroblasts to myofibroblasts.* Exp Biol Med (Maywood), 2018. **243**(7): p. 601-612.
242. Wang, W., et al., *P2Y6 regulates cytoskeleton reorganization and cell migration of C2C12 myoblasts via ROCK pathway.* J Cell Biochem, 2018. **119**(2): p. 1889-1898.
243. Paul, M., et al., *Protease-activated receptor 2 activates CRAC-mediated Ca2+ influx to cause prostate smooth muscle contraction.* FASEB Bioadv, 2019. **1**(4): p. 255-264.

244. Marquez, J.P., et al., *Cellular and matrix contributions to tissue construct stiffness increase with cellular concentration.* Ann Biomed Eng, 2006. **34**(9): p. 1475-82.

245. Camasão, D.B., et al., *Increasing Cell Seeding Density Improves Elastin Expression and Mechanical Properties in Collagen Gel-Based Scaffolds Cellularized with Smooth Muscle Cells.* Biotechnol J, 2019. **14**(3): p. e1700768.

246 Frangogiannis NG. Cardiac fibrosis: *Cell biological mechanisms, molecular pathways and therapeutic opportunities*. Mol Aspects Med. 2019 Feb;65:70-99. doi: 10.1016/j.mam.2018.07.001. Epub 2018 Aug 2. PMID: 30056242.